



National Library
of Canada

Acquisitions and
Bibliographic Services Branch

395 Wellington Street
Ottawa, Ontario
K1A 0N4

Bibliothèque nationale
du Canada

Direction des acquisitions et
des services bibliographiques

395, rue Wellington
Ottawa (Ontario)
K1A 0N4

Your file: Votre référence

Our file: Notre référence

NOTICE

The quality of this microform is heavily dependent upon the quality of the original thesis submitted for microfilming. Every effort has been made to ensure the highest quality of reproduction possible.

If pages are missing, contact the university which granted the degree.

Some pages may have indistinct print especially if the original pages were typed with a poor typewriter ribbon or if the university sent us an inferior photocopy.

Reproduction in full or in part of this microform is governed by the Canadian Copyright Act, R.S.C. 1970, c. C-30, and subsequent amendments.

AVIS

La qualité de cette microforme dépend grandement de la qualité de la thèse soumise au microfilmage. Nous avons tout fait pour assurer une qualité supérieure de reproduction.

S'il manque des pages, veuillez communiquer avec l'université qui a conféré le grade.

La qualité d'impression de certaines pages peut laisser à désirer, surtout si les pages originales ont été dactylographiées à l'aide d'un ruban usé ou si l'université nous a fait parvenir une photocopie de qualité inférieure.

La reproduction, même partielle, de cette microforme est soumise à la Loi canadienne sur le droit d'auteur, SRC 1970, c. C-30, et ses amendements subséquents.

UNIVERSITY OF ALBERTA

KeV X-Ray Generation from Picosecond KrF Laser Plasmas

By

James Norman Broughton



**A thesis submitted to the Faculty of Graduate Studies and Research in partial fulfillment
of the requirements for the degree of Doctor of Philosophy.**

Department of Electrical Engineering

Edmonton, Alberta

Fall 1992



National Library
of Canada

Acquisitions and
Bibliographic Services Branch

395 Wellington Street
Ottawa, Ontario
K1A 0N4

Bibliothèque nationale
du Canada

Direction des acquisitions et
des services bibliographiques

395, rue Wellington
Ottawa (Ontario)
K1A 0N4

our file *Voire référence*

Our file *Notre référence*

The author has granted an irrevocable non-exclusive licence allowing the National Library of Canada to reproduce, loan, distribute or sell copies of his/her thesis by any means and in any form or format, making this thesis available to interested persons.

L'auteur a accordé une licence irrévocable et non exclusive permettant à la Bibliothèque nationale du Canada de reproduire, prêter, distribuer ou vendre des copies de sa thèse de quelque manière et sous quelque forme que ce soit pour mettre des exemplaires de cette thèse à la disposition des personnes intéressées.

The author retains ownership of the copyright in his/her thesis. Neither the thesis nor substantial extracts from it may be printed or otherwise reproduced without his/her permission.

L'auteur conserve la propriété du droit d'auteur qui protège sa thèse. Ni la thèse ni des extraits substantiels de celle-ci ne doivent être imprimés ou autrement reproduits sans son autorisation.

ISBN 0-315-77366-9

Canada

UNIVERSITY OF ALBERTA
RELEASE FORM

NAME OF AUTHOR: James Norman Broughton

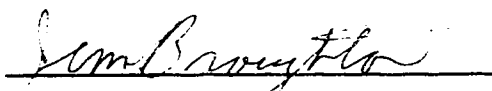
TITLE OF THESIS: KeV X-ray Generation from Picosecond KrF Laser Plasmas

DEGREE: Doctor of Philosophy

YEAR THIS DEGREE GRANTED: 1992

Permission is hereby granted to the University of Alberta Library to reproduce single copies of this thesis and to lend or sell such copies for private, scholarly or scientific research purposes only.

The author reserves all other publication and other rights in association with the copyright in the thesis, and except as hereinbefore provided neither the thesis nor any substantial portion thereof may be printed or otherwise reproduced in any material form whatever without the author's prior written permission.



3114 Leduc Crescent S.W.

Calgary, Alberta

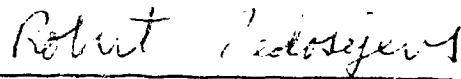
Canada, T3E 5W9

September 10, 1992

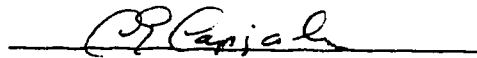
UNIVERSITY OF ALBERTA

FACULTY OF GRADUATE STUDIES AND RESEARCH

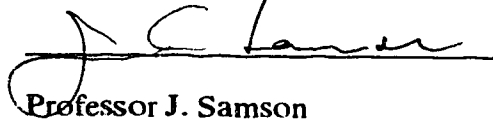
The undersigned certify that they have read, and recommend to the Faculty of Graduate Studies and Research for acceptance, a thesis entitled **KeV X-Ray Generation from Picosecond KrF Laser Plasmas** submitted by **James Norman Broughton** in partial fulfillment of the requirements for the degree of Doctor of Philosophy.



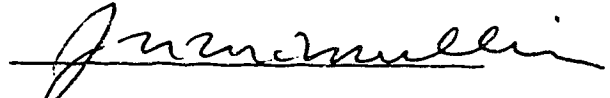
Professor R. Fedosejevs



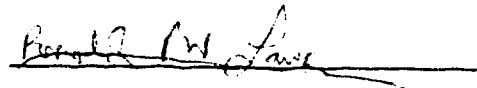
Professor C.E. Capjack



Professor J. Samson



Professor J. McMullin



Professor R.P.W. Lawson



Dr. G. Enright

Date: *Sept 29/42*

ABSTRACT

A krypton fluoride (KrF) laser system and target interaction facility has been developed in order to carry out investigations into keV x-ray conversion efficiency from short pulse (1 - 100 ps) KrF laser generated plasmas. The system which has been developed consists of a XeCl pump laser and two separate dye laser pulse generators which produce single pulses of approximately 1 ps and 100 ps duration at 497 nm wavelength. The dye laser pulses are frequency doubled to 248 nm and amplified to typical energies of 50 mJ in a discharge pumped KrF amplifier.

X-ray conversion efficiencies for 800 - 1400 eV x-rays in 2π Sr have been measured using these pulses for various metal target materials including Ti, Fe, Co, Ni, Cu, Zn and Sn. Crystal spectrographs were used to record the emission spectra and filtered semiconductor diode detectors to measure the absolute emission levels. Pulses of 120 ps duration focused to intensities of $1.5 \times 10^{14} \text{ Wcm}^{-2}$ produced conversion efficiencies of 1 - 3% for mid-atomic number materials such as Fe, Ni and Cu. A pulse length of 90 ps and improved focusing optics gave an intensity of $8 \times 10^{14} \text{ Wcm}^{-2}$ and increased yields to the 10 - 13% range for the same materials. Using the 1 ps dye laser front end, pulses of 2 ps and 850 fs were generated using different frequency doubling crystals. The intensity of the 2 ps pulse was $3 \times 10^{16} \text{ Wcm}^{-2}$ and gave conversion efficiencies of 8 - 10% with plasma reflectivity accounting for the reduction in conversion efficiency. The 850 fs pulse produced intensities of $6 \times 10^{16} \text{ Wcm}^{-2}$ but with reduced yields of 4% for copper due to plasma reflectivity and ionization lag in the short duration of the pulse.

The results clearly indicate that a high efficiency regime (>10%) of keV x-ray conversion can be accessed using low energy discharge pumped KrF modules. This result is of considerable interest in the development of laser based x-ray generation systems for use in advanced lithography technologies.

ACKNOWLEDGEMENTS

I would like to thank my supervisor Dr. Robert Fedosejevs for his support and advice through the course of my studies and research.

I am grateful to Blair Harwood for his technical expertise and for answering my numerous questions during the development of the laser systems.

I would like to acknowledge many valued discussions in the Power Plant with my friends and colleagues Doug Vick, Ying Tsui, Masayuki Fujita, Robert Newton and Yanmin Li.

I would also like to thank Herb Gans and gentlemen of the machine shop for their patience and fine workmanship during my numerous "critical" projects.

TABLE OF CONTENTS

Abstract	
Acknowledgements	
Table of Contents	
List of Tables	
List of Figures	
List of Terms	
Introduction.....	1
X-ray Generation From Laser Plasmas	6
Coronal Plasma Processes	8
Ablation Zone Processes.....	11
X-ray Emission Processes	14
Laser System.....	20
Excimer Laser Systems.....	20
XeCl Module.....	22
KrF Module	25
KrF Laser Physics	27
Dye Laser Systems	30
100 ps Dye Laser.....	31
1 ps Dye Laser	38
Frequency Doubling and KrF Amplification	50
Beam Divergence	51
Nonlinear Optics and Pulse Length Measurement.....	52
X-Ray Experimental Methods	55
Laser Plasma Diagnostic Apparatus	55
KeV X-ray Measurement Techniques	58
X-Ray Experimental Results	67
X-ray Spectra.....	68
TGS and Pinhole Camera Measurements	77
X-ray Yield Measurements	82
ASE Dependence.....	91
Angular Dependence.....	94
Plasma Reflectivity.....	96
X-Ray Yields in Helium Background.....	98
Discussion.....	101
Conclusions.....	123
References.....	127
Appendix 1.....	135
Laser System Alignment Techniques	135

LIST OF TABLES

Table 1 Wavelengths (in Angstroms) of transitions used in calibrating the mid Z_N
spectra. The spectral features are identified in Fig. 24. After Gordon et al.⁶⁶
.....page 68

LIST OF FIGURES

- Fig. 1 Diagram of general physical structure of laser produced plasma showing electron density and temperature profiles. The ablation zone and coronal plasma are separated by the critical density surface.page 7
- Fig. 2 Schematic of resonance absorption in a plasma gradient.page 10
- Fig. 3 Block diagram of laser and target interaction systems developed by author.page 21
- Fig. 4 General internal structure diagram of excimer laser modules used in this project.page 23
- Fig. 5 High speed photodiode trace of XeCl laser pulse shape showing risetime of 5 ns and pulse length (FWHM) of 30 ns.page 26
- Fig. 6 Diagram of KrF excimer molecule energy levels as a function of atomic separation showing the B-X laser transition. The separation between the B and C levels is exaggerated to show part of the vibrational manifolds.page 29
- Fig. 7 Diagram of 100 ps dye laser system.page 32
- Fig. 8 Schematic diagram showing physical structure of quenched resonator (QR).page 33
- Fig. 9 Computer simulation of quenched resonator temporal evolution. Inner resonator produces single relaxation spike and bulk of pump energy is shunted to outer resonator.page 34
- Fig. 10 Typical streak camera picture of Coumarin 500 quenched resonator pulse shape with FWHM of 91 ps.page 36
- Fig. 11 Modulated spectral structure of quenched resonator.page 37
- Fig. 12 Diagram of 1 ps dye laser system.page 39
- Fig. 13 Streak camera picture of PTP quenched resonator output.page 40
- Fig. 14 Streak camera picture of BPBD short cavity dye laser.page 42
- Fig. 15 Schematic diagram of modulated gain structure formation in DF DL by interference of pump beams.page 44
- Fig. 16 Simulation of DF DL behaviour when pumped over threshold such that multiple pulses are produced.page 45
- Fig. 17 Diagram of physical structure of DF DL apparatus.page 47
- Fig. 18 Streak camera picture of amplified DF DL laser pulse showing resolution limited pulse length.page 49
- Fig. 19 Schematic diagram of target interaction apparatus.page 56

- Fig. 20 Theoretical response functions for *p-i-n* diodes and GaAsP diodes as a function of x-ray photon energy.page 59
- Fig. 21 Transmission characteristics of 9 μm aluminum and 2B10 filters.....page 60
- Fig. 22 Theoretical response characteristics for the four detector/filter combinations used in measuring absolute keV x-ray emissions (a) *p-i-n* diode with 9 μm Al (b) *p-i-n* diode with 2B10 (c) GaAsP diode with 9 μm Al (d) GaAsP diode with 2B10.page 61
- Fig. 23 Ratio of integrated emission under isotropic assumption to cosine power law showing that the use of the 60 degree viewing angle introduces no more than 6% error for distributions between isotropic ($\alpha=0$) and lambertian ($\alpha=1$). ...page 65
- Fig. 24 Typical densitometer scan of copper spectrum recorded on Kodak DEF film and measured using Joyce Loebel microdensitometer (NA=0.25). Some of the major neon-like lines used to calibrate the wavelength scale have been marked and are listed in Table 1.....page 69
- Fig. 25 Final keV spectra for pure target materials obtained with 120 ps pulse at intensity $1.5 \times 10^{14} \text{ Wcm}^{-2}$. Materials are (a) Titanium, (b) Iron, (c) Nickel, (d) Copper and (e) Tin.....page 71
- Fig. 26 Final keV spectra for pure target materials obtained with 90 ps pulse at intensity $8 \times 10^{14} \text{ Wcm}^{-2}$. Materials are (a) Titanium, (b) Iron, (c) Cobalt (d) Nickel, (e) Copper, (f) Zinc and (g) Tin.page 72
- Fig. 27 Final keV spectra for mixed target materials obtained with 90 ps pulse at intensity $8 \times 10^{14} \text{ Wcm}^{-2}$. Materials are (a) German Silver, (b) Brass, (c) Inconel 750.page 75
- Fig. 28 Final keV spectra obtained with "stretched" 2 ps pulse at intensity $3 \times 10^{16} \text{ Wcm}^{-2}$. Materials are (a) Titanium, (b) Iron, (c) Nickel, (d) Copper and (e) Tin. Also shown in (f) is copper spectrum obtained with 850 fs pulse at intensity of approximately $6 \times 10^{16} \text{ Wcm}^{-2}$page 76
- Fig. 29 Aluminum spectra in 1400 - 2300 eV range showing helium and hydrogen-like spectral structures. Produced with (a) 850 fs, (b) 2 ps and (c) 90 ps pulses. Note that the He α line has been permitted to saturate in order to enhance the other structures.page 78
- Fig. 30 Raw data from TGS for nickel. Recorded on Kodak 101-07 film and measured with Joyce Loebel microdensitometer (NA=0.25). (a) 120 ps pulse at $1.5 \times 10^{14} \text{ Wcm}^{-2}$ and (b) 90 ps pulse at $8 \times 10^{14} \text{ Wcm}^{-2}$page 79
- Fig. 31 Final TGS spectra in 100 - 1600 eV range obtained with 120 ps pulse at intensity $1.5 \times 10^{14} \text{ Wcm}^{-2}$. Materials are (a) Titanium, (b) Iron, (c) Nickel, (d) Copper and (e) Tin.....page 80

- Fig. 32 Final TGS spectra in 100 - 1600 eV range obtained with 90 ps pulse at intensity $8 \times 10^{14} \text{ Wcm}^{-2}$. Materials are (a) Titanium, (b) Iron, (c) Cobalt, (d) Nickel. (e) Copper, (f) Zinc and (g) Tin.page 81
- Fig. 33 Scaling of charge detected by *p-i-n* diode with 9 μm Al filter as a function of laser energy on copper target using the 90 ps pulse with the triplet focusing lens. Diode solid angle is 333 μSrpage 84
- Fig. 34 Peak conversion efficiency into 800 -1400 eV x-rays in $2\pi \text{ Sr}$ as a function of atomic number measured with the 90 ps pulse and the 120 ps pulse.page 85
- Fig. 35 Peak conversion efficiency when x-ray window is redefined to 1000 -1400 eV.page 86
- Fig. 36 Conversion efficiency into 800-1400 eV x-rays from 2 ps pulse as a function of atomic number.page 88
- Fig. 37 Conversion efficiency for copper measured at 850 fs, 2 ps and 90 ps.page 89
- Fig. 38 Conversion efficiency for copper as a function of laser pulse energy measured using 90 ps pulses. (a) Conversion efficiency data on linear scale showing rollover in high energy end. (b) Same data on log-log scale showing drop off and scaling in low energy end.page 90
- Fig. 39 Effect of ASE on conversion efficiency. (a) Data not corrected to subtract ASE effect. (b) Data corrected to subtract ASE still shows trend of increasing conversion efficiency with slowly decreasing main pulse energy.page 93
- Fig. 40 Angular dependence of emission for (a) 850 fs pulse, (b) 2 ps pulse and (c) 90 ps pulse. The estimated $\cos^\alpha(\theta)$ coefficient is listed in each figure.page 95
- Fig. 41 Measured specular reflectivity of plasma as a function of pulse length. The curve is drawn only to guide the eye through the data.page 97
- Fig. 42 Effect of helium on conversion efficiency for copper as measured with the *p-i-n* diode with 9 μm Al filter. (a) shows charge detected as a function of energy. (b) shows x-ray conversion efficiency when corrected for helium absorption.page 99
- Fig. 43 MEDUSA simulation results for a 100 ps KrF laser pulse showing spatial profiles of electron temperature (T_e in eV), electron density in terms of critical density (n_e / n_c) and the radiation from the plasma (rad) in units of $10^5 \text{ W}\mu\text{m}^{-3}$. The profiles are those occurring at the peak of the laser where peak intensity is (a) 10^{14} Wcm^{-2} and (b) 10^{15} Wcm^{-2}page 102
- Fig. 44 Sources of radiation from the MEDUSA simulated plasma. Shows the scaling of the factors for bremsstrahlung, recombination and line radiation for the plasma conditions in Fig 43b. The vertical scaling is arbitrary in order to highlight the structural comparison to the MEDUSA prediction for radiation.page 105

- Fig. 45** MEDUSA simulation results at the peak of the laser pulse for (a) 1 ps KrF pulse at 10^{16} Wcm^2 and (b) 10 ps KrF pulse at 10^{16} Wcm^2 . Shows the spatial profiles of electron temperature (T_e in eV), electron density in terms of critical density (n_e / n_c) and the radiation in the plasma (rad) in units of $10^5 \text{ W}\mu\text{m}^{-3}$...page 108
- Fig. 46** Ionization of copper according to Thomas Fermi model as a function of mass density (gcm^{-3}) and temperature (eV) showing ionization state contours for Mg like ($Z=17$) to Be-like ($Z=25$) and a range of electron density contours from 1 to 11 times critical density.page 109
- Fig. 47** Ionization timescales for copper ions under conditions shown in Figs. 43b, 45a and 45b. The figure shows the inverse of the collisional ionization rate for ions in the Al through O-like states. Note that the transition to Ne-like ions is generally marked by a significant jump in ionization time.page 111
- Fig. 48** RATION simulated aluminum spectra at (a) temperature 500 eV and electron density of 10^{23} cm^{-3} (b) temperature 300 eV and 10^{21} cm^{-3}page 114

LIST OF TERMS

2B10	2 layers of B10 filter material
ADP	Ammonium Dihydrogen Phosphate
ASE	Amplified Spontaneous Emission
BBO	Beta Barium Borate
BBOT	2,5-di-(5-tert-butyl-2-benzoxazolyl)-thiophene
BPBD	2-(4-biphenyl)-5-(4-t-butylphenyl)-1,3,4-oxadiazol
DEF	Direct Exposure Film
DFDL	Distributed Feedback Dye Laser
DMF	Dimethyl Formamide
DRAM	Dynamic Random Access Memory
FWHM	Full Width Half Maximum
GaAsP	Gallium Arsenide Phosphide
GSA	Gated Saturable Absorber
HCl	Hydrogen Chloride
IB	Inverse Bremsstrahlung
IC	Intercombination
ICF	Inertial Confinement Fusion
keV	kilo-electronvolt
KrF	Krypton Fluoride
LTE	Local Thermodynamic Equilibrium
NA	Numerical Aperture
OG530	Schott OG530 filter glass
PHC	Pinhole Camera
PTP	Para-Terphenyl
PVC	Poly-Vinyl Chloride

QR	Quenched Resonator
RAP	Rubidium Acid Phthalate
SCDL	Short Cavity Dye Laser
TAP	Thallium Acid Phthalate
TGS	Transmission Grating Spectrometer
UV	Ultraviolet
VUV	Vacuum Ultraviolet
XeCl	Xenon Chloride

INTRODUCTION

X-ray generation from laser produced plasmas has received increasing attention for many reasons in the past few years. In the study of laser plasma interactions x-ray emission has been valued primarily as a diagnostic of plasma conditions because estimates of temperature and density can be made from x-ray measurements in regimes where optical probing is not possible. Until recently, advances in the development of the understanding of x-ray emission from dense plasmas has been led by researchers in the field of inertial confinement fusion^{1,2,3,4,5}. However, x-ray generation from laser plasmas is beginning to develop into a separate subfield of laser plasma interactions as a result of advances in the ability to produce high intensity ($>10^{14}$ W / cm²) laser radiation with relatively small laser systems. These advances are largely the result of developments in ultrashort pulse generation technology. This has led to work in developing diverse applications such as x-ray lasers, x-ray microscopy and x-ray lithography.

Inertial confinement fusion (ICF) has generally led the field in the development of the understanding of laser plasma interactions. This is because ICF is one of the two leading approaches to harnessing nuclear fusion for energy generation (the other being magnetic confinement fusion) and on this basis has received substantial funding in many countries. ICF is based upon the concept of using high intensity laser pulses to compress and heat a fuel pellet of deuterium and tritium until a thermonuclear reaction is ignited and energy is released. The concept is simple but there are many physical issues to be addressed in order to be able to do this in a manner where the energy released exceeds the energy invested in generating the laser pulses. Not only is x-ray radiation a valuable source of data for these high density plasmas but it is also an important component of energy transport into as well as out of the fuel plasma and must be understood in order to develop ICF as a viable mechanism for power generation.

In addition to an interest in understanding the basic processes of nature there is a new desire to harness the ability of laser generated plasmas to produce coherent (laser) x-ray radiation⁶ by judicious selection of the interaction parameters (target material and geometry, laser intensity, pulse length and wavelength). Collisionally pumped coherent x-ray emission has been demonstrated using laser produced plasmas in the nanosecond pulse length regime^{7,8,9}. There is also the possibility of x-ray emission from transient recombining ionization regimes driven by ultrashort pulses (< 10 ps) which will yield coherent x-ray radiation¹⁰. In addition x-ray lasers pumped by direct photoionization⁶ from short, intense x-ray pulses have been proposed. X-ray lasers constitute a field of continuing development because of potential applications in fields such as x-ray microscopy^{11,12}. If coherent sources can be developed in the so called "water window" (23 - 44 Å) where water transmits and the carbon in organic materials absorbs then it will be possible to image even the smallest structures in living cells¹³.

X-ray lithography is one of the new application areas stimulating investigations into optimizing keV x-ray generation. Currently, x-ray lithography is expected to succeed optical lithography in the production of dynamic random access memory (DRAM) chips by the end of this century. However, it is worth noting that the demise of optical lithography has been predicted for a number of years¹⁴. The transition from g-line (546 nm mercury light) to i-line (365 nm mercury light) has delayed the need for major retooling for much of the production of large scale integrated microcircuits. Recently, the transition in optical lithography has continued and it appears likely that KrF lasers (248 nm) will replace i-line lamps for large scale production in the development of 0.35 μm down to 0.25 μm features and that ArF (193 nm) lasers may provide even further advances down to the 0.2 μm feature level and beyond^{15,16}. In addition to the transition in wavelengths there have been ongoing advances in lithographic techniques such as phase shifting which have allowed improvements in resolution using existing technology and tools. This type of advancement in the optical lithography technology

area has forestalled the implementation of x-ray lithography as a production tool. In spite of these advances x-ray lithography is still expected to take over when the fundamental limits of optical lithography are reached.

There are two wavelength regimes which are being investigated for possible use in production of the sub-0.2 μm size circuit features which will be needed to develop 256 Mbit and 1 Gbit memory chips. One regime is very soft x-rays in the 100 eV photon energy range where it is now possible to produce reasonable (60%) reflectivity coatings¹⁷. This allows the development of x-ray optics which can be used to demagnify an x-ray mask and expose a resist without having the mask in close proximity to the resist surface. This technique is called projection lithography¹⁸. The other regime proposed for development of x-ray lithography is harder x-rays in the 1 keV region where high reflectivity coatings do not exist and therefore the proposed technique for exposing resists is to hold the x-ray mask in close proximity to the resist and then to expose with x-rays incident from the mask side. The advantage of using keV x-rays is that the diffraction of the radiation from the mask features is small (within a given proximity gap range) which means the minimum feature size is not determined by the wavelength of the x-rays but by the ability to produce masks with the appropriate feature size. Another advantage of x-rays in this regime is that mask opacity can be controlled by selection of materials which allows for the possibility of techniques like phase shifting being implemented. Mask substrates can be made from materials like SiC and SiN which have reasonable mechanical properties (rigidity and strength) as well as transparency at thicknesses near 1 μm . Much of the development in the x-ray lithography field is geared towards the use of synchrotron radiation as the exposure source. However, synchrotron facilities are enormously expensive (on the order of \$100 million) and while there is little doubt that such a facility would be most appropriate for mass production of DRAM chips there are few companies capable of this type of capital investment to develop an unproven technology. On this basis there is substantial interest in the possibility of using

high repetition rate laser produced plasmas as x-ray sources for much of the development process as well as for small scale and specialized production processes. A single laser based system would probably cost on the order of a few million dollars.

The subject of this thesis is an investigation into the generation of keV x-rays using low energy (5 - 50 mJ), picosecond (1 - 100 ps) KrF laser pulses. These pulses are able to access the high intensity regime (10^{14} - 10^{16} Wcm⁻²) required to produce hot enough plasmas to emit efficiently in the keV x-ray range. The first and largest stage of the work was to build a laser system and target interaction facility oriented towards investigation of short pulse KrF laser plasma interactions. The second stage of the research was to engage in a set of experiments which would provide an indication of which regimes of pulse length and energy could be optimal for keV x-ray generation using discharge pumped KrF lasers which typically provide amplified short pulse (<1 ns) energies in the 30 - 50 mJ range. Basic construction of the laser systems plus the target interaction and data acquisition infrastructure entailed approximately four years work. The last two years have been more focused on laser system optimization, the target experiments and publication of the data as it became available.

The remainder of the thesis will be presented in six chapters. First, the background theory related to the generation of x-rays from laser produced plasmas will be presented. Next, details of the laser system will be presented, including both theoretical considerations and experimental results. Thirdly, the experimental methods used to measure keV conversion efficiency will be examined. Fourth, the experimental x-ray results will be presented including some material which has been published in the Journal of Applied Physics¹⁹ and in Applied Physics Letters²⁰. The results will then be discussed in terms of simple theoretical modeling of plasma behaviour in the various laser pulse length regimes and plasma physics simulation of the experimental conditions. Finally, conclusions will be presented regarding the use of KrF lasers in the efficient generation of keV x-rays and issues will be identified where further study is needed both

in terms of the physical processes and the technological issues which must also be addressed in order to develop commercial applications.

X-RAY GENERATION FROM LASER PLASMAS

When a sufficiently intense laser pulse is incident on a solid target a portion of the target surface is melted, vaporized and ionized. The details of the initial melting and vaporization process are strongly material and laser pulse dependent but for laser radiation over a threshold value (typically $>10^8 \text{ Wcm}^{-2}$) the end result is always the formation of a region of ionized material (plasma) where the interaction physics changes and the more broadly applicable concepts of laser plasma interactions can be discussed.

The general physical structure of a laser generated plasma is shown in Fig. 1 which shows the electron density (n_e) and the electron temperature (T_e) spatial profiles. In terms of the laser plasma interactions there are two basic regions which are separated by a characteristic electron density defined by the laser wavelength. The outer region is known as the coronal (underdense) plasma and the inner region is called the ablation zone (overdense plasma). The two regions are delineated by the surface where the oscillation frequency of the laser field becomes equal to the local electron plasma frequency. At this surface the electromagnetic wave is no longer able to penetrate the plasma and the plasma reflects the laser light. The electron density (hence the terms over/underdense) at which this occurs is called the critical density (n_c), this density is expressed as:

$$n_c = 1.1 \times 10^{21} \lambda_L^{-2} \text{ cm}^{-3} \quad (1)$$

where λ_L (μm) is the wavelength of the laser in vacuum. In the case of KrF lasers this density is $1.81 \times 10^{22} \text{ cm}^{-3}$ where λ_L is $0.248 \mu\text{m}$. The coronal plasma is dominated by the physics of the interaction between the oscillating electromagnetic field and the plasma. The most important effect is the transfer of energy from the electromagnetic wave to the plasma. Also associated with the underdense plasma are many types of wave interactions which can affect the energy transfer from the laser to the plasma. The ablation region is dominated by the physics of energy conducted by electrons and to a

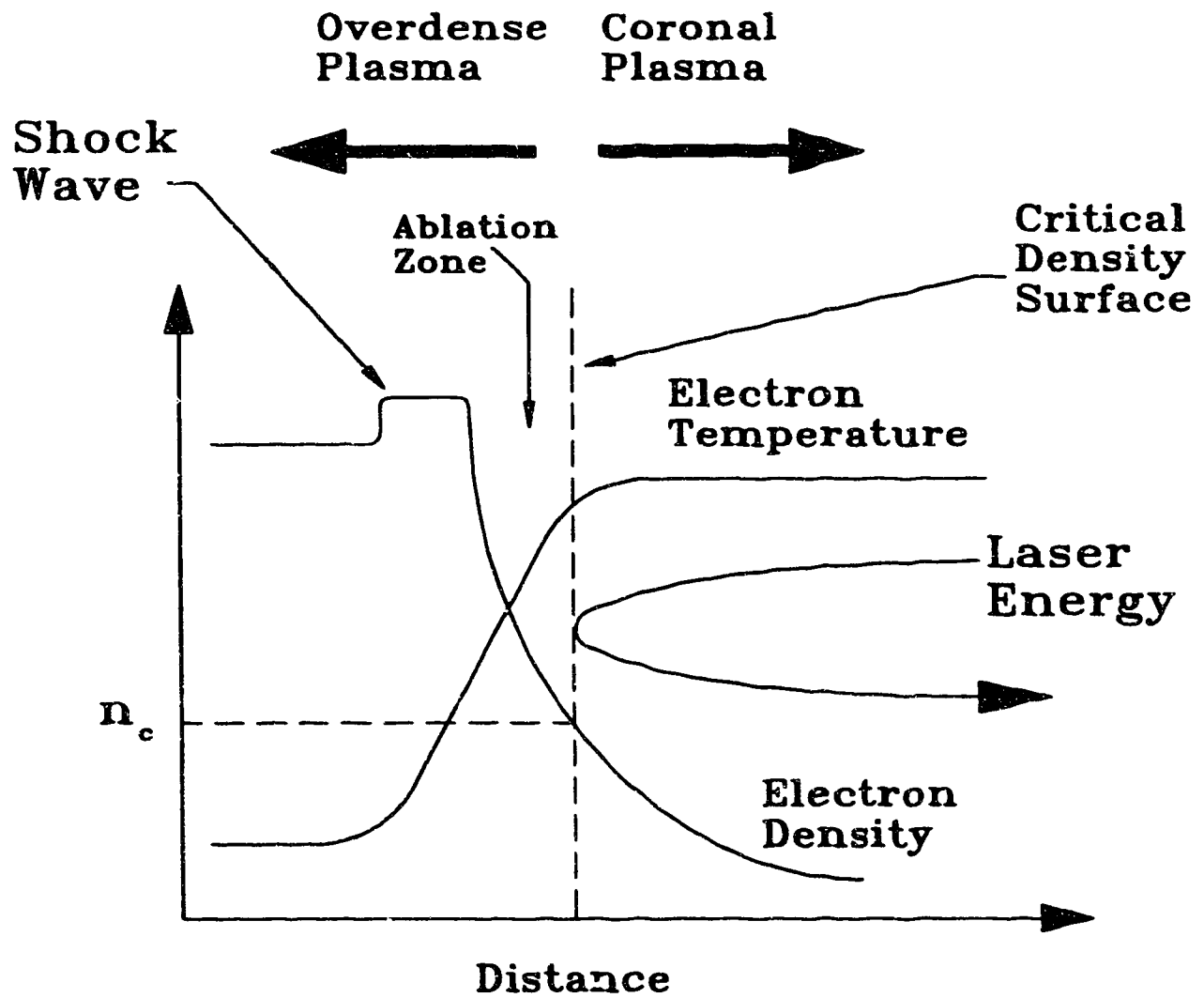


Fig. 1 Diagram of general physical structure of laser produced plasma showing electron density and temperature profiles. The ablation zone and coronal plasma are separated by the critical density surface.

lesser extent by x-ray radiation generated inside the overdense plasma. Energy deposited in the coronal plasma is conducted inwards by electrons since the light cannot penetrate beyond n_c . The ablation region is characterized by a thermal wave propagating into the target material. The ablation region is generally preceded by a shock wave in which the material is compressed and slightly heated.

Coronal Plasma Processes

The coronal plasma is generally characterized by smooth temperature and density profiles. The coronal plasma can usually be considered to be isothermal for simplicity in analytic description. This is a result of the high thermal conductivity of the electrons in the hot coronal plasma. The transfer of energy from the laser to the coronal plasma is usually dominated by collisional randomization of the electrons oscillating in the electric field of the laser. Collisional energy transfer requires the presence of the much heavier ions because electron-electron collisions are not able to produce net momentum exchange. This process of radiation energy being converted to thermal energy by electron-ion collisions is called inverse bremsstrahlung (IB). In a broad sense the physics of this process can be described by the classical motion of an electron (charge $-e$) with thermal velocity (v_e) near an ion (charge Ze) where the orbit of the electron around the ion produces a 90° change in the direction of the electron motion. More exact calculations require the incorporation of kinetic theory and can become extremely complex when the rate of energy transfer to the electrons is faster than the rate at which the electrons are able to distribute the energy among themselves (thermalize). Under the general assumption of a Maxwellian energy distribution for the electrons, the collision frequency which determines the rate of energy absorption by a plasma due to inverse bremsstrahlung (ν_{ib}) has been calculated²¹ to have the behaviour:

$$\nu_{ib} \propto \frac{Zn_e^2}{n_c T_e^{3/2}} \ln \Lambda \quad (2)$$

where n_e is the electron density, T_e is the electron temperature, Z is the charge of the ions and $\ln\Lambda$ is the Coulomb logarithm. The Coulomb logarithm is the log of the ratio of maximum to minimum impact parameters in the electron ion collision process. Essentially, it describes the range over which electron ion interactions can occur with the outer limit being the distance at which the rest of the plasma screens out electrostatic fields (Debye length). It can be seen that the inverse bremsstrahlung absorption rate of the plasma is maximized for higher densities, lower temperatures and highly ionized plasmas. One effect of the temperature dependence is that as the plasma becomes sufficiently hot the absorption due to inverse bremsstrahlung is reduced and can result in a reduction of energy transfer from the laser to the target. When this occurs there may be substantial reflection from the critical density unless other mechanisms for absorption take over. An example of a second important absorption mechanism for these plasmas is resonance absorption.

The basic principle behind resonance absorption is usually described in terms of a polarized plane electromagnetic wave incident at an angle to an infinite plasma with a gradient in one direction. Figure 2 shows this idealized situation where an obliquely incident wave is reflected at a density of $n_e \cos^2 \theta$. If the polarization of the EM wave is such that the electric field oscillates in and out of the plasma gradient (p polarization) it is possible to excite electron plasma waves which propagate outwards from the plasma. This occurs because the electric field penetrates beyond the $n_e \cos^2 \theta$ point as an evanescent wave (exponential decay). In many cases resonance absorption must be considered as a source of plasma heating because laboratory lasers generally contain "hot spots" which result in physical modulation of the plasma density profile. As a result, even when the laser is perpendicular to the target surface (the case for most of the experiments discussed in this thesis) there are regions where the electric field can excite electron plasma waves and enhance absorption of the laser energy.

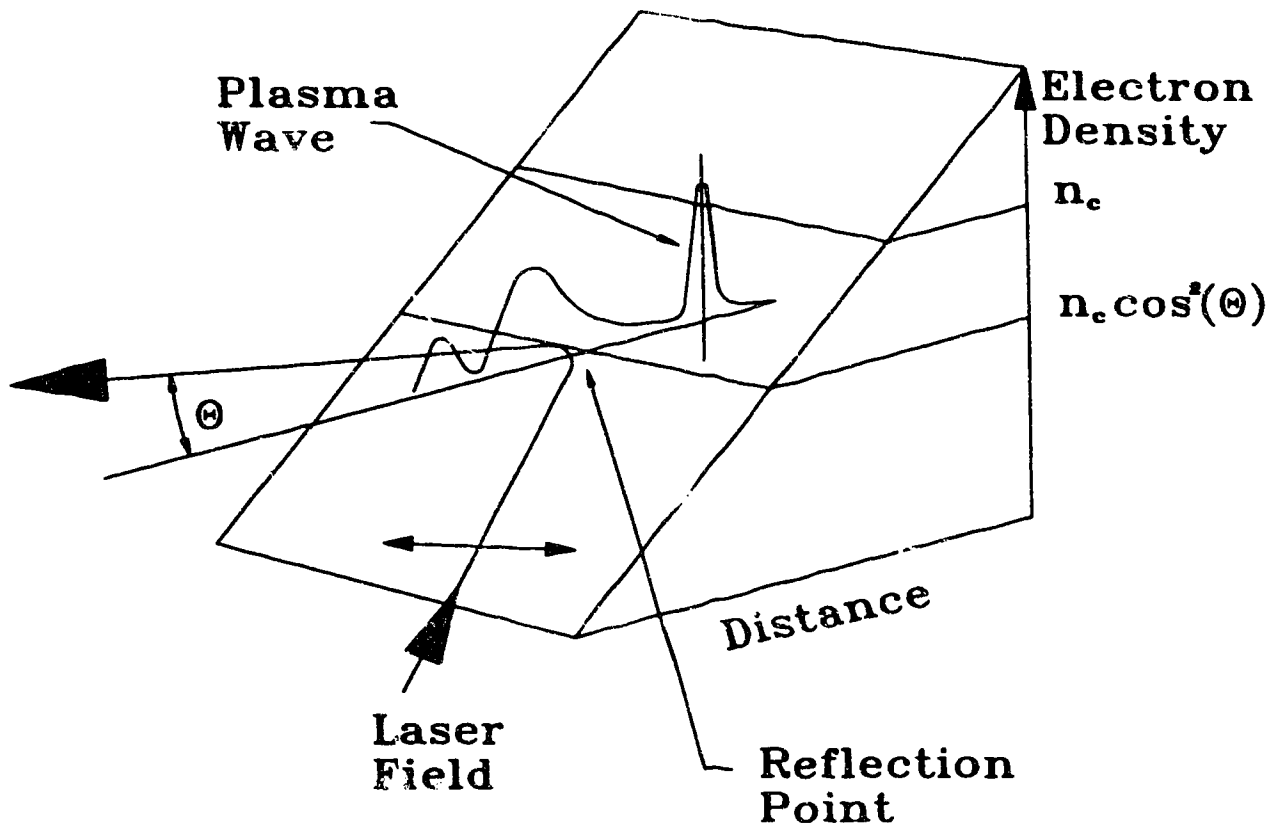


Fig. 2 Schematic of resonance absorption in a plasma gradient.

In addition to mechanisms for absorption of the laser energy there are also processes where the laser interacts with waves in the underdense plasma and the result is a reduction in energy transfer to the plasma. Stimulated Brillouin Scattering (SBS) is the result of the incident EM wave generating an ion acoustic wave (sound wave) in the underdense plasma and in the process a reflected (scattered) light wave is generated which can result in substantial losses of energy. A similar process is Stimulated Raman Scattering (SRS) where an electron plasma wave is generated and a reflected light wave is produced as well. SRS only occurs in the plasma where the density is less than quarter critical. SRS and SBS are the subject of extensive investigation in ICF literature because they represent significant loss mechanisms in the process of attempting to heat and compress a fuel plasma. These processes are part of a broader field of instabilities where a variety of waves are generated in the underdense plasma²². Generation of strong electron plasma waves is undesirable for ICF targets because if the amplitude is large enough electrons can be accelerated to high energies and can transport significant amounts of energy into the target ahead of the shock waves resulting in preheat of the fuel material.

Ablation Zone Processes

The ablation zone is characterized by gradients in temperature and density which may become so steep that the physics of electron heat conduction is modified because the mean free path of the electrons exceeds the scale length of the gradients. The most important consequence of this is that heat conduction is reduced to a small fraction of what would be expected from standard heat conduction calculations. This is the "flux limited" regime²². Another important physical characteristic of the ablation zone is the development of a rocket effect where hot dense plasma expands rapidly outward towards the coronal zone and at the same time generates a strong compressional and thermal shock wave which propagates into the target.

One of the most important processes in the evolution of a laser produced plasma is the ionization of the material as it makes the transition from the cold solid target through the ablation zone and into the coronal plasma. Calculation of the ionization state of material within specific regions is a complex process even for pulse length regimes where processes approach steady state. In the case of high density plasmas where energy exchange is dominated by electron collisional processes (local thermodynamic equilibrium LTE) the ionization can be described using the Saha equation²³:

$$\frac{n_{z+1}}{n_z} = \frac{G_{z+1}}{G_z} \frac{2}{n_e \lambda_e^3} \exp\left(\frac{-X_z}{T_e}\right) \quad (3)$$

where n_{z+1} and n_z are the populations of ions in the states Z and Z+1, G is the statistical weight of the state, λ_e is the thermal electron deBroglie wavelength and X_z is the ionization energy of state Z. The Saha equation is analytically simple but has restricted applicability because of the requirement of electron collisions dominating all processes (including radiative transitions). A common rule for application of the Saha equation is that²⁴:

$$n_e > 1.7 \times 10^{14} \sqrt{T_e} X_z^3 \text{ cm}^{-3} \quad (4)$$

where T_e and X_z are in eV. Even for moderate values of T_e and X_z this leads to very high density requirements (e.g. $T_e=300$ eV and $X_z=1000$ eV implies $n_e=164 n_c$ for a KrF laser plasma). The other extreme of plasma ionization is based on the assumption that the plasma is completely transparent to radiation produced by recombination and that the density is low enough that collisional deexcitation is negligible. This regime is called coronal equilibrium in reference to theoretical development to describe the plasma in the solar corona. Coronal equilibrium is described by the equation²⁵:

$$\frac{n_{z+1}}{n_z} = \frac{S_z}{\alpha_{z+1}} \quad (5)$$

where S_z is the collisional ionization rate and α_{z+1} is the recombination rate.

Application of the coronal model is restricted to low density plasmas and a general rule for suitability can be expressed as²⁴:

$$n_e < 6 \times 10^{10} (Z+1)^6 T_e^{1/2} \exp\left(\frac{(Z+1)^2}{10T_e}\right) \text{ cm}^{-3} \quad (6)$$

This type of equilibrium is generally not useful for describing laser plasmas generated from solid targets because the density limit is very low compared to typical values in the interaction region (e.g. $T_e=300$ eV and $Z=19$ (neon-like copper) implies $n_e \approx 0.005 n_c$ for KrF).

The regime in between LTE and coronal equilibrium is described by rate equations which take into account all significant collisional and radiative processes occurring in the plasma. This type of description is the collisional radiative (CR) regime and a full description requires detailed calculations of all processes contributing to the total populations in the various ionization states and to the excited state population within each ionization state. Some simplifications can be made such as assuming LTE for excitation states near the continuum but in general collisional radiative ionization is a regime requiring intensive computational simulation. The picture becomes even more complex when the time dependence of the ionization must be accounted for. This is the case when short laser pulses are used to generate plasmas. Laser intensities which might produce particular ionization states under long pulse conditions may fail to produce those same states because the duration of the pulse is not sufficient to allow the atoms to ionize. On the other hand shorter pulses produce higher intensities for a given amount of energy (such is the case for KrF laser pulses) which may compensate for the time lag in ionization by producing higher temperature and density regimes leading to faster ionization rates.

In spite of the complexities of describing the details of the ionization and excitation processes in laser produced plasmas there are broad guidelines which can provide some insight into the results observed. When a plasma is heated the electrons are stripped off the atoms such that the ions reach a state of ionization where the ionization energy of the electrons that are stripped off is of the order of 3 to 7 times the electron temperature of the plasma. One important factor which affects the ionization balance is the jump in ionization energies which occurs between closed electron shells (transition in the principal quantum number n). For instance, to ionize a copper atom (atomic number $Z_N=29$) from a sodium-like state (+18) to a neon-like state (+19) requires 676 eV but to remove the next electron and make it fluorine-like (+20) requires 1542 eV an increase in ionization energy by a factor of 2.28. This behaviour favours the stabilization of the ionization of the plasma near closed shell configurations (i.e. Ne-like) and instead of further ionization, electron thermal energy is channeled into outer shell excitation resulting in increased line radiation.

X-ray Emission Processes

X-ray emission from the various plasma zones occurs as a result of three basic processes. Firstly, there is the radiation which occurs as a result of electron-ion collisions resulting in strong acceleration of the electrons (without recombination), this is known as bremsstrahlung (also known as free free emission referring to the initial and final states of the electron). Secondly, there is radiation resulting from electrons which recombine with ions in the plasma and release the energy of recombination as radiation (free bound radiation). Recombination radiation is concentrated near the ionization energy levels of the atoms forming the plasma. Bremsstrahlung and recombination radiation are valuable as a plasma diagnostic because in hot plasmas these two combine and extend into higher energy ranges than line radiation (and so can be isolated and measured) and in particular have exponential spectral distributions of the form²⁵:

$$P_{ff}(E) + P_{rb}(E) = 1.52 \times 10^{-32} n_e n_i Z^2 T_e^{-1/2} \exp\left(\frac{-E}{T_e}\right) \quad (7)$$

$$\times \left[g_{ff} + G_n \frac{\xi}{n^3} \frac{X_z}{T_e} \exp\left(\frac{X_z}{T_e}\right) + 2 \sum_{v=n+1}^{\infty} G_v \frac{Z^2 R_y}{v^3 T_e} \exp\left(\frac{Z^2 R_y}{v^2 T_e}\right) \right] \text{ Wcm}^{-3} \text{ eV}^{-1}$$

where n_e is electron density, n_i is ion density, Z is the ion charge, T_e is the electron temperature, E is the x-ray photon energy, g_{ff} and G are "gaunt" factors which are quantum correction factors to classically derived expressions for the radiation. The first term in the sum (g_{ff}) is the contribution from bremsstrahlung emission. The second part represents emission from recombination into the first unfilled electron shell (principal quantum number n) of the ion. ξ is the number of available electron positions in that shell (out of a possible $2n^2$). X_z is the ionization energy for the position being filled. The third part of the expression represents recombination into completely unfilled electron shells ($n+1$ and higher) which are approximated using a hydrogenic structure where R_y is the ionization energy of hydrogen (13.6 eV). Recombination radiation and bremsstrahlung have a similar exponential energy dependence but recombination radiation has a step function at each ionization stage because it not possible to emit less energy than the ionization energy of the state into which the electron is recombining. As a result of this step function recombination radiation tends to swamp bremsstrahlung emission in most plasmas. For applications in keV x-ray lithography these types of radiation are of little value because their emission is lower in intensity than line radiation.

However, they are useful because of the simple exponential spectral structure ($\exp\left(\frac{-E}{T_e}\right)$)

which allows a temperature measurement from hard x-rays (typically above the 2 - 3 keV range).

The third and often most important component of the x-ray radiation emitted from a plasma is line radiation from bound outer shell electrons of the ions. Line radiation is generated by two mechanisms: one is the cascade of recombining electrons from relatively high energy states down to the ground state, the other source is excitation of bound electrons by free electrons. The rate of collisional excitation is given by $\langle \sigma_{ij} v \rangle$ which is the collision cross section for the transition ij averaged over the electron velocity distribution (v) which is assumed to be maxwellian. The expression for $\langle \sigma_{ij} v \rangle$ is given²⁵ by:

$$\langle \sigma_{ij} v \rangle = 3.15 \times 10^{-7} \bar{g} f_{ij} \frac{R_y}{E_{ij}} \left(\frac{R_y}{T_e} \right)^{1/2} \exp\left(\frac{-E_{ij}}{T_e} \right) \quad \text{cm}^3 \text{ s}^{-1} \quad (8)$$

where f_{ij} is the oscillator strength of the ij transition with energy E_{ij} and \bar{g} is the gaunt factor. Recombination cascade radiation is generally a much smaller contributor to line radiation than electron excitation. For keV x-ray emission in the present experiments line radiation is the most important source since the other forms are concentrated in the softer portion of the spectrum. The amount of line radiation increases strongly with the number of outer shell electrons as the number of available excitation states increases. For this reason materials which are ionized to their K (principal quantum number $n=1$) shell are poor emitters of line radiation compared to L ($n=2$) shell ions since the number of outer shell electrons goes from maximum 2 to maximum 8. For M($n=3$) shell and N($n=4$) shell ions the change is characterized by a broadening of the spectral features into bands as opposed to strong line structure because the increase in the number of outer shell electrons has the effect of increasing the number of possible excitation configurations resulting in overlap between features.

The strong correlation of x-ray emission with electron shell structure was observed in early x-ray emission studies performed using CO₂, ruby and Nd:Yag lasers in the nanosecond pulse length regime^{26,27,28}. More recent calculations and

experiments^{29,30} aimed at studying higher keV conversion efficiency regimes have demonstrated that this dependence of x-ray conversion efficiency on atomic number continues to be observed with lasers operating in the ultraviolet as well. These studies have shown that within a given x-ray window there are particular values of atomic number for which emission can be maximized corresponding to appropriate shell configurations (K, L, M, N, O). The particular value of atomic number (Z_N) for which emission is optimal varies with the position of the x-ray window of interest. For keV emission (defined as 750 - 2000 eV by Alaterre et al.²⁹) the L and M shells are predicted to be the most efficient x-ray producers and the optimal species for each shell is near $Z_N=29$ (copper) and $Z_N=54$ (xenon) respectively.

Line and band radiation have the advantage of being radiatively strong as well as being spectrally narrow (at least in comparison with other forms). Equation 8 for the collisional excitation rate would appear to lead to maximum emission at $T_e = 2E_{ij}$ but this is misleading because the atoms would in fact be ionized well beyond the state which gave rise to the shell structure being excited. The implication is that line emission is maximized at the temperature which gives rise to the largest number of ions in the desired ionization state. The x-ray photon emission rate per unit volume is given by $n_e n_i \langle \sigma_{ij} v \rangle$ (photons $\text{cm}^{-3}\text{s}^{-1}$) therefore the maximization of conversion efficiency occurs for maximum density/volume of plasma ionized to the correct stage. Plasma ionization (density, volume and temperature dynamics) is a highly complex issue and depends strongly on the laser pulse that drives the interaction in terms of intensity and duration as well as other parameters. Computer simulations of plasma hydrodynamics and atomic physics are of great value in understanding the results of experimental laser plasma interactions and will be discussed in a later section.

The efficiency of emission of x-rays from laser generated plasmas has been investigated by a number of groups in the past. Among the measurements of overall x-ray conversion efficiency the highest are those of Kodama et al.³¹ where total x-ray

conversion was estimated to be 80% from a 400 ps pulse at 260 nm and a strong dependence on laser wavelength was demonstrated (increasing as wavelength was decreased). Measurements by Popil et al.^{30,32} at the University of Alberta have yielded 54% total conversion efficiency using a 1.8 ns KrF laser pulse. Most notable in the keV field have been the results of Chaker et al.³³ They have found that using 260 nm laser light it is possible to obtain ~13% conversion efficiency into 750 - 2000 eV x-rays from copper. In their experiment this was achieved using a frequency quadrupled Nd:glass laser with a 500 ps pulse length and 10 J of energy focused to intensities up to $4 \times 10^{14} \text{ Wcm}^{-2}$. At the fundamental Nd:glass wavelength of 1.06 μm Chaker et al. have observed reduced keV yields of 6% from copper targets indicating significant advantage in using UV lasers which is in agreement with Kodama's results. The principal difference between the results at the two wavelengths is the density to which the laser radiation is able to penetrate. The limiting density is the critical electron density (n_c) and for 1.06 μm in comparison to 0.248 μm light the ratio in densities is approximately 18 which means KrF light can penetrate to 18 times the density that Nd:glass light can reach. This is an important factor in terms of being able to couple laser light into heating the dense target material as opposed to the low density coronal plasma.

Large laboratory laser systems, such as the ones used in experiments mentioned above are not currently capable of generating pulses at significant repetition rates and thus are valuable for establishing the physics of x-ray generation but not for generating substantial sustained fluxes. High repetition rate excimer lasers operating as oscillators produce pulses with typical pulse lengths of tens of nanoseconds. Experiments³⁴ with excimer lasers operating in this mode have yielded low conversion efficiencies (only 0.3%) because they are unable to achieve the high intensities ($>10^{14} \text{ Wcm}^{-2}$) needed to heat the plasma effectively. A second problem associated with the long pulse regime is that as the plasma expands it eventually becomes too large for the laser to heat effectively and the x-ray emission shuts off while the laser is still on. The solution to these

problems is to compress the laser energy into a short pulse and increase the intensity to the desired range. However, excimer lasers cannot store their optical energy for more than a few nanoseconds and thus a series of pulses (pulse train) is required to effectively extract the energy from an excimer module. Experiments performed with a high repetition rate XeCl laser operating in the pulse train mode have yielded keV efficiencies on the order of 2.5% under high repetition rate conditions and 5% under single pulse conditions³⁵. One of the aims of this project was to demonstrate that it is possible to achieve the high efficiency (>10%) regime of conversion into keV x-rays using a KrF laser which can be scaled as a high repetition rate system.

LASER SYSTEM

The laser system developed during this project is modeled after systems developed over a number of years by Szatmari and Schafer at the Max Planck Institute in Gottingen^{36,37,38,39,40}. They have pioneered the development of ultrashort pulse excimer laser systems and using their published results a similar system has been developed. The laser system is shown schematically in Fig. 3 and consists of a XeCl ($\lambda = 308$ nm) excimer laser module which is used to pump one of two dye laser systems which produce green light ($\lambda = 497$ nm) pulses of approximately 100 ps and 1 ps respectively. Throughout this thesis the laser systems will be referred to by their nominal pulse lengths for simplicity since the actual pulse lengths generated by the systems have changed during the development process. The green laser pulses are frequency doubled in a nonlinear crystal to a wavelength of 248.5 nm and injected into a KrF amplifier where they are amplified in two passes to a typical energy of 50 mJ. There is an evacuated pinhole spatial filter between the two KrF amplification passes which reduces much of the amplified spontaneous emission (ASE) that would otherwise accompany the main pulse. After the final pass in the KrF amplifier the pulses are steered to a target chamber where the interaction experiments are conducted. Most of the experiments were conducted under vacuum (5×10^{-5} torr). However, additional experiments were conducted under atmospheric helium to verify the applicability of helium as a background gas for keV x-ray lithography.

Excimer Laser Systems

Excimer lasers are an important class of lasers both scientifically and industrially because of their ability to produce moderately coherent, high intensity ultraviolet radiation and their ability to support a wide range of pulse lengths ranging⁴¹ from 100 ns down to 60 fs. Scientifically, excimers are valuable for investigations ranging from

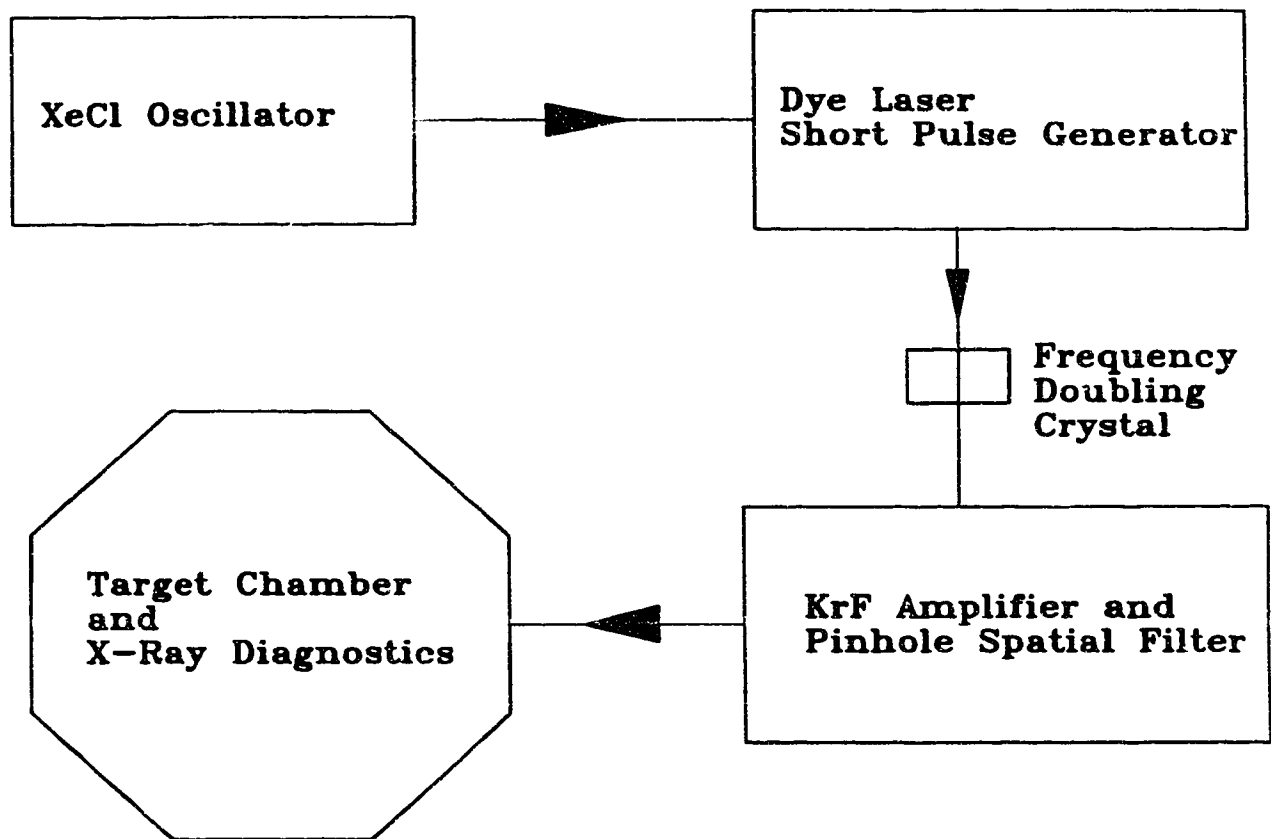


Fig. 3 Block diagram of laser and target interaction systems developed by author.

laser plasma interactions, atomic fluorescence and multiphoton ionization⁴² to ultrafast pump and probe experiments in biology which take advantage of the full range of possible pulse lengths. Industrially, excimers are important because they are relatively efficient (typically a few percent) in terms of producing high intensity radiation from electricity. More importantly though, excimer lasers are available which can deliver several hundred watts of sustained average power and research is advancing rapidly to increase this to the kilowatt level⁴³. It should be noted that there are two basic classes of excimer laser devices. The systems to be discussed in this thesis are discharge pumped lasers where the electrical energy of a high voltage storage system is deposited in a gas by virtue of a self-sustained glow discharge. The other type of system which has been developed primarily for scientific investigations is the e-beam pumped laser where energy is deposited kinetically from highly accelerated electrons injected into the gas from a vacuum diode accelerator. E-beam systems are valuable for achieving large energies (kilojoules) in a single pulse but cannot be run at any significant repetition rate. Discharge systems, on the other hand, can be run at very high repetition rates (500 hz for some commercial systems) but do not produce such large energies in a single pulse (typically hundreds of millijoules).

XeCl Module

The first stage of this project was initiated in May 1987 and entailed the construction of the XeCl excimer module. The design of the module was adapted from an earlier series of KrF modules built for the U of A nanosecond KrF laser system. The discharge excimer lasers developed at the University of Alberta consist essentially of the components shown in Fig. 4. An energy storage capacitor (C1) is connected to a set of secondary capacitors (C2) via a high speed high voltage switch (spark gap SG1). The secondary capacitors are connected between an electrode and the center ground plate. The laser gas is contained by a dielectric chamber (L) which separates the electrode and

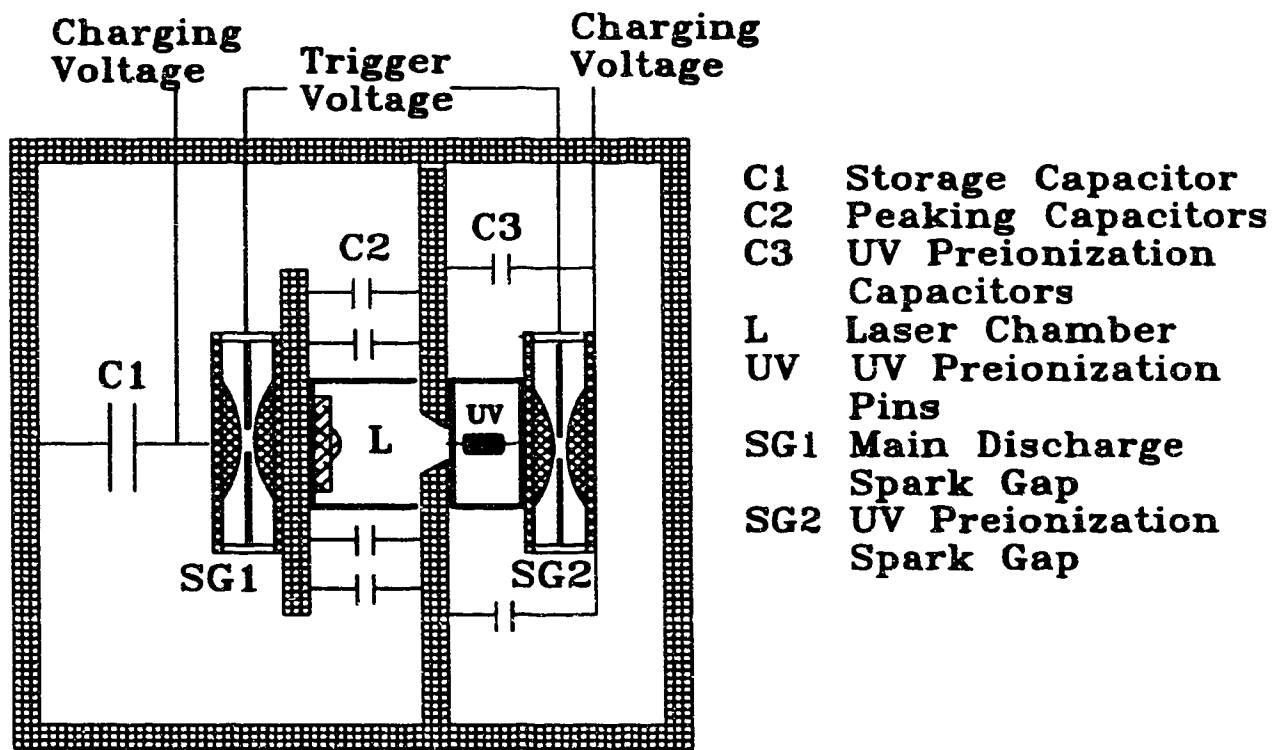


Fig. 4 General internal structure diagram of excimer laser modules used in this project.

the ground plate. The discharge is driven by closing SG1 which connects C1 to C2 and the energy is transferred to C2 resulting in a rapid rise of the voltage between the electrode and the ground plate. In addition to the circuit which drives the main discharge there is also the preionization circuitry. The preionization circuit is similar to the main discharge with the exception that there is only one set of capacitors (C3) used to store the energy. The preionization is provided by high voltage sparks sliding over a dielectric surface producing hard UV radiation which shines through the perforated screen that forms part of the ground electrode and into the laser chamber. Preionization of the laser gas is critical to the proper operation of discharge excimer lasers. The purpose of the preionization is to provide a minimum density ($10^6 - 10^7 \text{ cm}^{-3}$) of free electrons⁴⁴ from which the avalanche discharge can be seeded. The high voltage discharge which drives the population inversion is inherently unstable and eventually collapses into current filaments resulting in arcing which terminates the laser action. The preionization electrons allow the discharge to initiate as a uniform glow during which the electrons accelerated by the high voltage drive the chemical reactions which result in the formation of the excimer molecules.

The principal differences between the XeCl module used in this project and the previous series of modules were a reduction in overall size of the module and the attempted use of an analytically designed electrode profile called a Chang profile⁴⁵. The Chang profile is the result of electrostatic calculations where the design objective is to produce a maximally uniform field between two isolated electrodes. Unfortunately, the Chang profile proved to be inadequate due to severe arcing in the laser gas and was eventually replaced with a modified elliptical profile which was designed by the author specifically for the module. The design of the elliptical profile was generated using the electrostatic field modelling code POTENT⁴⁶ and took into account the field distorting effects of the laser body walls which are not accounted for in the Chang model. The electrode has a length of 43.5 cm and gives a discharge with a cross section of 12 by 18

mm. The XeCl module has been the source of very serious, ongoing problems and has been the principal restraining factor in the progress of this work. In addition to the time needed to redesign and remachine the electrode additional problems were encountered in the initial use of Delrin plastic as the dielectric insulator. Under the duress of the corrosive HCl and the shock of the discharge the plastic stress-cracked and failed. Eventually the Delrin was replaced with Poly Vinyl Chloride (PVC) which is still not ideal but is inexpensive and is adequate for the purpose. While these failures were the worst of the problems encountered with the XeCl module there are still ongoing problems of gas lifetime and electrode damage due to arcing. Ultimately, these problems will only be resolved by a basic redesign of the laser body. In spite of these problems the module was brought to an operational status where it would routinely produce 130 mJ pulses with a pulselength of 30 ns and a risetime of 5 ns. Figure 5 shows the pulse shape of the XeCl beam measured using a high speed Hamamatsu photodiode. It is important to note that the risetime of the XeCl pulse is one of the most critical parameters in the entire system. This is due to the fact that the dye laser pulses are generated as transient pulses from the leading edge of the pump pulses and at every stage the pulselength that is produced is directly dependent on the risetime of the preceding pulse. As a result any deviation in the behaviour of the XeCl module generally has a major impact (usually bad) on the operation of the rest of the system.

KrF Module

The KrF module which is used as the amplifier for both the 100 and 1 ps systems represents some significant improvements over the design of the XeCl module. The modified elliptical electrode profile was used from the beginning in this module and has provided relatively trouble free operation. One major problem which was common to both modules was the failure of the Delrin plastic body pieces. Both pieces in the KrF module were replaced with PVC but this failed (on the main discharge side) as well, due

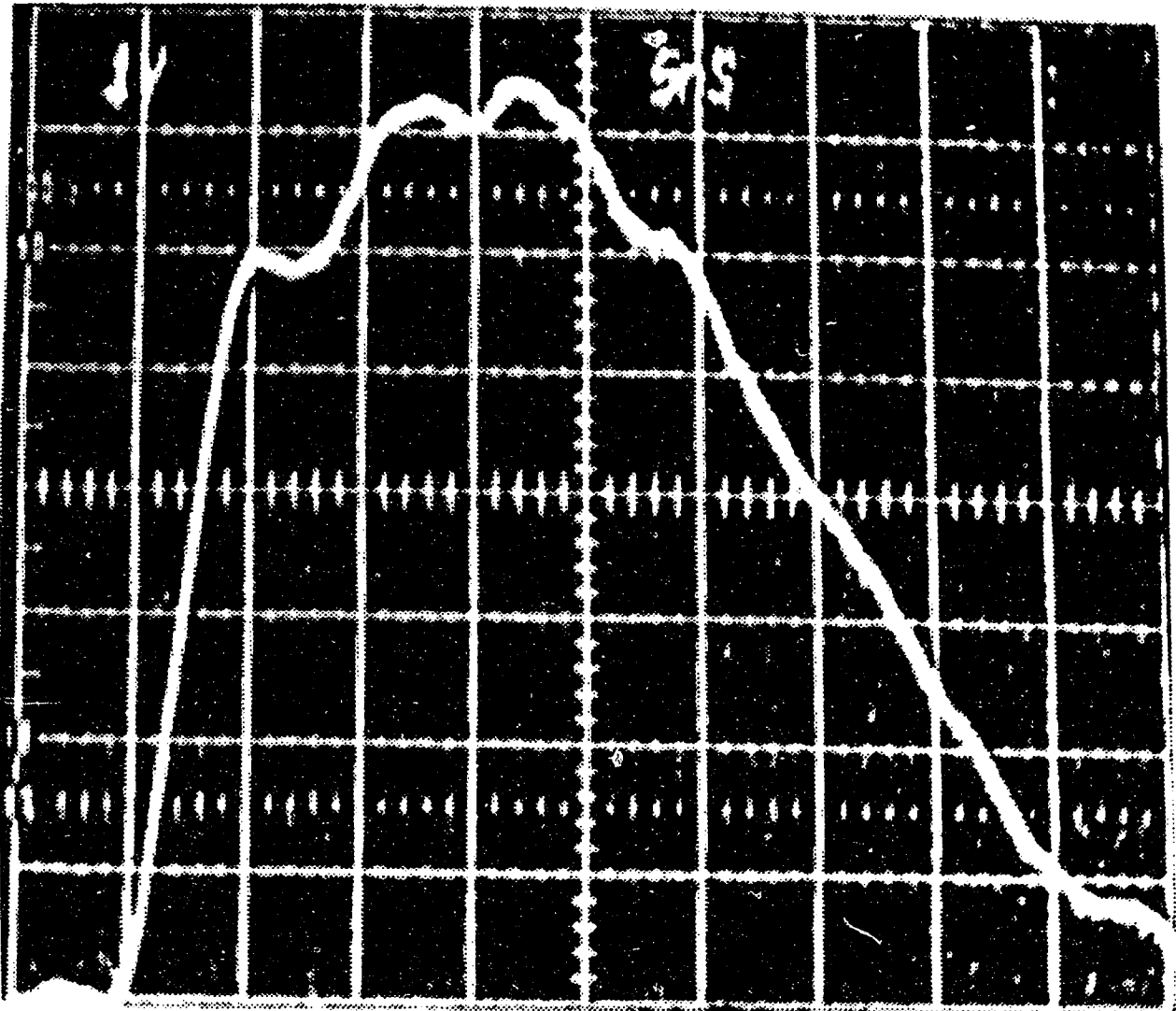


Fig. 5 High speed photodiode trace of XeCl laser pulse shape showing risetime of 5 ns and pulse length (FWHM) of 30 ns.

to stress-cracking under the influence of the fluorine gas. This constitutes a major difference between the gas chemistries of the two systems. Chlorinated plastics are acceptable for operation with HCl gas because they are only required to resist the corrosion effects of an acid gas. Chlorinated plastics are undesirable for use with F₂ gas because the more reactive fluorine substitutes itself for chlorine atoms. The PVC body on the main discharge side of the module was replaced with a fluorinated engineering plastic called Kynar (poly-vinylidene fluoride) which is the material used in many commercial excimer modules. The Kynar has provided relatively trouble free operation for over 2 years now. The PVC on the UV preionization side has not been replaced because it has not failed. However, its presence does reduce gas lifetime due to reaction with the F₂. In spite of the limited gas lifetime the KrF module operates well in terms of its ability to provide substantial amplification for the pulses from the dye laser systems. It has a discharge length of 53 cm and a cross section of approximately 32 mm by 14 mm. It is capable of producing over 600 mJ in a 30 ns pulse when operated as an oscillator with a plane-plane resonator.

KrF Laser Physics

Unlike many other types of lasers where the emission is the result of an electronic transition in an atom or a stable molecule, excimer lasers make use of the formation of unstable molecular species. The term excimer refers to a molecule which is created in an excited state. As soon as a photon is emitted or the energy lost to collisions the molecule becomes unstable and the constituent atoms become repulsive or are easily broken apart. The principal chemical reactions which result in the formation of excited KrF (KrF*) molecules are:



The harpoon reaction tends to be an early process in the course of the discharge and the ion - ion reaction tends to dominate once the discharge is fully developed. In the recombination reaction the M atom is the buffer gas which facilitates the reaction. The buffer gas affects the reaction rates by virtue of its mass when it participates in three-body processes⁴⁷. The word excimer is a bit of a misnomer for most of the laser systems to which it is applied. The term actually refers to a molecule which exists in an electronically excited state but which is formed from two identical atoms. The proper term is exciplex for systems such as the KrF* and XeCl* molecules. In spite of this, the common usage is to apply excimer to all such systems.

Figure 6 shows an energy level diagram⁴⁸ of the KrF excimer molecule. The transition of interest is the $B^2\Sigma_{1/2} - X^2\Sigma_{1/2}$ transition between the lowest stable upper state and the unstable lower state. It is important to note that within the upper state there exists a series of vibrational sublevels. These levels are important because their existence strongly affects the amplification characteristics of the KrF gain medium⁴⁹. The most important effect is that they produce a relatively wide gain bandwidth since the lower four vibrational bands overlap. Wide bandwidth is critical in the ability of a lasing system to amplify short pulses where the increase in bandwidth is a direct result of shortening the pulse. The bandwidth of the KrF transition is approximately 2.2 nm which is in principle capable of amplifying pulses as short⁵⁰ as 30 fs. To date the shortest pulses⁵⁰ amplified in KrF are 230 fs but pulses from KrF amplifiers have been compressed³⁹ after amplification to 60 fs. One major disadvantage of excimer systems is that the lifetime of the upper state is relatively short, being on the order of 3 - 5 nanoseconds for KrF. This means that energy pumped into the inversion cannot be stored for longer than this time. The result is that the energy available to a single short pulse is limited by the cross sectional area of the amplifier and the inherent saturation energy density (E_{SAT}) of the lasing medium. Once again the structure of the upper energy

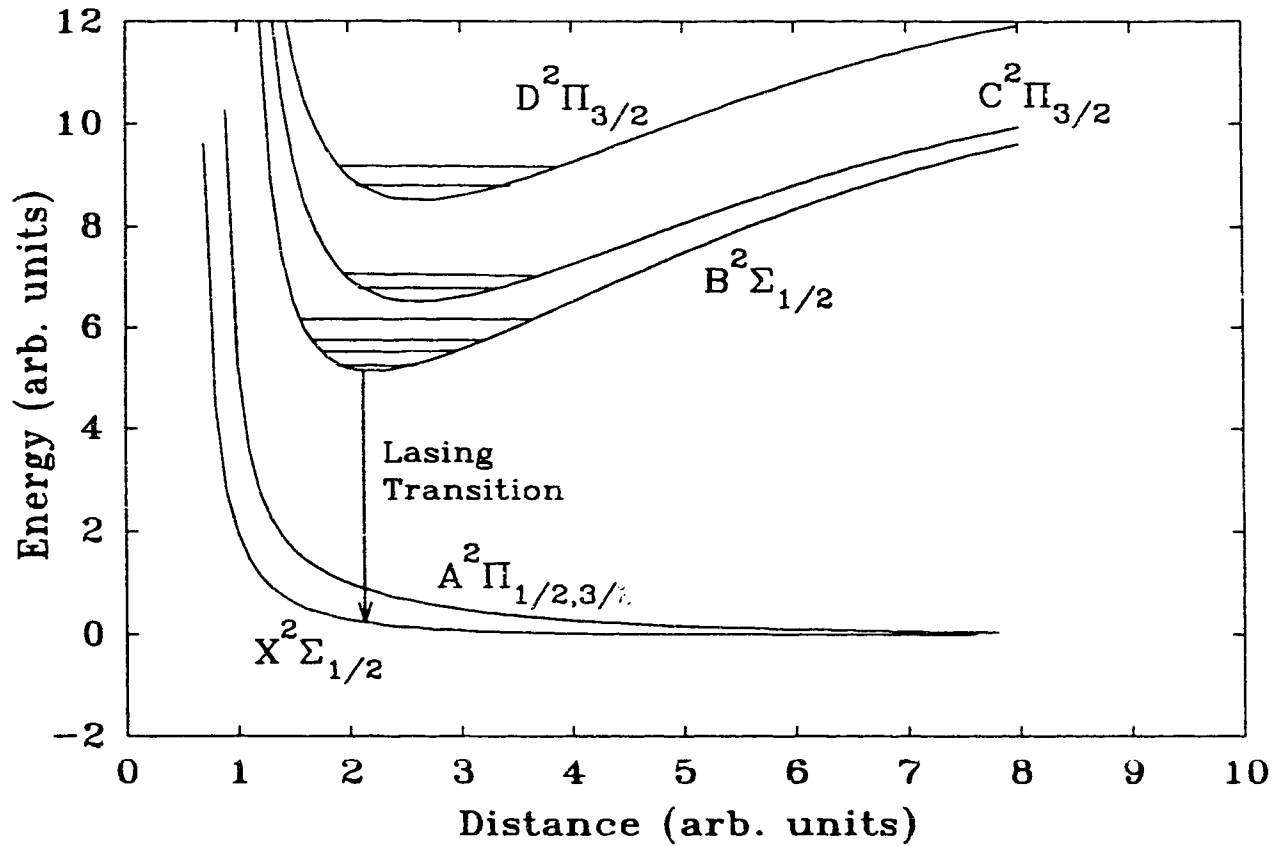


Fig. 6 Diagram of KrF excimer molecule energy levels as a function of atomic separation showing the B-X laser transition. The separation between the B and C levels is exaggerated to show part of the vibrational manifolds.

levels comes into play in determining the characteristics of the amplifier⁴⁹. There are two effects which act to modify the value of E_{SAT} in KrF dependent on the pulse length. Firstly, there is a certain amount of mixing between the B and C states which results in additional energy being available to amplify pulses on timescales longer than that over which the B - C mixing occurs. This process has been measured^{51,52} and is observed as a 10-25% gain recovery with a 54 ps time scale following the passage of a saturating pulse. Secondly, there is relaxation from the upper vibrational levels of the B state which proceeds on a slower timescale of hundreds of picoseconds. In the case of ultrashort pulses where the duration of the pulse becomes less than the time it takes to relax the upper vibrational states the saturation energy density becomes reduced in comparison to that which would be observed with longer pulses. Measurements⁵¹ of gain dynamics using subpicosecond pulses have shown that for pulses under 5 ps in duration the value of E_{SAT} is 2.0 mJ/cm^2 but for pulses between 5 and 200 ps the value of E_{SAT} is expected to increase to 2.7 mJ/cm^2 and remain constant for pulses over 200 ps. The final result is that while KrF lasers possess the characteristics necessary for amplifying ultrashort laser pulses the efficiency with which they are able to do so is reduced as the pulse length is reduced.

Dye Laser Systems

As mentioned previously the dye laser systems are modeled after systems developed by Szatmari and Schafer. Two complete dye laser systems were developed for this project in order to examine differences between 100 ps and 1 ps timescales in the generation of keV x-rays. The two systems are referred to by their nominal pulse length while the actual pulse lengths produced range from 120 ps to 90 ps for the "100 ps" system and were typically estimated to be 850 fs for the "1 ps" system. In addition, the 850 fs pulses could be "stretched" to 2 ps by use of a longer frequency doubling crystal. The dye lasers were constructed such that it is possible to switch operation between the

two merely by the removal or addition of two mirrors and little or no realignment of the system is required. The operational principles of the 100 ps system will be discussed first followed by those of the 1 ps system. A detailed discussion of setup procedures for the dye lasers is given in Appendix 1.

100 ps Dye Laser

The 100 ps system is shown schematically in Fig. 7 and consists of a quenched resonator dye laser (QR) which produces a short pulse with a relatively broad spectrum which is narrowed using a dielectric notch filter and amplified in two stages. Figure 8 shows the basic physical structure of the quenched resonator. The idea is to pump a gain region (dye cell) which has two competing resonators having different temporal evolutionary characteristics (one fast and one slow) and a slight angular separation. The first (inner) resonator is provided by the dye cell walls which have relatively small reflectivities (4%). This inner resonator is short (dye cell length) in comparison to the second (outer) resonator. However, the outer resonator has a much higher Q factor due to the use of a high reflectivity back mirror. The Q factor is proportional to the ratio of energy storage to energy loss per transit in the resonator. Figure 9 shows a computer simulation of the temporal evolution⁵³ of the intensity in the QR. The principle is that, initially, the gain builds up much more rapidly than the laser field in either resonator. After the gain reaches a high level (well beyond steady state) the field in the inner resonator starts to build up very rapidly due to the short length of the inner cavity. The reflectivity of the dye cell walls is small but provides sufficient feedback to initiate strong lasing once the gain reaches a high enough level. This results in a laser spike (relaxation spike) which, in the absence of the outer resonator, would normally be followed by a modulated buildup to steady state lasing. However, the presence of the high Q outer resonator results in a second laser field building up which rapidly dominates the gain and

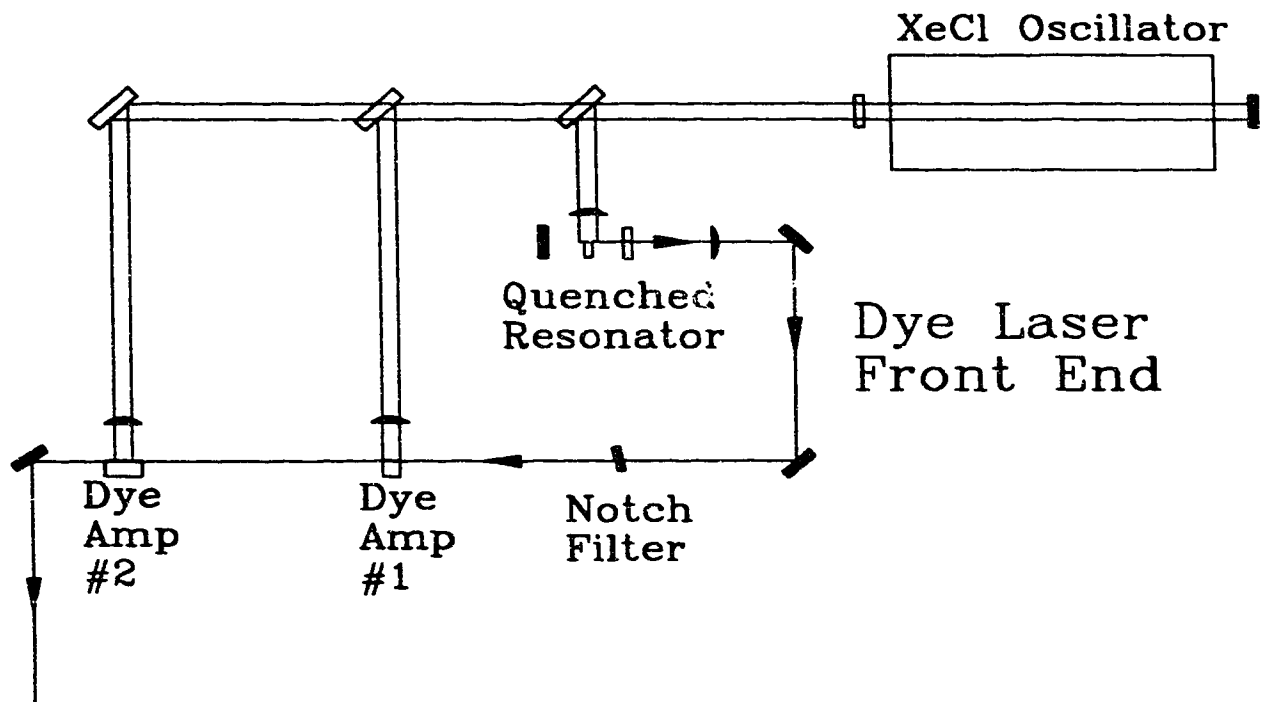


Fig. 7 Diagram of 100 ps dye laser system.

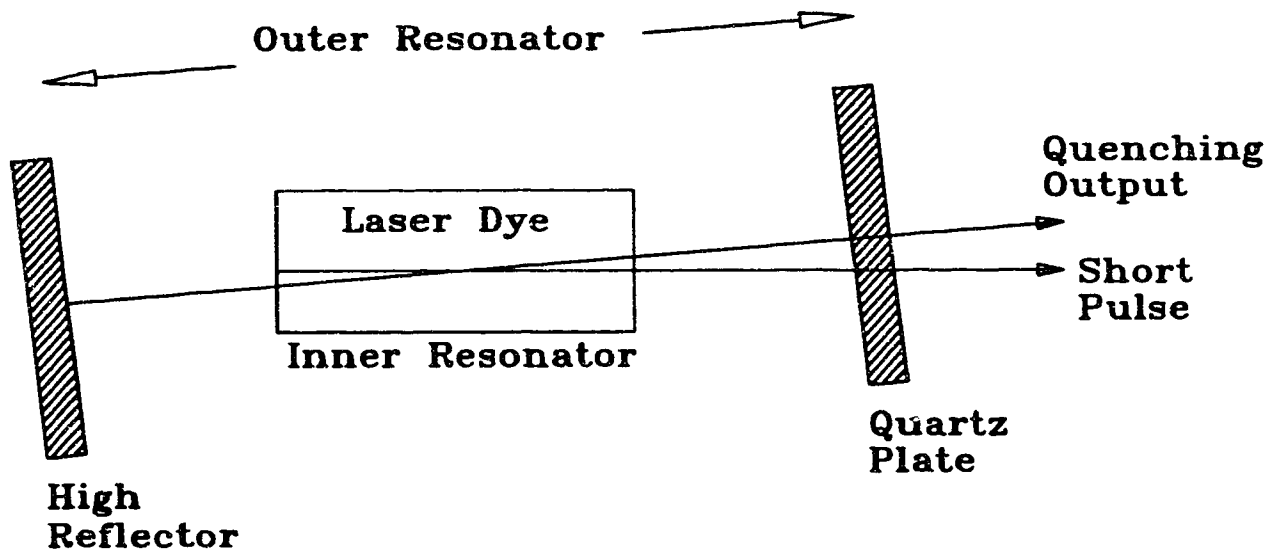


Fig. 8 Schematic diagram showing physical structure of quenched resonator (QR).

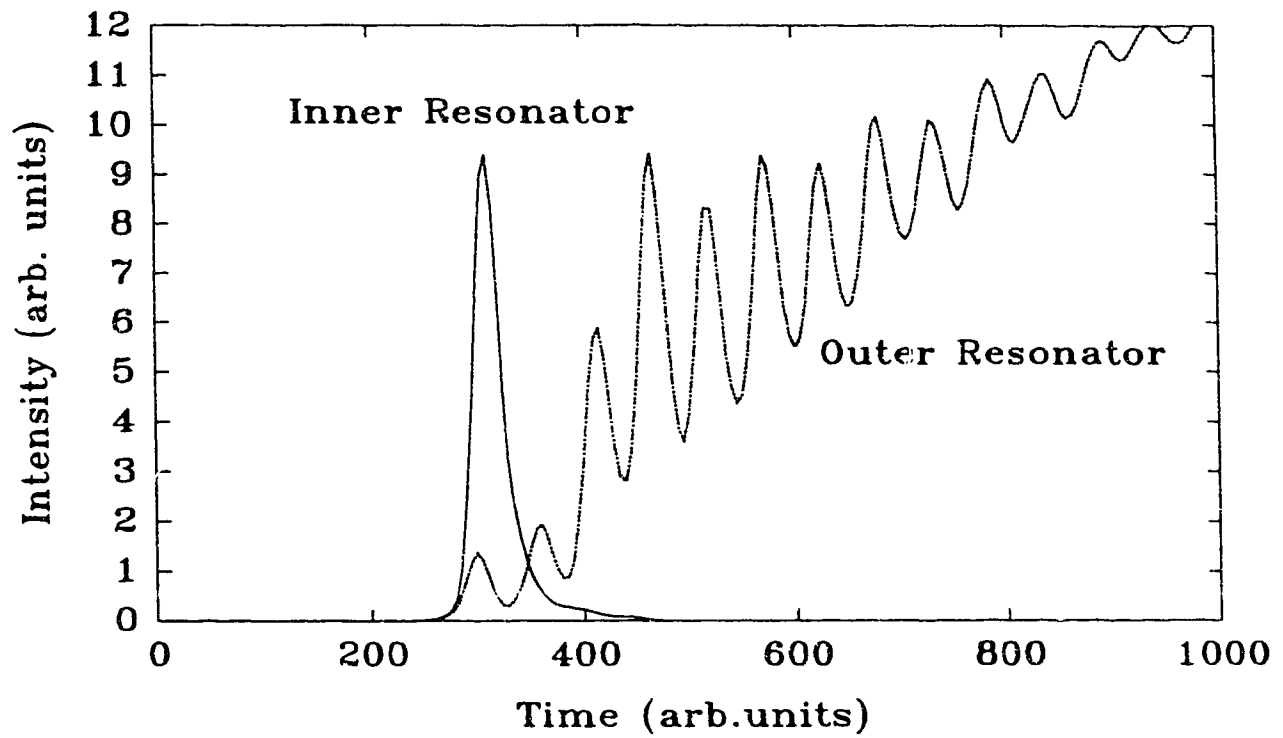


Fig. 9 Computer simulation of quenched resonator temporal evolution. Inner resonator produces single relaxation spike and bulk of pump energy is shunted to outer resonator.

"quenches" the inner resonator. The result is that the initial spike escapes from the inner resonator and the remainder of the pump pulse energy is diverted through the outer resonator. The most important parameters in the process which determine the output pulse length are the pump pulse risetime and the length of the dye cell. Additional parameters are the absorption and emission cross sections of the dye molecules.

The actual setup of the system uses a 5 mm quartz dye cell as the inner resonator. The outer resonator is formed with a high reflectivity mirror and a quartz plate approximately 10 cm apart and symmetric around the dye cell. The quenched resonator was filled with a 10^{-2} Molar solution of Coumarin 500 dye where the solvent was a 1:1 mixture of p-dioxane and ethanol. Mixing of solvents is highly advantageous because it allows a tuning of the central peak of the dye laser output over an experimentally measured range of almost 30 nm. The quenched resonator is pumped with approximately 10 mJ of XeCl energy and produces 1.5 μ J of light in a 90 ps pulse (streak camera trace shown in Fig. 10) with a broad modulated spectrum (10 nm) as shown in Fig. 11. The modulation of the spectrum is a result of a weak Fabry Perot etalon effect from the surfaces of the dye cell which is strongly enhanced by the gain. It is necessary to filter the broad spectrum in order to select only the portion near 497 nm for frequency doubling into the gain band of KrF at 248.5 nm. The method used to achieve this filtering has taken two forms over the progress of the project. Initially, the method used was the same as Szatmari's system which used a diffraction grating to select the desired frequency. There were two problems associated with this method of filtering. The first is that it is inefficient in terms of using the energy produced in the quenched resonator. The bulk of the energy incident on the grating goes into the zero'th order reflection which is not dispersed and cannot be used. The remaining fraction (~25% of the unpolarized QR beam) is dispersed. In addition there is a ratio of 3.7:1 in polarization leaving ~18% of the original energy in the dispersed beam. This beam must still be filtered further (using a suitable slit) in order to actually select the desired wavelength. The measured

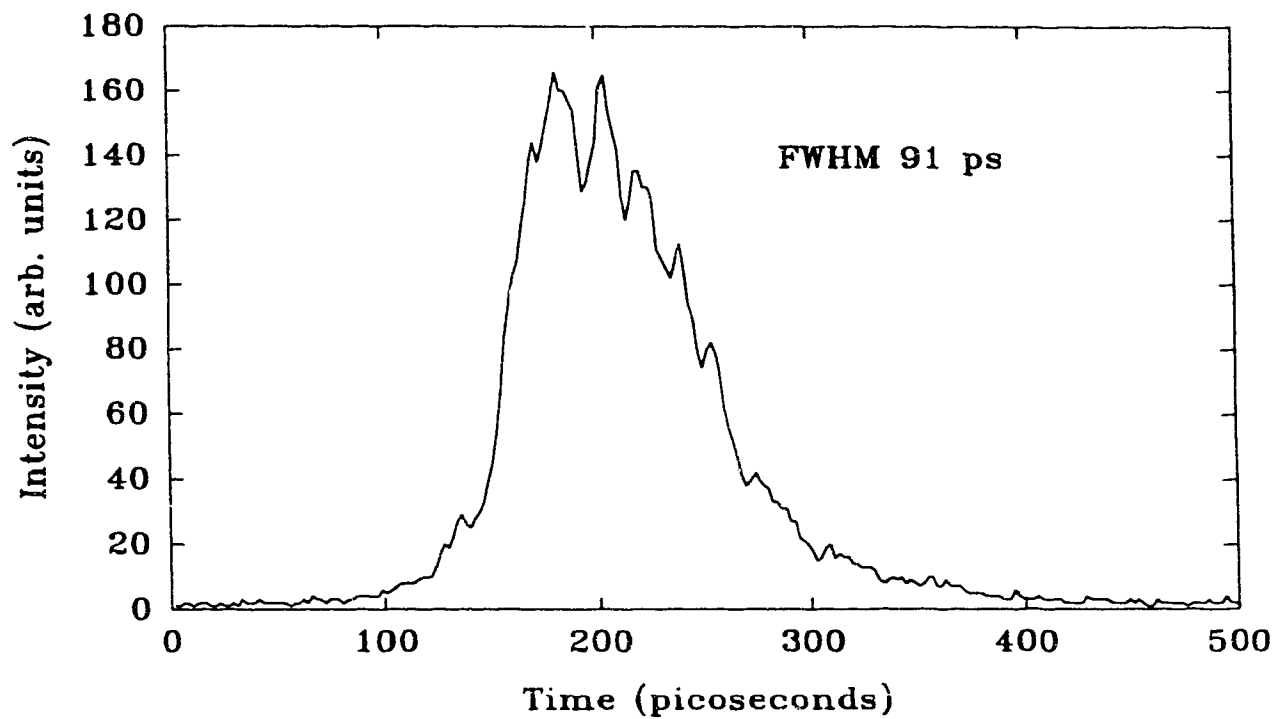


Fig. 10 Typical streak camera picture of Coumarin 500 quenched resonator pulse shape with FWHM of 91 ps.

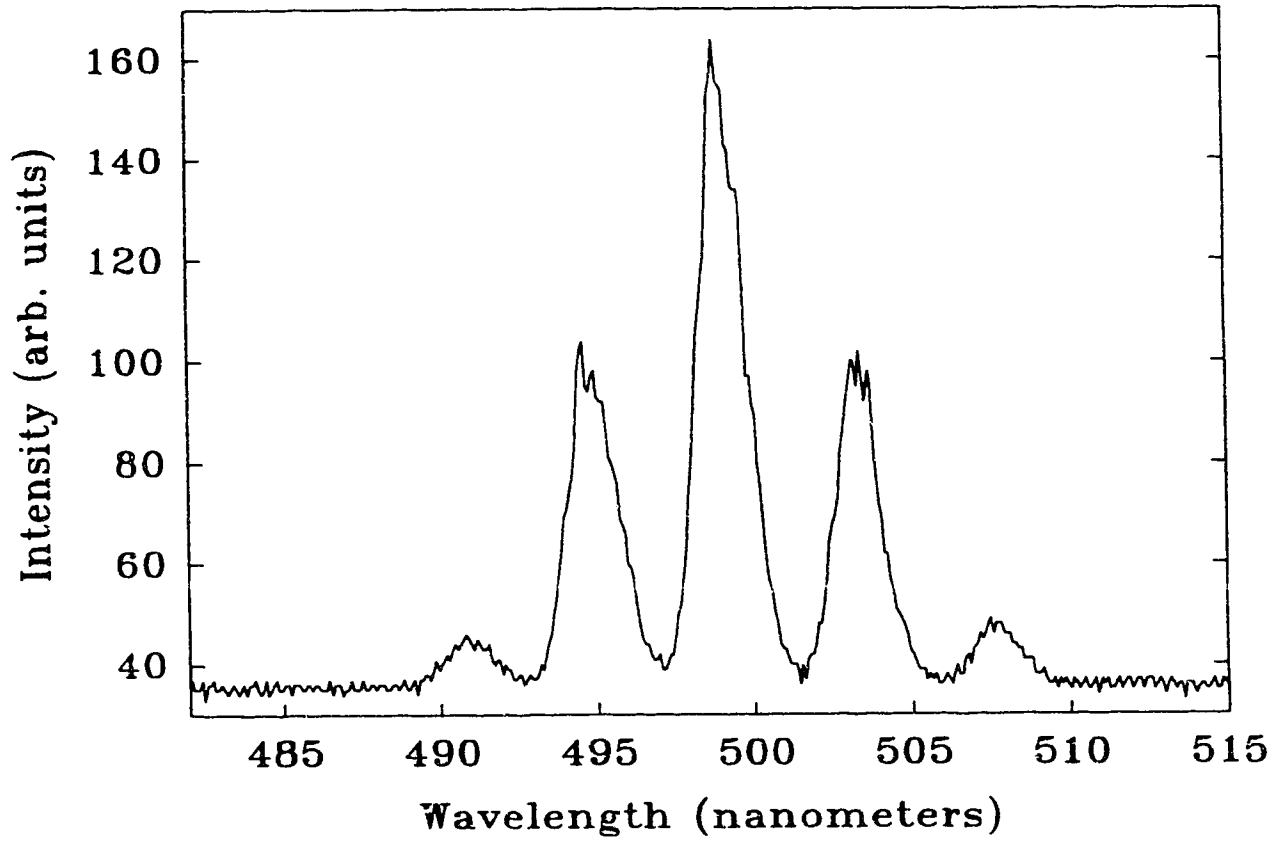


Fig. 11 Modulated spectral structure of quenched resonator.

loss ratio for this method was 560:1 and reduced the available energy to 2 - 3 nJ. It became evident that there was a need to replace the grating with a more efficient frequency selection system in terms of using the energy available from the quenched resonator. The new technique is to narrow the spectrum with a custom made dielectric notch filter with a bandwidth of 1 nm which is used to select the portion of the output from the quenched resonator near 497 nm. The measured rejection ratio with this method is 80:1. This method of filtering also solved the second problem associated with the grating. The slightest change in grating tuning always necessitated a complete realignment of the dye system because of the physical shift of the grating itself. The use of a transmission element eliminated this problem completely since the physical shift due to angle tuning a transmission element over a few degrees is negligible. With the improvement in the filtering system the frequency narrowed energy is almost 20 nJ. This is increased by the use of the two amplifier cells which raise the pulse energy to 1.5 μJ and then to 30 μJ respectively.

1 ps Dye Laser

The principle behind the 1 ps system is to generate a series of resonator transients which results in a cascade of pulse shortening with successively shorter pulses based on the risetime of each preceding pulse. The dye laser system is shown schematically in Fig. 12. The laser system starts with a quenched resonator (similar to the 100 ps system) which is followed by a short cavity dye laser (SCDL) and then by a distributed feedback dye laser (DFDL). The cascade of photon wavelengths is from the 308 nm pump pulse of the XeCl to 340 nm in the QR to 365 nm in the SCDL and finally to 497 nm in the DFDL. The quenched resonator is a 5 mm dye cell filled with para-terphenyl (PTP) dye which lases at 340 nm. The output from this QR is typically 2 μJ of energy with a pulse width of 200 ps. Figure 13 shows a streak camera trace of the QR pulse. The 200 ps pulse length contrasts with the 100 ps system in spite of the fact that the physical

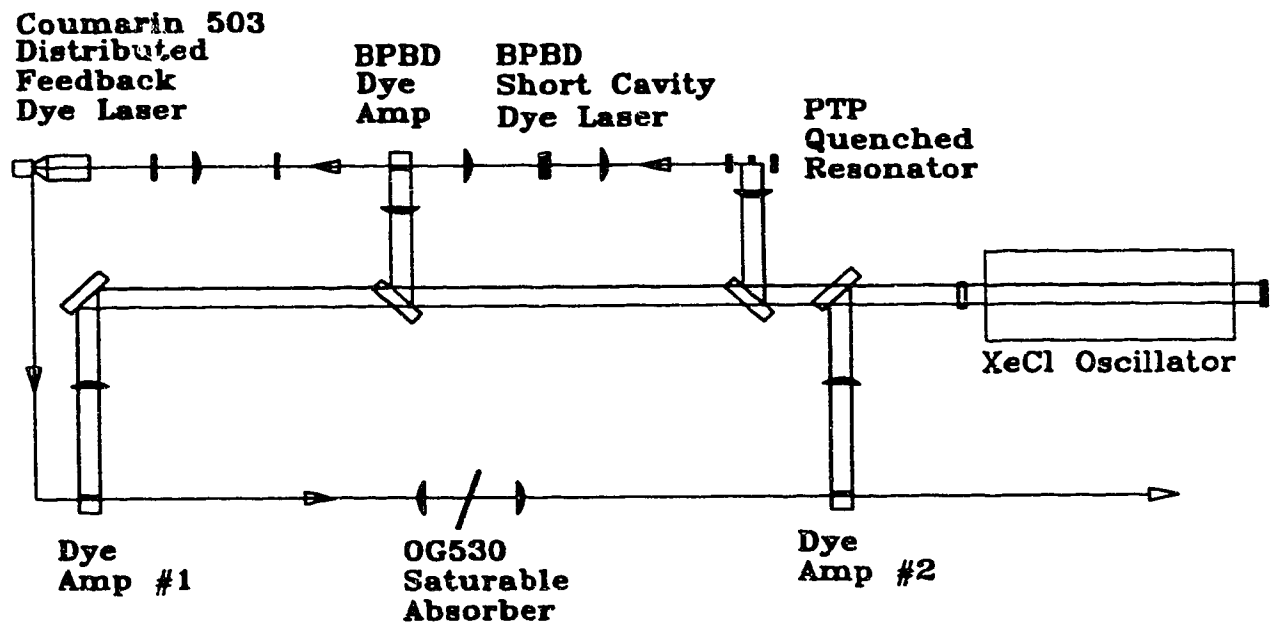


Fig. 12 Diagram of 1 ps dye laser system.

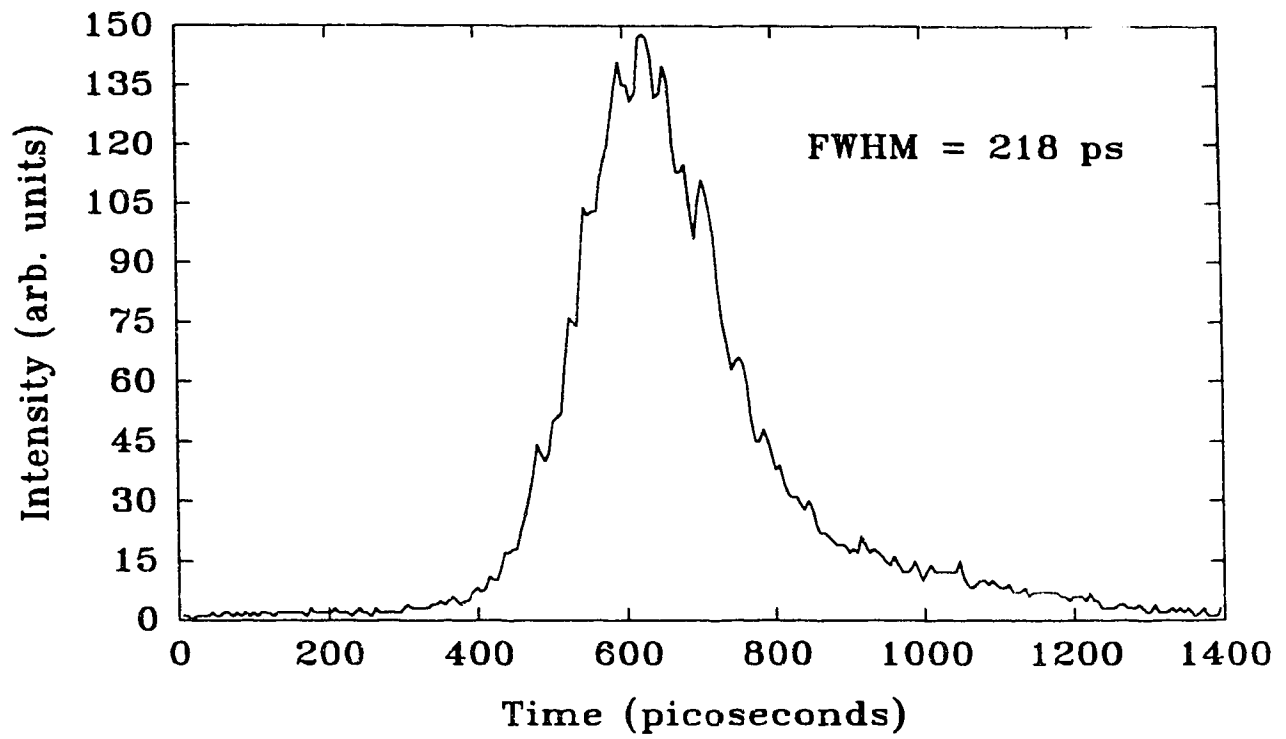


Fig. 13 Streak camera picture of PTP quenched resonator output.

parameters are the basically the same as in the 100 ps system. This demonstrates that the parameters of the dye itself (absorption and emission cross sections) also play a role in determining the pulse length. The second stage of the short pulse system is the SCDL which is made from two mirrors sandwiched with a 0.5 mm gap in between which is filled with 10^{-2} Molar solution of 2-(4-biphenyl)-5-(4-t-butylphenyl)-1,3,4-oxadiazol (BPBD) dye which lases at 365 nm. The very short gap between the resonator mirrors provides for a very rapid rise in the optical field when the dye is excited. The SCDL has a dichroic back mirror (through which the pulse from the QR is focused) with high transmission at the pump wavelength of 340 nm and high reflectivity at the lasing wavelength of 365 nm. The front mirror has 50% reflectivity at both wavelengths. The output from the QR is injected into the SCDL cavity through the dichroic and the result is a very strong relaxation spike followed by a low level steady state output. Typically the output from the SCDL had 200 nJ of energy in a 60 ps pulse. The output pulse shape is shown in Fig. 14. The output from the SCDL is amplified to an energy of 15 μ J in a 1 cm amplifier filled with a 5×10^{-4} Molar solution of BPBD.

In the original design³⁸ the output from the SCDL amplifier would be sent through a stage called a gated saturable absorber (GSA) which is formed from two dichroic mirrors with a 0.5 mm gap filled with 2,5-di-(5-tert-butyl-2-benzoxazolyl)-thiophene (BBOT). The dichroic mirrors are designed to have high transmission at 365 nm and high reflectivity at 400 nm which is the lasing wavelength of BBOT. Again the operation relies on the transient lag between the buildup of the gain and the optical field. When the amplified pulse from the SCDL hits the GSA the front edge is absorbed in the dye and the dye then becomes relatively transparent to the SCDL pulse as the dye molecules are shifted to their upper states. However, due to the high reflectivity of the mirrors at the BBOT wavelength, lasing builds up a very short time later and the transparency is shut off again as the population in the excited state is reduced to a much lower steady state value. Thus the tail on the SCDL is eliminated as the energy is

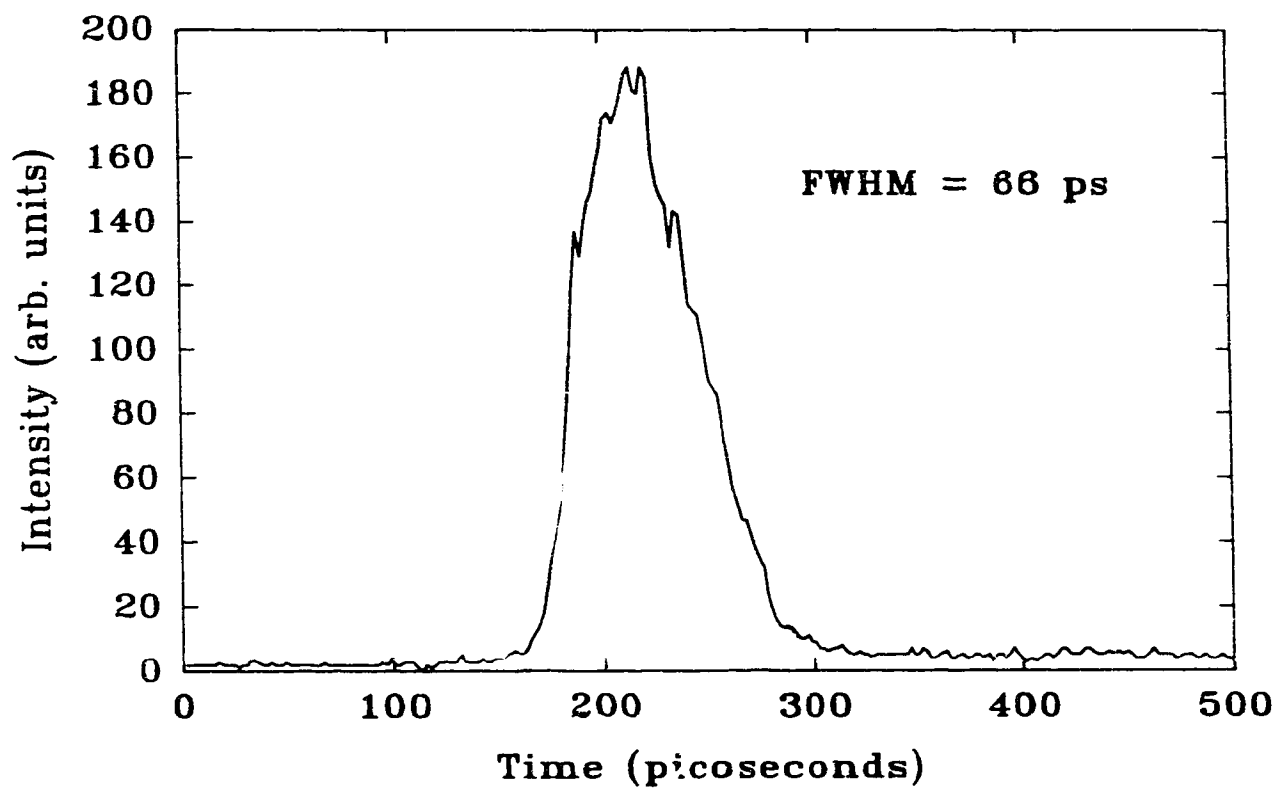


Fig. 14 Streak camera picture of BPBD short cavity dye laser.

shunted into lasing of the BBOT. The result is a clean short pulse which is amplified again and then fed into the next stage which is the DF DL. Unfortunately, due to space restrictions on the optical tables it was not possible to implement the GSA stage and it was necessary to use the amplified SCDL pulse directly to pump the DF DL. Once the operation of the DF DL is explained it will become clear that this is not a major problem.

The operation of DF DL lasers is fundamentally different from most other types of lasers⁵⁴ in that there are no external feedback mechanisms employed to provide buildup of the optical field. Instead, the feedback is provided by creating a region of spatially modulated gain in which Bragg reflection occurs allowing the laser field to build up within the gain region. Figure 15 shows how the interference pattern between the two pump beams forms the modulated gain. The period of the modulation (Λ) is determined by the interference angle (2α) between the two pump pulses:

$$\Lambda = \frac{\lambda_p}{2n \sin \alpha} \quad (9)$$

where λ_p is the wavelength of the pump beams and n is index of refraction of the medium. In turn the wavelength (λ_L) at which the DF DL operates is determined by the period of the spatial modulation of the gain:

$$\lambda_L = 2n\Lambda \quad (10)$$

The subtle beauty of the system is that the rise of the optical field depletes much of the spatially modulated population inversion and results in the destruction of the laser cavity in the process of producing a pulse. This process will repeat if the pump pulse is sufficiently intense or long but if the pump pulse intensity is chosen such that the lasing threshold is reached only once then a single pulse can be produced. Figure 16 shows the computer simulated⁵⁴ behaviour of a DF DL when pumped well over threshold. Note that the first pulse is the largest because there is no loss of gain to ASE in the grating. The second pulse is smaller than the first in spite of the fact that the pump pulse is still rising because the gain is not completely reduced by the pulse generation process.

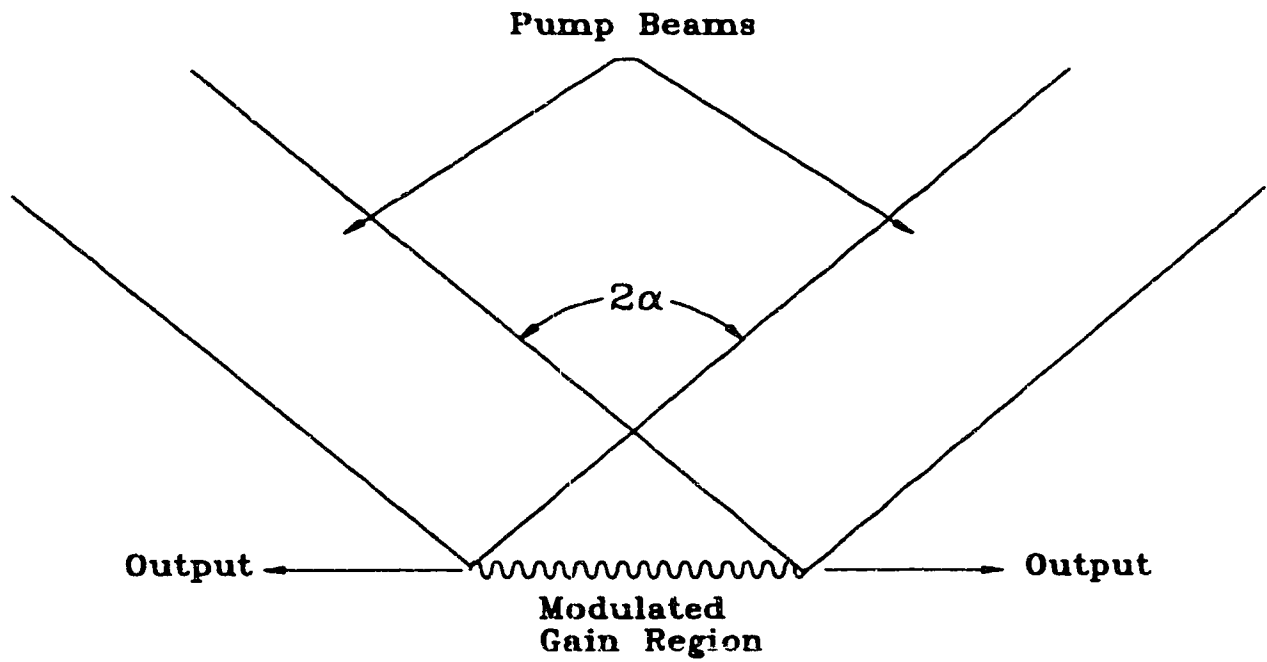


Fig. 15 Schematic diagram of modulated gain structure formation in DFDB by interference of pump beams.

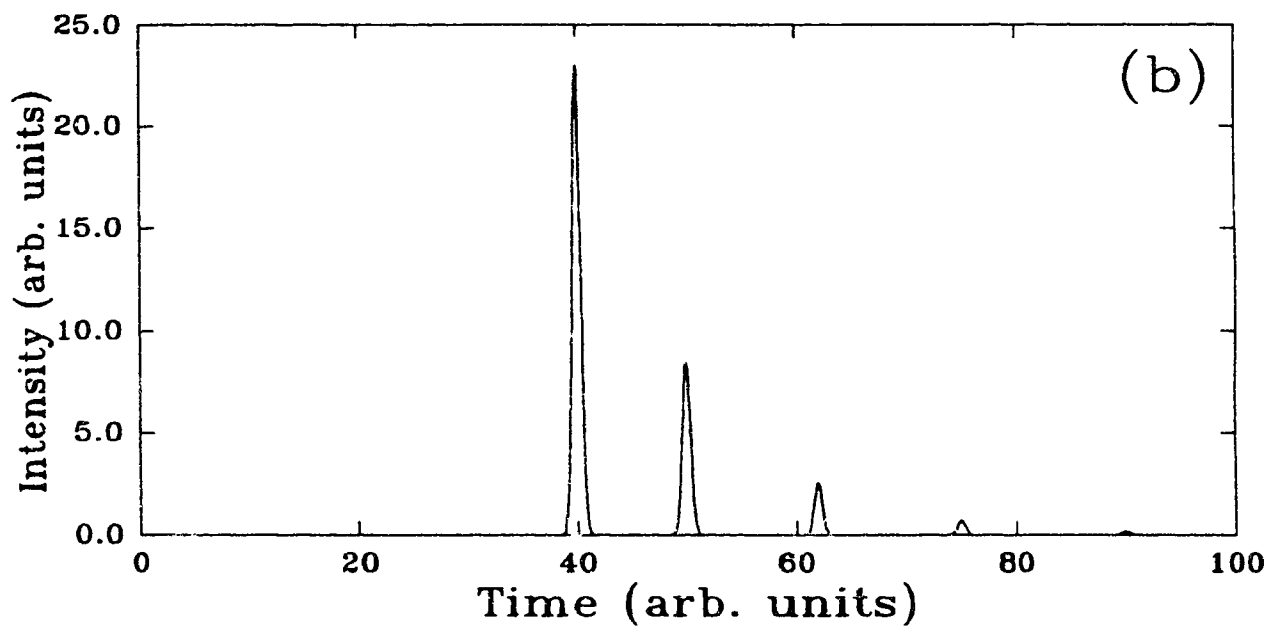
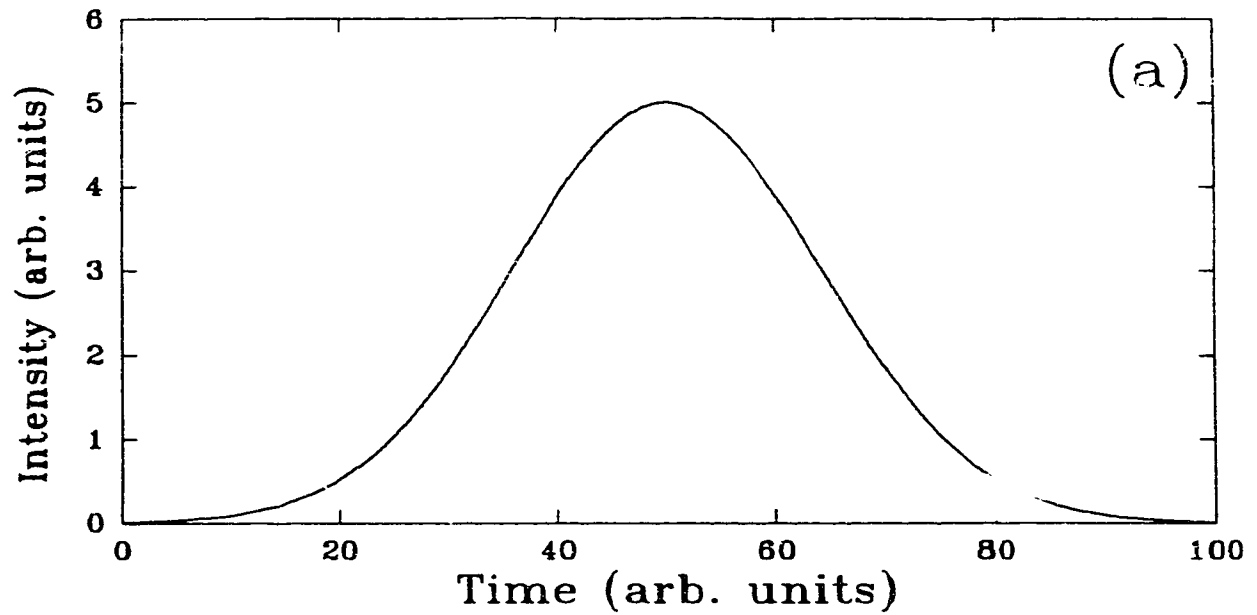


Fig. 16 Simulation of DFDL behaviour when pumped over threshold such that multiple pulses are produced. (a) Shows DFDL pump pulse. (b) Shows pulses generated by DFDL.

After the first pulse there is still a remnant of the grating and this produces a low level of continuous ASE which drains some of the gain in the interpulse period. Physical details of the implementation of the DF DL are shown in Fig. 17. The amplified pulse from the SCDL is expanded horizontally using a negative 19 mm cylindrical lens and then refocused by a positive 117 mm cylindrical lens at the front focal plane of a microscope objective (Leitz-Wetzlar 63/1.30). It is necessary to use a high numerical aperture objective (NA=1.30) because the angle at which the 365 nm beams must recombine is approximately 94°. Such numerical apertures are only possible with oil contacted objectives. A metal grating pattern (50 lines/mm) is placed near the image position of the objective to generate a diffraction pattern from the SCDL pulse. The zero'th order beam is blocked and the first order diffracted beams are reimaged by the objective inside a dye cell with a wall thickness of 150 μm filled with a 10^{-1} Molar solution of Coumarin 307 in dimethylformamide (DMF). Essentially what occurs is a demagnified reimaging of the metal diffraction grating inside the dye. The use of the first order beams allows the output wavelength of the DF DL to be tuned as the angle of the recombining beams is varied by moving the metal grating back and forth. This tunability is the principal trademark of DF DL operation. Measurements of the tuning range for this system yielded 20 nm tuning corresponding to approximately 6 mm of movement by the grating. Assuming the index of refraction of DMF to be 1.5 and the interference angle to be near 94 degrees the grating period is estimated to be approximately 166 nm. The measured output energy was typically around 2 nJ.

The temporal characteristics of the DF DL are more difficult to characterize. The measurement of pulse length of ultrashort pulses is an important scientific field in itself and many techniques have been developed for measuring pulse length using nonlinear photon processes⁵⁵. No direct measurements of the pulse length of the DF DL pulse were made because of the complexities involved in developing the needed measurement systems. In this system the output from the DF DL is an intermediate result. In the

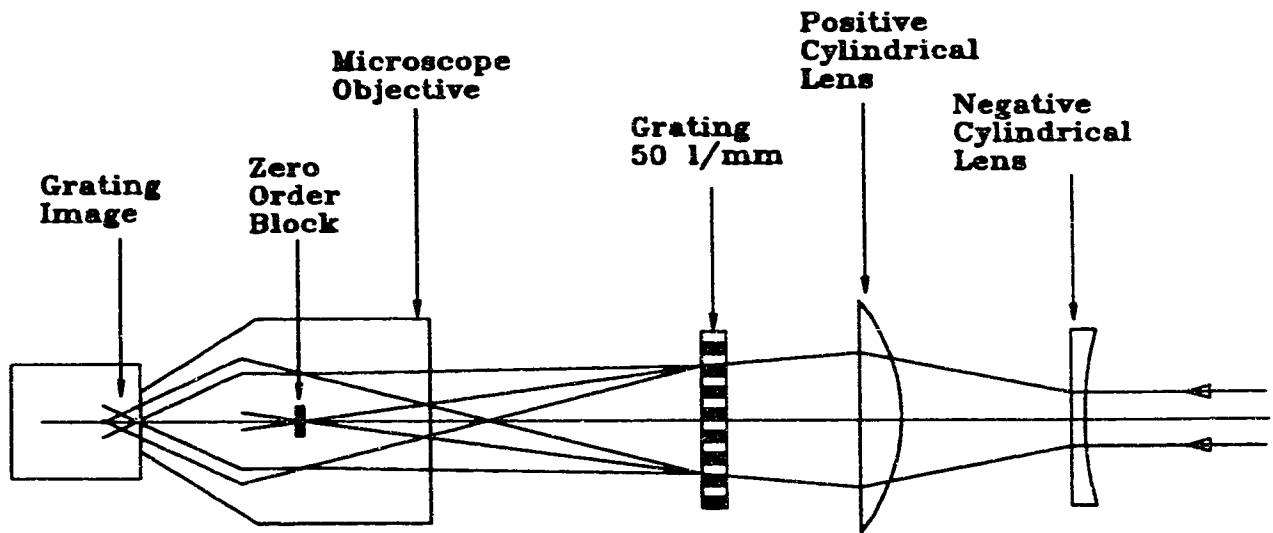


Fig. 17 Diagram of physical structure of DFDL apparatus.

visible spectrum our primary diagnostic is still the streak camera but the resolution is limited to 10 ps and can give no information below this level. Figure 18 shows a typical resolution limited streak trace which results from the DF DL pulse. Once the resolution limited range of operation has been achieved with the DF DL the measurement of the real pulsewidth is done using the final UV pulse of the laser system. The measurements that have been made in the UV range, using techniques which will be discussed later, indicate a pulsewidth of 800 - 900 fs.

The DF DL stage is followed by two 2 cm amplifier cells separated by a saturable absorber. The saturable absorber consists of two short focal length (25 mm and 30 mm) lenses with a 1 mm thick piece of Schott OG530 filter glass between the two lenses. This stage serves several important purposes. First, it isolates the two amplifiers from each other and prevents parasitic lasing from the strong gain which exists. Second, it serves as a collimator for the beam emerging from the first amplifier stage. This is necessary because the DF DL pulse must be focused somewhat beyond the first amplifier in order to get substantial gain in a strongly pumped dye cell. Third, it introduces some spectral broadening⁵⁶ and chirping (time dependent spectral structure) which is needed for additional pulse compression using gratings or prisms. Development of the pulse compression system is not part of this project. The first dye amplification stage is filled with a 5×10^{-3} Molar solution of Coumarin 500 and increases the pulse energy to 1.6 μ J. Passage through the OG530 filter reduces this energy to 70 nJ and the second dye amplifier which is filled with 2.5×10^{-3} Molar solution of Coumarin 500 raises the energy back up to 20 μ J. Note that transmission through the OG530 is kept low (4%) in order to suppress lasing between the dye amplifiers due to their close physical proximity. OG530 transmissions as high as 50% have been measured with this system and if the dye amplifiers could be further separated spatially then the system would be able to amplify the pulses more efficiently.

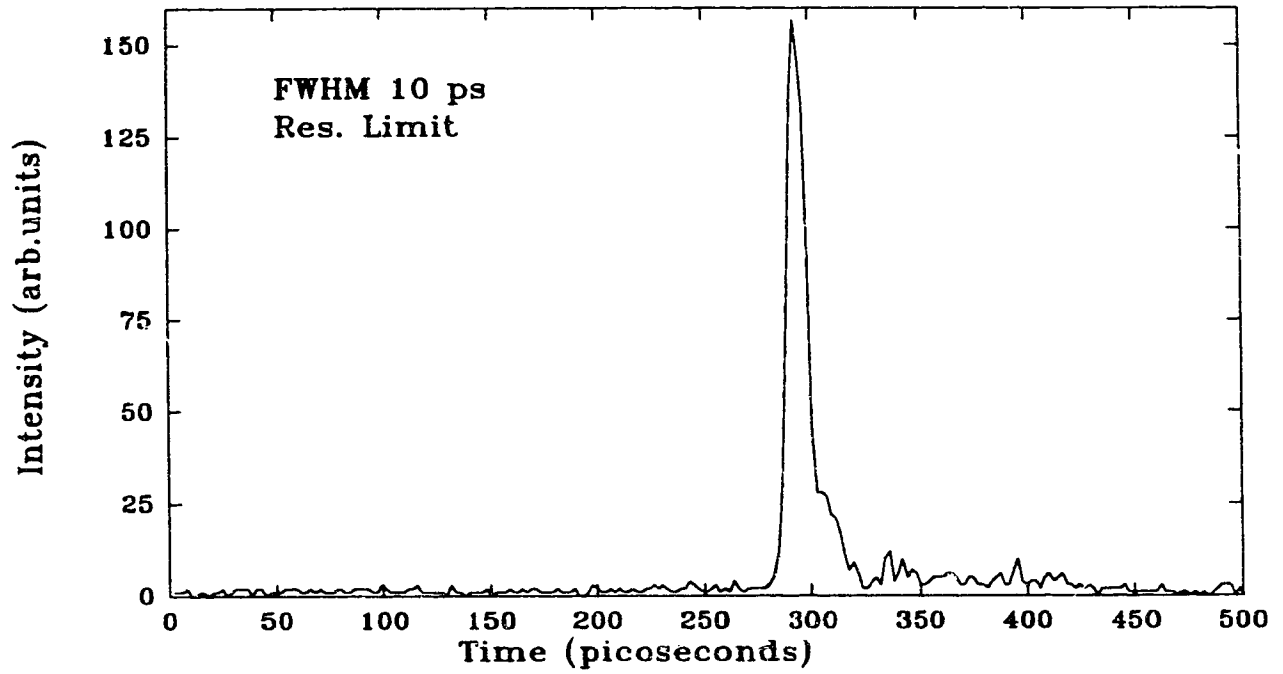


Fig. 18 Streak camera picture of amplified DFDL laser pulse showing resolution limited pulse length.

Frequency Doubling and KrF Amplification

The pulses which emerge from the two dye laser systems are fed into a set of switching mirrors which allow the user to choose between the two pulse lengths by removing or replacing only two mirrors (one for the dye beam and one for the pump beam). In principle, after the switch point the dye laser beams are collinear and the remainder of the system should require no adjustment. In practice there is always some beam wandering due to thermal drift in the laser bay which results in the need for periodic adjustment to the dye beam steering. It is possible (with experience) to keep both systems operational in parallel for a period of several months without major difficulty.

After the switching mirrors the dye pulse is focused by a 1000 mm glass lens into a frequency doubling crystal. Two types of nonlinear crystals have been used during this project. During the early stages of the work the crystal was a positive uniaxial urea crystal 8 mm in length. A negative uniaxial beta barium borate (BBO) crystal was later purchased for the development of the 1 ps pulse system. However, it was used for both systems because both beam quality and conversion efficiency improved for the 100 ps system in spite of the relatively short length (0.5 mm) of the crystal. The use of the BBO crystal has increased the reliability of the frequency doubling substantially in comparison to the urea crystal because of an increase in optical quality. The urea crystal had a slightly cloudy appearance and produced a heavily structured output beam. In addition to the 0.5 mm BBO crystal an 8 mm BBO crystal was borrowed from another laboratory and used to "stretch" the short pulses and access slightly longer pulselength regimes. This is possible because of the difference in group velocities at the fundamental and the 2ω wavelengths. In BBO the UV pulse is slower than the green pulse and in a thick crystal the effect is to create a stretched UV pulse as the UV continually lags behind the fundamental. In practice the stretching to approximately 2 ps was not as much as was

expected theoretically (6 ps) possibly due to recompression by gain saturation in the KrF amplifier.

Typically, the 0.5 mm BBO crystal provided 5% conversion efficiency and the output energy at 248 nm was 1 - 2 μJ . This energy is injected into the KrF module and amplified in two passes. During the first pass the beam expands from less than 1 mm diameter to about 5 mm diameter and increases to 1 - 2 mJ in energy. The pulse is focused by a 100 mm lens into an evacuated spatial filter with a typical diameter of 30 μm . The spatial filter is made from glass tubing which is collapsed at one end using a blowtorch and ground down to expose a hole of the desired diameter. After the spatial filter the beam is allowed to expand and is recollimated using a 500 mm lens. This generally results in an overfilling of the amplifier but this helps to compensate for beam wandering and thus provides some stability. The collimated beam is fed through the amplifier and energy is increased to a typical value of 60 to 65 mJ in the case of the 100 ps pulse (this includes 5% ASE). In the case of the 1 ps pulse the typical energy was lower at 50 - 55 mJ including ASE. This difference corresponds to the difference in E_{SAT} values between the two pulse regimes. A rough estimate of the small signal gain in the module for the 100 ps pulse yields a range of 0.12 - 0.15 cm^{-1} .

Beam Divergence

The divergence of the laser beam determines its ability to be focused by a lens onto a target where the plasma is created. Measurements of the divergence of the KrF beam were made using a 10 m lens to generate burns on Dylux UV sensitive paper. A UV sensitive camera was also used to image the focal spot generated by the 10 m lens. Typically the divergence of the main pulse from the laser system was measured to be 60 μrad . The divergence of the ASE which accompanies the main pulse depends largely on the size of the pinhole in the vacuum spatial filter. In principle, the ASE on target should be a reimaging of the ASE passing through the pinhole. Generally the pinhole started at

30 μ m diameter but the damage due to ASE focused onto the pinhole resulted in an enlargement with time. After several thousand shots the pinhole size would typically be increased to 80 μ m by 100 μ m. The divergence of the ASE was also measured using the video camera as well as Dylux paper and ranged from 150 μ rad to 250 μ rad. For calculating ASE intensity a typical value of 200 μ rad is used.

Nonlinear Optics and Pulse Length Measurement

It is possible that self-focusing in the quartz of the triplet lens could have an effect on the focusing of the pulses from the 1 ps system. Some self-focusing of the unfocused 850 fs beam was observed as an intensification of beam structure after passage through a 2 cm piece of quartz. Self-focusing is an effect arising from nonlinear indices of refraction. The index of refraction in a nonlinear regime can be expressed as:

$$n = n_0 + \gamma I \quad (11)$$

Where n_0 is the linear index of refraction, γ is the second order index as a coefficient of laser intensity (I). In ultrashort pulse systems it is important that the cumulative effects of the second order index be minimized in order to avoid beam breakup due to self-focusing in the laser system. The criteria used is the so called "B integral":

$$B = k_0 \int \gamma I(x) dx \quad (12)$$

where k_0 is the wave number of the laser ($2\pi n_0/\lambda$) and x is path length in the medium.

The importance of self-focusing can be roughly estimated by ignoring any spatial dependence in the form $k_0\gamma IL$. The typical value of I for the final 850 fs pulse is estimated as 5-6 GWcm^{-2} and the value⁵⁷ of γ for quartz is $2.59 \times 10^{-16} \text{ cm}^2\text{W}^{-1}$ and $L=$ 2 cm of quartz. This results in a B integral value of ~ 1 which is borderline for inducing breakup due to self-focusing ($B > 3$ is considered unacceptable). The effects of self-focusing were tested experimentally using a 2 cm thick quartz window. The short pulse was transmitted through the window and burns on Dylux were taken at various distances

beyond the window. The burns at the window exit showed only very minor changes in appearance while burns at a distance of 260 cm showed some enhancement of intensity modulations originating from the structure of the KrF discharge. A similar experiment was conducted when the beam divergence was measured using a 10 m lens. In this case no change in the structure or the size of the focused beam was observed when the 2 cm window was inserted into the unfocused beam. However, in both cases the focused beam did contain considerably more structure than was seen at the longer pulse lengths perhaps due to self-focusing in air. On this basis it may be said that self-focusing must be considered as a possible source of focal degradation in the case of the 850 fs pulse but that the experimental evidence is inconclusive.

For the measurement of the 100 ps pulse the 10 ps resolution of the streak camera is adequate. However, in order to measure the duration of the short pulse it was necessary to use nonlinear optical processes as a means of estimating pulse length. The primary method used for obtaining approximate values of pulse length during the experiments was two-photon absorption in quartz. By measuring the transmission of the unfocused pulse in a 20 mm thick quartz plate one can obtain estimates of the pulse length by assuming a pulse shape. The assumption of pulse shape is not based on any physical parameters and thus yields an inferred estimate rather than a direct measurement of pulse length. The transmission of the unfocused short pulse is typically measured to be around 70% for a pulse with an incident energy density of 5 - 6 mJ cm⁻². The two-photon absorption coefficient of quartz (β) is 4.5×10^{-11} cm W⁻¹. Assuming a gaussian pulse shape the energy transmission (T_E) of a pulse through a quartz plate may be calculated to be:

$$T_E = \frac{(1-R)^2}{\sqrt{\pi}} \int_{-\infty}^{+\infty} \frac{dx}{\exp(x^2) + \gamma} \quad (13)$$

where $\gamma = \beta L(1-R)I_0$ and $I_0 = \frac{E}{A\tau\sqrt{\pi}}$ (14)

R is the reflectivity at a single surface, L is the thickness of the quartz plate, E/A is the energy per unit area of the incident pulse and τ is the gaussian parameter of the pulse length. This method resulted in estimates of 800 - 900 fs for pulse length. The principal source of error in these estimates is the assumption of the pulshape. For instance, using a sech^2 pulse reduces the estimate by $\sim 15\%$ but the use of a triangular pulse increases the estimate by only $\sim 1\%$. Self-focusing of the beam in the quartz window is not expected to bias these measurements because of the distance required to observe any self-focusing effect. Recent measurements using a more advanced technique⁵⁸ of imaging two-photon fluorescence from colliding pulses in BaF_2 have yielded results which support the two-photon absorption estimate of pulse length.

X-RAY EXPERIMENTAL METHODS

Laser Plasma Diagnostic Apparatus

The analysis of x-ray emissions from heated plasmas has long been valued as an important diagnostic of plasma temperature and density. Starting from simple measurements of high energy continuum emission to diagnostics based on detailed line spectroscopy, many aspects of plasma dynamics and conditions can be studied using spatial and energy resolved x-ray measurements. It is also necessary to know the spectral details of the keV emission because applications in x-ray lithography will require careful characterization of processes which are strongly wavelength dependent.

The diagnostic apparatus used in these experiments is shown in the target chamber schematic in Fig. 19. For the bulk of the experiments the target chamber was evacuated to a pressure of 5×10^{-5} Torr with some additional experiments being performed in atmospheric helium. The laser is directed into the target chamber through a CaF_2 window (to avoid two-photon losses) and onto the dry machined edge of a target disk at normal incidence. The targets are usually solid disks of material but in certain cases foils were wrapped around the disks. The disks are mounted on a computer controlled stepper motor which advances the disk with every shot to present fresh target material. The laser energy was monitored on a shot-to-shot basis using a pyroelectric calorimeter (designed by the author using Kynar piezoelectric film). The pulse shape was also monitored regularly using high speed photodiodes or a streak camera (UV optics designed by author) depending on the resolution required.

In order to make absolute measurements of keV emission it is necessary to know the spectral details accurately so that the energy dependence of the detectors may be taken into account. In the measurement of these x-rays two types of semiconductor diodes have been used as the primary detectors of the absolute yield. In combination

Target Experiment Diagnostics

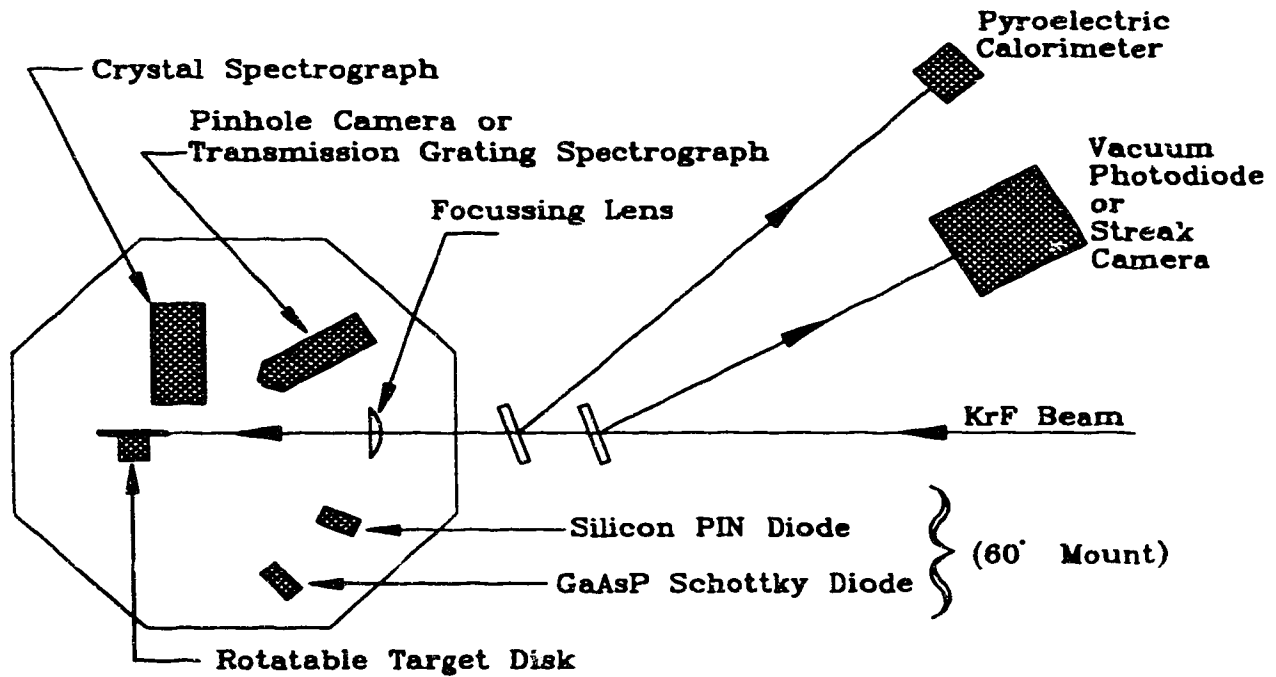


Fig. 19 Schematic diagram of target interaction apparatus.

with these detectors a crystal spectrograph was used to resolve the x-ray emission such that the measured spectrum could be combined with the theoretical response of the detectors yielding accurate results for the absolute measurements. In addition to the semiconductor detectors other detectors have been used to characterize the plasma. For example a pinhole camera was used to measure the size of the keV emission zone. As well, a free-standing 2000 l/mm gold grating in combination with a 25 μm pinhole was used as a transmission grating spectrometer to measure the x-ray spectrum over a wider range down to 100 eV.

One of the most important elements in the target chamber is the lens which focuses the laser light onto the target surface. Two different focusing lenses have been used during the course of the experiments. During the first set of x-ray measurements a 20 cm planoconvex quartz lens was used which provided a 20 μm diameter (50% energy contour) focal spot size with the 100 ps system. This value is obtained using an optical ray tracing code⁵⁹ and the measured value of beam divergence. During these experiments the pulse length was 120 ps and the estimated peak focal intensity was $1.5 \times 10^{14} \text{ Wcm}^{-2}$ for a 50 mJ pulse. This lens was later replaced with an aberration corrected triplet lens with a focal length of 12.5 cm which reduced the calculated focal spot size to an estimated 8 μm (50% energy). In combination with a reduced pulse length of 90 ps the ray tracing code estimate for peak intensity on target is $8 \times 10^{14} \text{ Wcm}^{-2}$ for a 50 mJ pulse. In the case of the 850 fs pulses the typical peak energy on target was 35 mJ due to two-photon losses in the triplet lens. For these pulses the peak intensity on target was estimated to be $6 \times 10^{16} \text{ Wcm}^{-2}$ but it must be noted that this value may be reduced by the effects of self-focusing. Finally, for the stretched pulse duration of 2 ps the energy on target was higher at 40 mJ yielding a peak intensity estimate of $3 \times 10^{16} \text{ Wcm}^{-2}$.

KeV X-ray Measurement Techniques

The primary absolute yield detectors are the silicon *p-i-n* diodes (Quantrad 025- *p-i-n* 250) whose x-ray response is known from manufacturers data and is shown in Fig. 20, and the GaAsP Schottky diodes (Hamamatsu G1127-02) whose response is not as well documented but for which there are published measurements⁶⁰ and sufficient data from which a response characteristic has been constructed. The theoretical response for the GaAsP diodes is also shown in Fig. 20. The detectors have been filtered to restrict the x-ray energies being measured to values where the crystal spectrograph can determine the spectral structure of the emission. One of each of the two types of detectors has been filtered with 9 μm aluminum and the other two detectors are filtered with two layers of B10 filter material⁶¹ (this filter will be identified as 2B10). B10 material is 2 μm thick polycarbonate plastic coated with 0.165 μm of aluminum. Two layers of this material provide a light tight barrier with x-ray transmission μm characteristics similar to 10 μm beryllium. Figure 21 shows the transmission characteristics of the two filter materials and Fig. 22 shows the response functions of the four keV detector/filter combinations. The detector response function $R(E)$ is given by:

$$R(E) = D(E)T(E) \quad \text{C/J} \quad (15)$$

where $D(E)$ is the basic response characteristic of the detector (in C/J) and $T(E)$ is the transmission of the filter. The measured response of the detector itself when exposed to x-rays is an integrated convolution of the detector/filter response function and the x-ray spectrum. This integration takes the form of the charge produced by the detector and measured by an oscilloscope. Analytically, the integrated response (Q) of each detector takes the form:

$$Q = \int_{E_1}^{E_2} D(E)T(E)I_c(E)\Omega dE \quad \text{Coulombs} \quad (16)$$

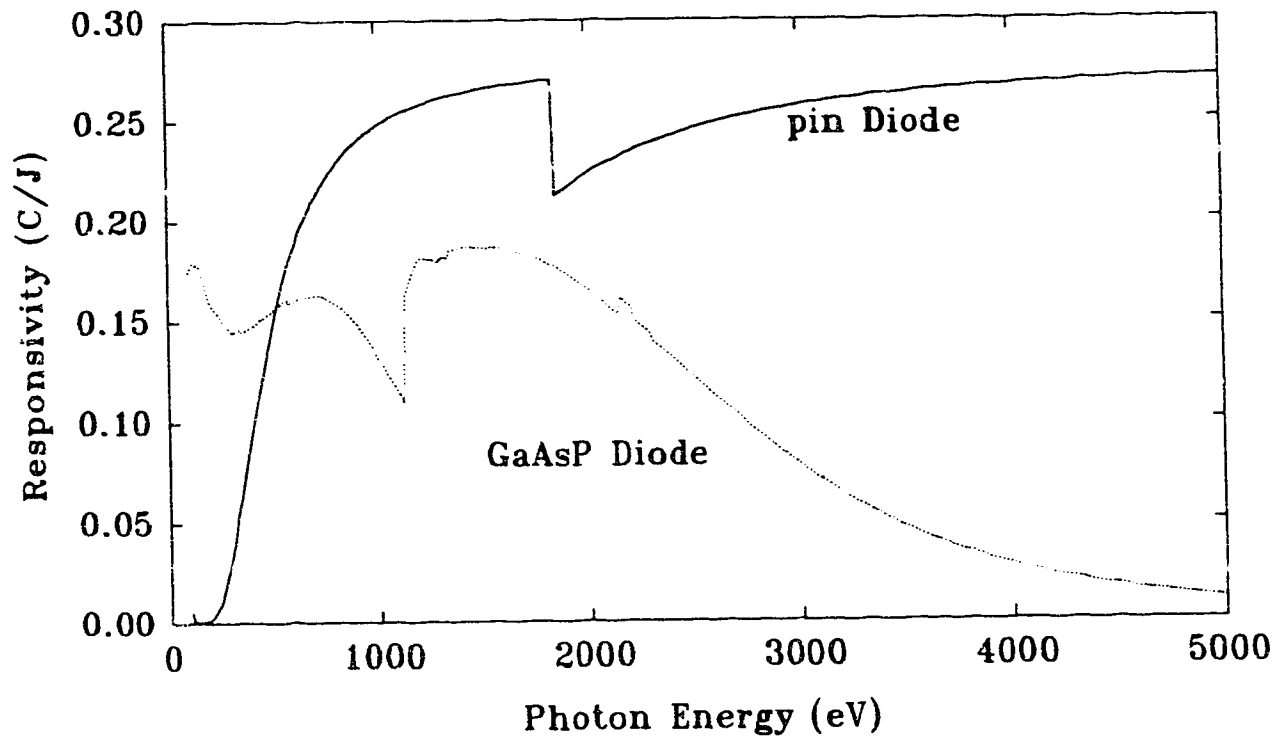


Fig. 20 Theoretical response functions for *p-i-n* diodes and GaAsP diodes as a function of x-ray photon energy.

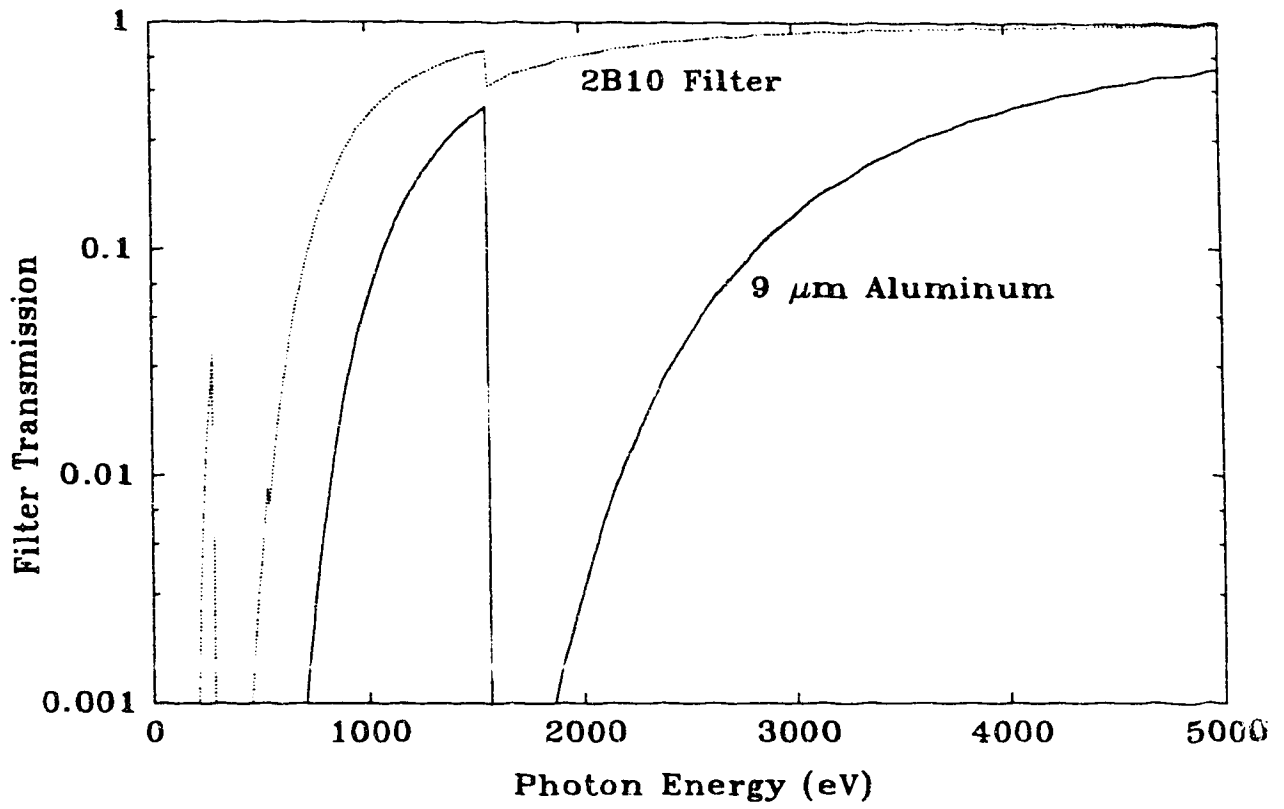


Fig. 21 Transmission characteristics of 9 μm aluminum and 2B10 filters.

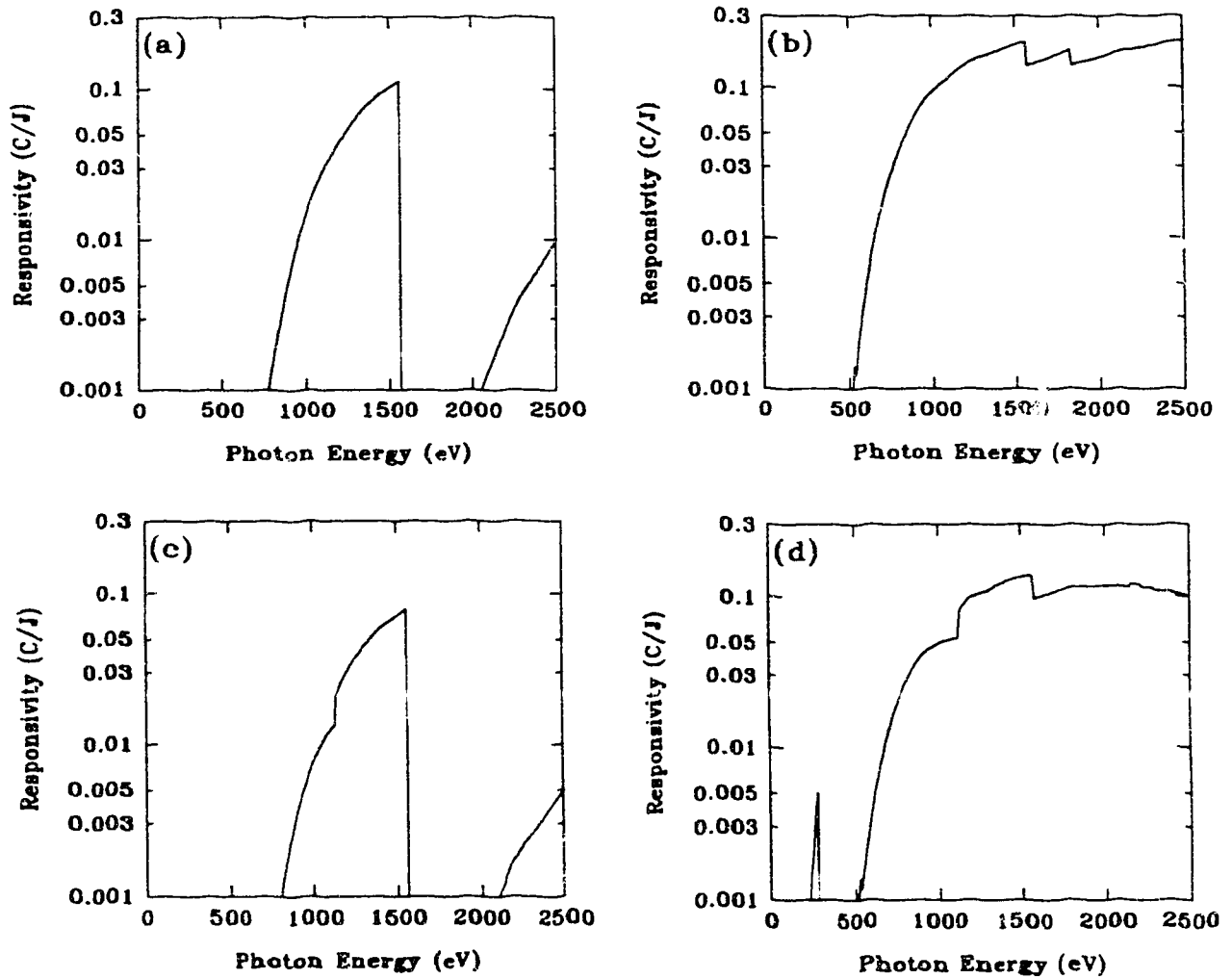


Fig. 22 Theoretical response characteristics for the four detector/filter combinations used in measuring absolute keV x-ray emissions (a) *p-i-n* diode with 9 μm Al (b) *p-i-n* diode with 2B10 (c) GaAsP diode with 9 μm Al (d) GaAsP diode with 2B10.

where $I_e(E)$ is the x-ray spectrum ($\text{JeV}^{-1}\text{sr}^{-1}$), Ω is the solid angle of the detector and E_2 and E_1 are, in principle, the physical limits of the x-ray spectrum. However, it is a very difficult task to measure the complete x-ray spectrum in detail. Some simple assumptions can be made which lead to correct results even though the range of the spectral measurements is restricted. The first and most important step is filtering the detectors to restrict the range of x-rays being detected to the keV range. As long the x-ray spectrum is known over the range where there is significant sensitivity from the detector/filter combination then it is not necessary to know the whole spectrum. This allows a restriction of the range of integration ($E_1 - E_2$) to some range of values where the contribution to the total charge from x-rays detected outside this range is small.

Several different crystal spectrographs have been used to measure the detailed x-ray spectrum in the 800 - 1600 eV region as well as some spectra in the 1600 - 2300 eV region. X-ray diffraction from crystals is governed by the equation:

$$\lambda = 2d \sin \theta \quad (17)$$

where d is the spacing between the crystal planes, θ is the angle of incidence measured from the crystal planes and λ is the wavelength of the diffracted x-rays. During the course of the experiment three types of x-ray diffracting crystals have been used. The first set of experiments were done using a thallium acid phthalate (TAP $2d=25.76 \text{ \AA}$) crystal which was relatively small in size ($5 \text{ mm} \times 10 \text{ mm}$) and as a result the spectra were acquired in two overlapping sections. For the second series of experiments the TAP crystal was replaced with a rubidium acid phthalate (RAP $2d=26.1 \text{ \AA}$) crystal which was large enough to obtain complete spectra on a single piece of film. The third type of crystal was Ammonium Dihydrogen Phosphate (ADP $2d=10.64 \text{ \AA}$) which was used in obtaining spectra in the higher range of 1600 - 2300 eV. All of the spectra generated from the crystal reflections were recorded on Kodak DEF film. The films were scanned using a Joyce Loebel microdensitometer ($NA = 0.25$) connected to a microcomputer to record the data for digital processing. The data was converted from measured film

density to photon flux $I_p(E)$ using the calibration model of Henke et. al.⁶². The data was also corrected^{63,64} for the energy dependent integrated crystal reflectivity $R_c(E)$ and for the filter transmission according to the equation:

$$I_e(E) = I_p(E)E \frac{d\theta}{dE} \frac{r^2}{R_c(E)} \frac{1}{T(E)} \quad (18)$$

where:

$$\frac{dE}{d\theta} = E \left[\left(\frac{2dE}{hc} \right)^2 - 1 \right]^{1/2} \quad (19)$$

and E is the photon energy, $I_e(E)$ is the x-ray energy flux per steradian per eV, $T(E)$ includes the transmission of the 2B10 filter which protects the film from room light as well as the 2 μ m polycarbonate filter which protects the crystal from target debris, $d\theta/dE$ is the crystal dispersion, r is the source to film distance and hc is the product of Planck's constant and the speed of light. The digitized and deconvolved spectra which are the final result from the crystal spectrograph are normalized to produce unit area under integration over their energy limits. After convolution this is equivalent to saying that the measured spectrum is the complete spectrum (at least as far as the filtered detectors are concerned). This allows us to return to Eqn. 16 and say that E_2 and E_1 are the limits of the measured spectrum and that we use the normalized spectrum $I_n(E)$ where:

$$I_n(E) = \frac{I_e(E)}{\int_{E_1}^{E_2} I_e(E) dE} \quad eV^{-1}Sr^{-1} \quad (20)$$

The value of $I_n(E)$ is that only the structure of the spectrum is retained and not the absolute value. This allows definition of an integrated responsivity for each detector/filter/spectrum combination. This integrated responsivity is defined as:

$$R_1 = \int_{E_1}^{E_2} D(E)T(E)I_0(E)dE \quad \text{CJ}^{-1}\text{Sr}^{-1} \quad (21)$$

Assuming an isotropic distribution, the absolute x-ray yields can be determined from:

$$Y_1 = \frac{2\pi}{\Omega} \frac{Q}{R_1} \quad \text{J} \quad (22)$$

where Y_1 is the integrated x-ray energy yield in the range E_2 to E_1 , Ω is the solid angle subtended by the detector and Q is the integrated charge from the detector.

Note that depending on the actual angular position of the detectors different angular dependences of x-ray emission can be incorporated into the calculation. All of the detectors are set at 60° from the target normal which allows for a minimum of error so long as the actual distribution is somewhere between isotropic and lambertian (corresponding to a $\cos^\alpha(\theta)$ dependence with $\alpha = 0 - 1$). Figure 23 shows the error incurred for various detector angles as a function of α . In fact, as will be shown later, this assumption has been proven valid.

In addition to the main keV measurement system additional measurements were made for which data will be presented in the subsequent chapter. One such measurement is the use of a pinhole camera (PHC) which used a pair of pinholes ($12.5 \mu\text{m}$ and $30 \mu\text{m}$ diameter) to measure the diameter of the keV emission region. The camera was typically held at 45° off target normal so that an estimate of the plasma diameter could be obtained. The fact that a $12.5 \mu\text{m}$ pinhole is being used to view a focal spot which is expected to be $10 \mu\text{m}$ in diameter is problematic but it is possible to make an estimate of the diameter from geometric imaging⁶⁵ because the penumbral enlargement of the spot is a result of the finite size of the plasma source. This system provides no spatial resolution but the primary concern is obtaining a reasonable estimate for the size of the keV emission zone. Another diagnostic which was used with the 100 ps system was the

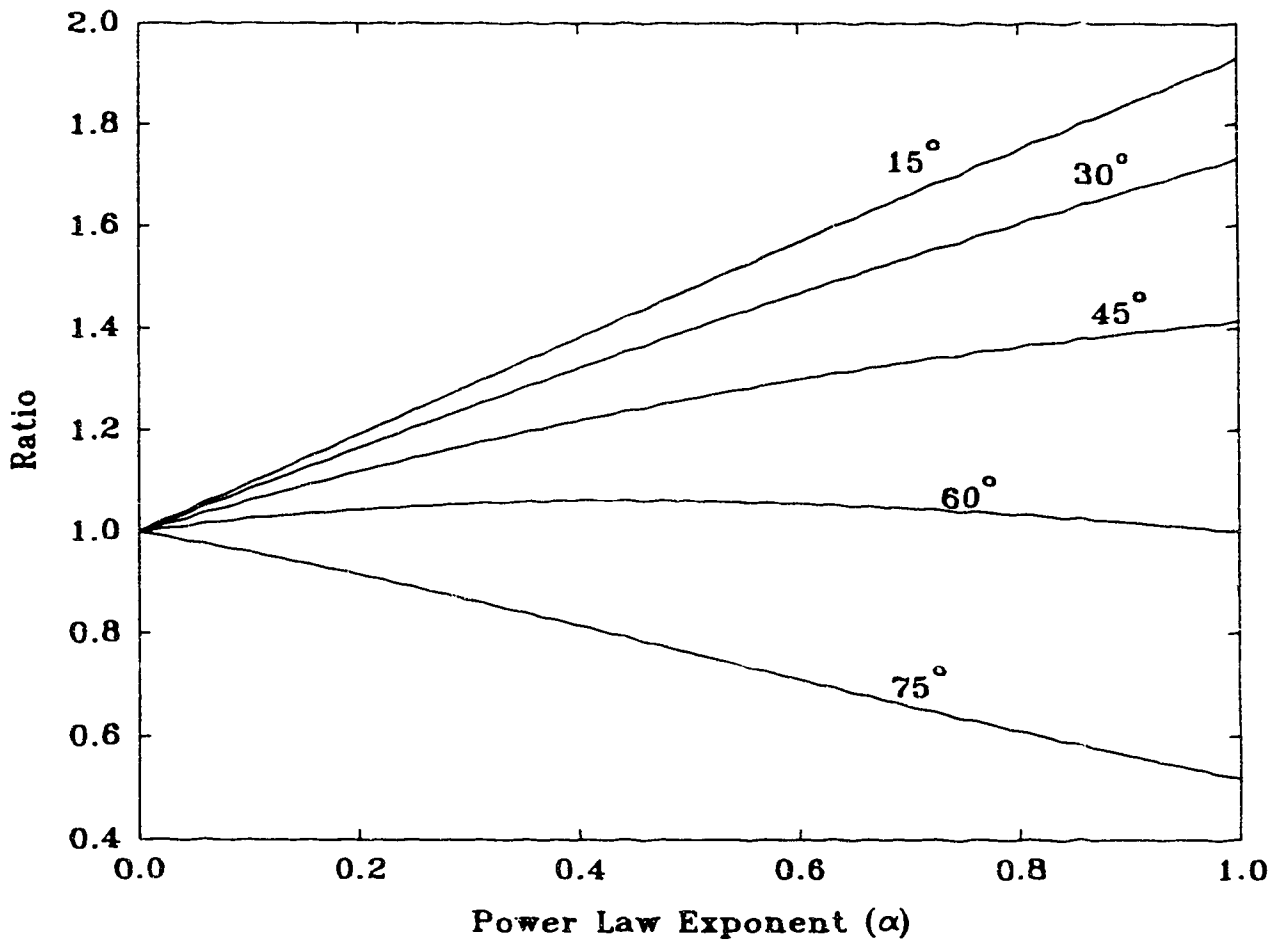


Fig. 23 Ratio of integrated emission under isotropic assumption to cosine power law showing that the use of the 60 degree viewing angle introduces no more than 6% error for distributions between isotropic ($\alpha=0$) and lambertian ($\alpha=1$).

transmission grating spectrometer (TGS). For these measurements a 25 μ m diameter pinhole with a free standing 2000 l/mm gold grating was used to obtain dispersed x-ray spectra down into the 100 eV region. The spectra obtained with this instrument were recorded on Kodak 101-07 film. The resolution of the TGS was limited to about 2 Å which is inadequate for calculating detailed yields in the keV region but is useful for characterizing overall x-ray emission.

X-RAY EXPERIMENTAL RESULTS

The x-ray experiments conducted using the laser systems developed for this project have proceeded in two basic stages. These first and second stages are differentiated by the laser intensities and the x-ray yields achieved and will be referred to as the low and high intensity experiments (or stages) respectively. The first set of x-ray conversion measurements were obtained in the summer of 1990 following the completion of the infrastructure of the laser laboratory and the development of the 100 ps dye laser. Analysis of those results was initially delayed in preference of development work on the 1 ps laser system. The analysis was undertaken beginning in spring 1991 with submission for publication in late summer 1991. The results were subsequently published¹⁹ in the Journal of Applied Physics in February 1992. The second stage of the experiments began in the fall of 1991 when both the 100 ps and 1 ps systems were brought into simultaneous operation. The main physical differences between the first and second stages of the x-ray experiments are as follows. During the first stage of the x-ray experiments a 20 cm focal length planoconvex lens was used to focus the laser on target resulting in a peak intensity of $1.5 \times 10^{14} \text{ Wcm}^{-2}$. For the second stage this was switched to an aberration corrected triplet with a focal length of 12.5 cm resulting in a smaller focal spot. The frequency doubling crystal was changed from urea to BBO which lead to improvements in beam quality and reliability of second harmonic generation. Improvements were made in the setup techniques for the 100 ps dye laser system and resulted in a reduction of pulse length from 120 ps in the first stage to 90 ps in the second stage of the experiments. The modifications for the second stage resulted in estimated peak focal intensities ranging from $8 \times 10^{14} \text{ Wcm}^{-2}$ for the 90 ps pulse to $6 \times 10^{16} \text{ Wcm}^{-2}$ for the 850 fs pulse.

X-ray Spectra

Figure 24 shows a typical raw spectrum from the RAP spectrometer for copper with a number of the principal neon-like spectral lines identified. Copper is a standard element for evaluation of diagnostic performance and for comparison to results from other groups in the keV x-ray range. Wavelength calibration of the keV spectra is achieved in one of two ways: the preferred method is to use identifiable lines (such as neon-like) within the spectrum, the alternate technique is to use a second target material such as Teflon (which contains fluorine) to produce easily identifiable lines superimposed on the spectrum under study. Both methods have been used in these experiments and once lines have been identified for a particular material the second method is simply a verification of results of the first. Gordon et al.⁶⁶ have published a list of spectral features which have been used extensively in calibrating the spectra obtained since the dominant ionic stages in these plasmas (for the mid Z_N targets Fe through Zn) are neon, fluorine and oxygen-like. Table 1 lists the principal neon-like transitions used in calibrating the mid Z_N target spectra.

Table 1 Wavelengths (in Angstroms) of transitions used in calibrating the mid Z_N spectra. The spectral features are identified in Fig. 24. After Gordon et al.⁶⁶

	Transition	Iron	Cobalt	Nickel	Copper	Zinc
A	$2s^2 2p^6 - (2p^5(^2P_{1/2}), 4d(^2D_{5/2}))_1$	12.123	10.975	9.977	9.106	8.345
B	$2s^2 2p^6 - (2p^5(^2P_{3/2}), 4d(^2D_{5/2}))_1$	12.264	11.108	10.110	9.237	8.471
C	$2s^2 2p^6 - (2p^5(^2P_{1/2}), 3d(^2D_{5/2}))_1$	15.015	13.634	12.435	11.383	10.458
D	$2s^2 2p^6 - (2p^5(^2P_{3/2}), 3d(^2D_{5/2}))_1$	15.262	13.868	12.656	11.594	10.664
E	$2s^2 2p^6 - (2p^5(^2P_{1/2}), 3s)_1$	16.777	15.169	13.779	12.570	11.512
F	$2s^2 2p^6 - (2p^5(^2P_{3/2}), 3s)_1$	17.054	15.437	14.043	12.827	11.765

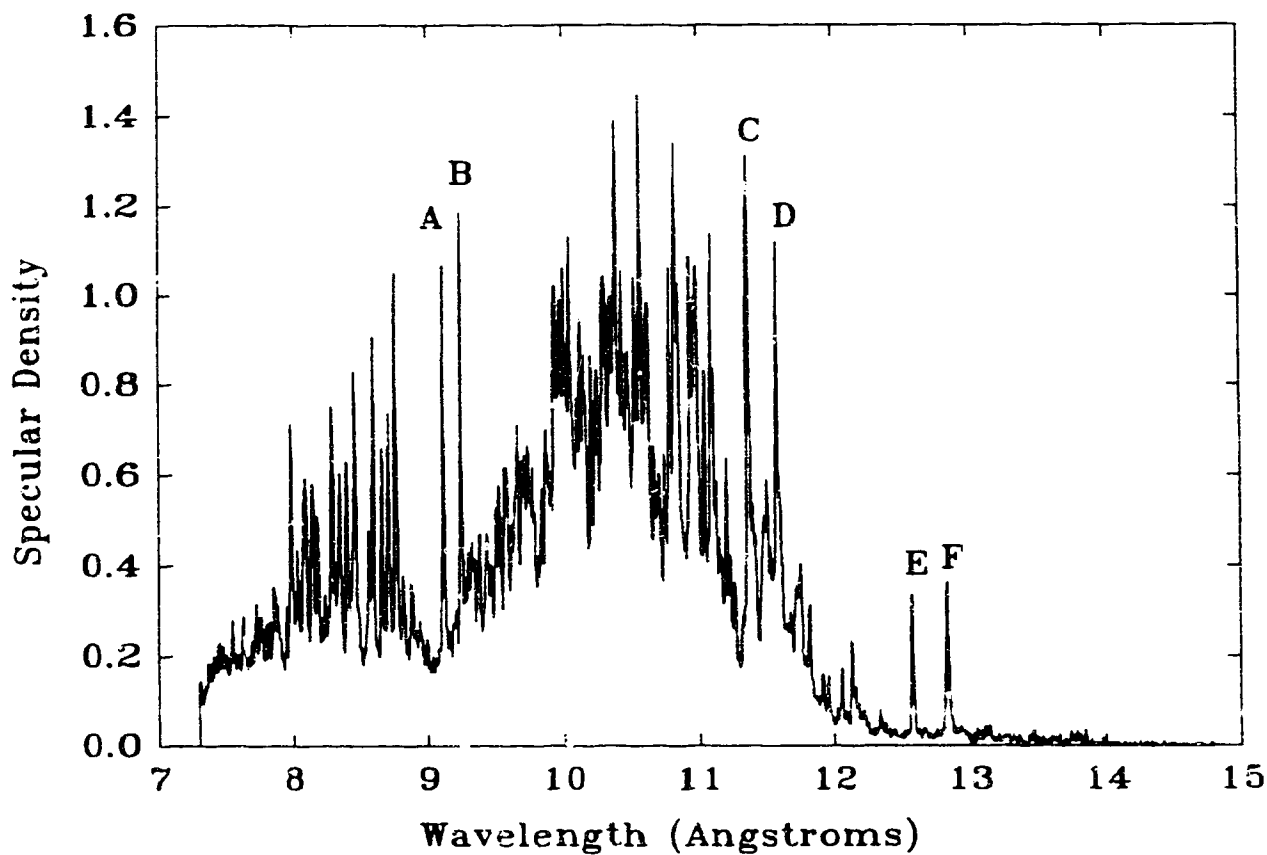


Fig. 24 Typical densitometer scan of a copper spectrum recorded on Kodak DEF film and measured using Joyce Loebel microdensitometer (NA=0.25). Some of the major neon-like lines used to calibrate the wavelength scale have been marked and are listed in Table 1.

As discussed previously, the digitized film densities are deconvolved from the DEF film response according to Henke's model and corrected for crystal and filter response. Figures 25a - 25e show the final normalized spectra from the TAP crystal spectrometer obtained for five elements (Ti, Fe, Ni, Cu and Sn) using the 120 ps pulse and the 20 cm lens where the peak intensity is estimated to be $1.5 \times 10^{14} \text{ Wcm}^{-2}$. These spectra are acquired at a typical pulse energy of 50 mJ with the number of required shots ranging from 10 - 30. At this intensity the spectra from the mid Z_N targets (Fe, Ni and Cu) are dominated by neon-like features. In addition to the neon-like features in the mid Z_N targets, fluorine-like and oxygen-like features have been identified and in the titanium spectra lithium-like features provide the visible structure. The tin spectrum shows a distinct lack of line features which is the result of line structure merging into band structure with the transition from L shell emission to M shell emission. It should be noted that the highly detailed structure which appears in the low energy end of the tin spectrum and in the low end of some of the other spectra is the result of the decreasing sensitivity of the combination of the 2B10 filter and the DEF film. As the sensitivity drops the grain noise of the film becomes strongly amplified through the deconvolution process.

Figures 26a - 26g show the spectra from the RAP crystal spectrometer obtained using the 90 ps pulse and the triplet lens where the peak intensity is estimated to be $8 \times 10^{14} \text{ Wcm}^{-2}$. These spectra were also taken at a typical laser energy of 50 mJ with the number of shots ranging from 5 - 20. The same elements were tested as were used in the previous experiment plus two more: cobalt and zinc were added to expand the selection of the mid Z_N elements. A number of important changes in the spectra have occurred with the increase in laser intensity. The most notable effect is the shift of the emission peaks by almost 100 eV to higher energies which is correlated with the increase in fluorine-like and oxygen-like spectral structures as the (mid Z_N) materials become ionized beyond the neon-like state. The tunability of the keV x-ray emission peak by

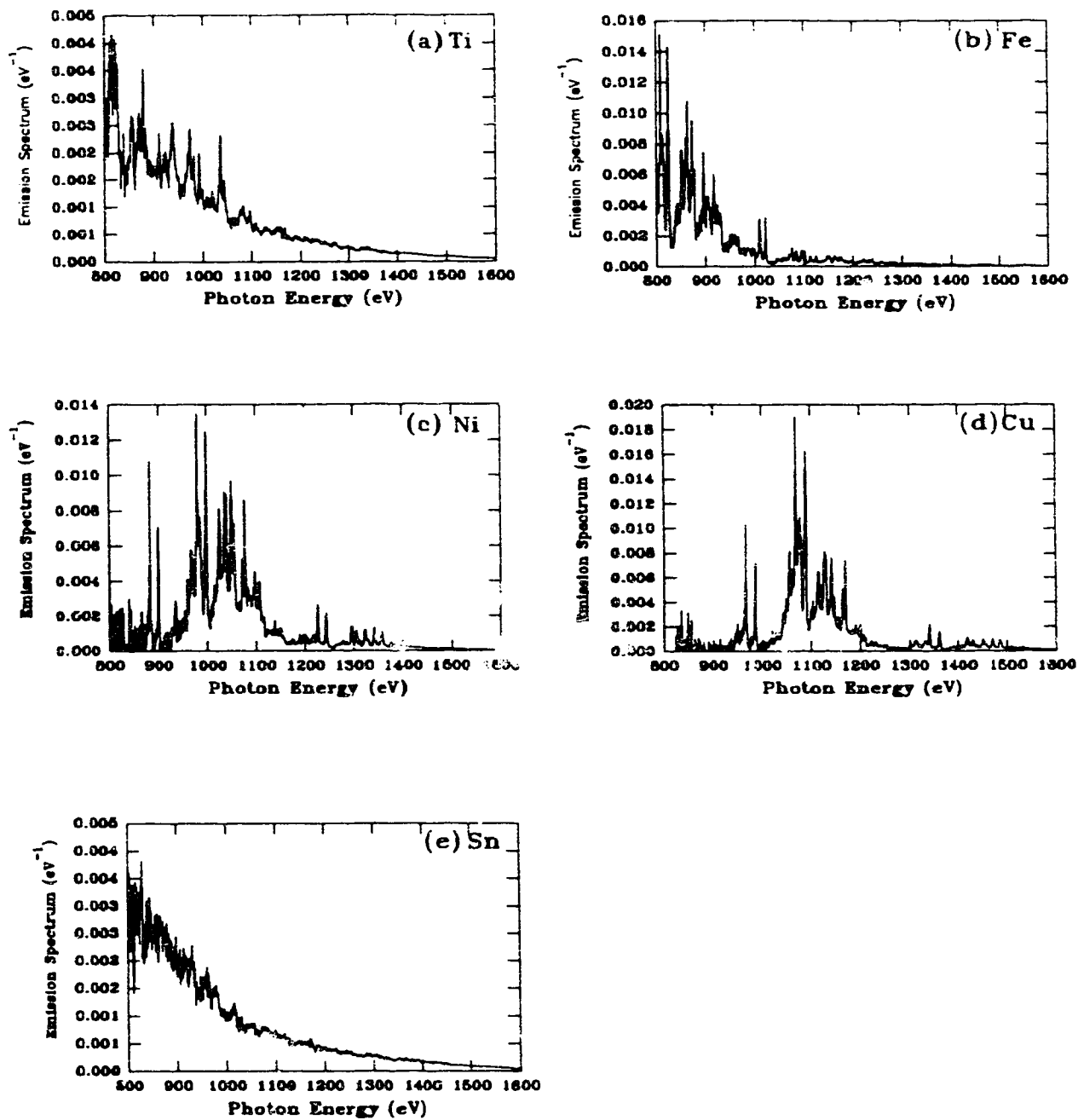


Fig. 25 Final keV spectra for pure target materials obtained with 120 ps pulse at intensity $1.5 \times 10^{14} \text{ W m}^{-2}$. Materials are (a) Titanium, (b) Iron, (c) Nickel, (d) Copper and (e) Tin.

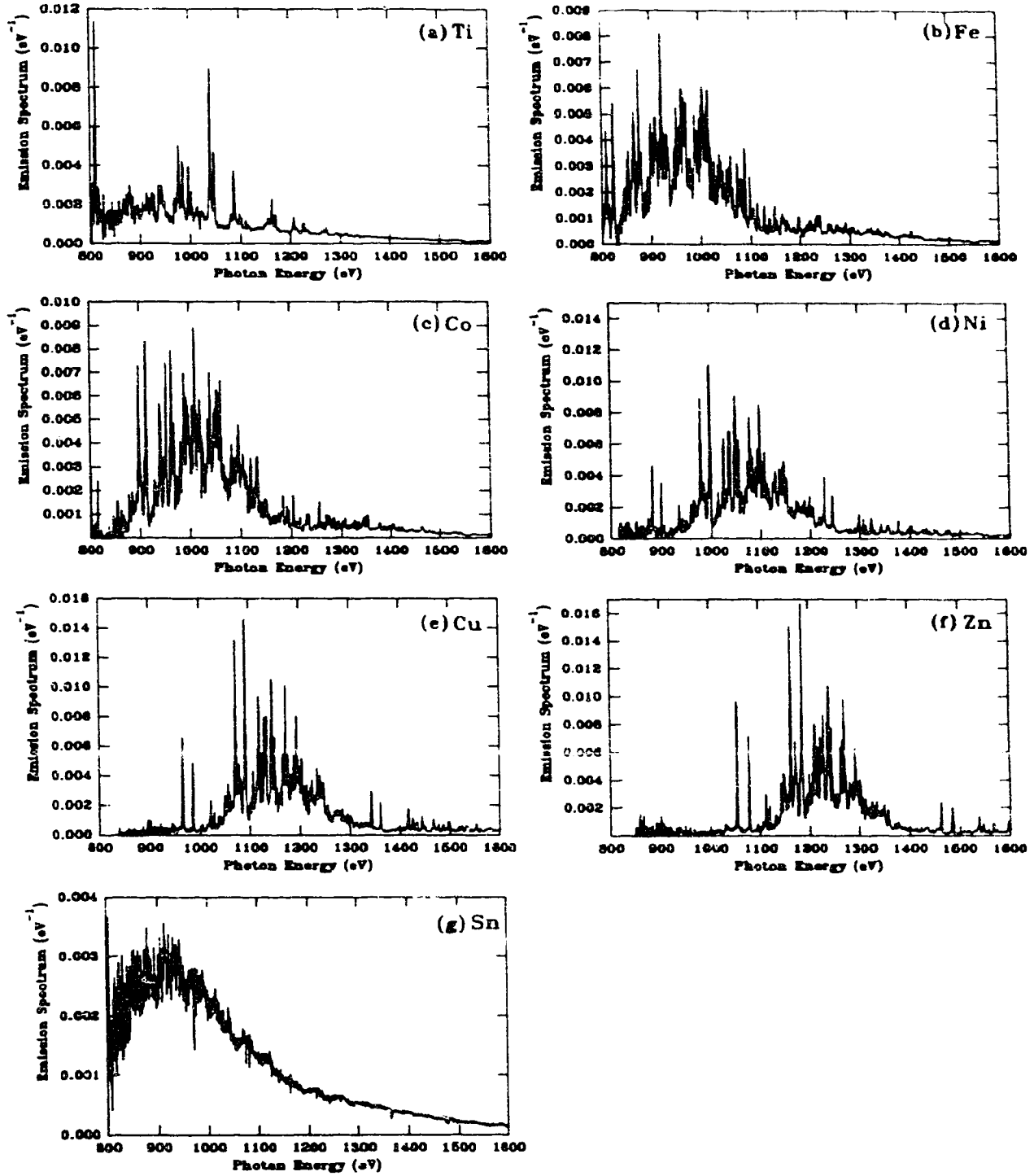


Fig. 26 Final keV spectra for pure target materials obtained with 90 ps pulse at intensity $8 \times 10^{14} \text{ Wcm}^{-2}$. Materials are (a) Titanium, (b) Iron, (c) Cobalt (d) Nickel, (e) Copper, (f) Zinc and (g) Tin.

selection of target material has been discussed by other groups⁶⁷ and can be clearly seen in the results here. The lithium-like structure from titanium occurs in the keV range but in comparison to the other spectra it is relatively flat because the L shell emission peak is down near 600 eV and as a result provides poor emission characteristics in the keV range. The iron spectrum shows the rise of the keV emission structure with a spectrum that is heavily mixed between neon, fluorine and oxygen-like with a centroid of emission near 950 eV. The continuing progression through cobalt, nickel, copper and zinc all show the trend of the shift in the emission centroid increasing from 1000 eV to 1250 eV. Also clearly visible is the reduction in the complexity of the spectral structure with increasing Z_N as the spectra become more dominated by the neon-like state and the ionization into the fluorine and oxygen states decreases due to increasing ionization energies. The tin spectrum with its peak at 900 eV has a centroid which is close to that expected for manganese (in the L shell series) in terms of where the spectral peak falls except it represents the beginning of the keV emission in the M shell series.

In the density and temperature regimes in which the x-ray production is predicted to occur it is expected that the plasma will become sufficiently optically dense that the escape of the keV radiation from the plasma becomes impeded by repeated absorption and emission processes. In such an optically dense regime it may be possible to reduce the opacity of the main emitting species by using a mixed target such that the emission lines from the main component are interleaved with those of a second component thus lowering the concentration and therefore the opacity of each component. In addition to the pure materials tested for x-ray conversion efficiency in the 100 ps pulse length regime three mixed species materials have been tested to check for the possibility of opacity as a limiting factor as well as to provide for the possibility of additional tuning. Mixed species may also be desirable in an engineered laser plasma x-ray source on the basis of mechanical properties in a target mechanism (i.e. high strength thin foils). The materials tested were German Silver (63% Cu, 21% Zn, 13% Ni, 3% Mn), Inconel 750

(74% Ni, 15% Cr, 7% Fe, 2.5% Ti plus trace elements) and Brass (generic Brass assumed to be 70% Cu, 30% Zn). The spectra from the mixed species are shown in Figs. 27a - 27c and possess features which are largely similar to those seen in the pure material spectra with the expected overlap of features from each contributing material. It may be noted at this point that no enhancement of yields was observed from these materials. The lack of increased yields does not necessarily imply that opacity is not a problem since the mixed species were chosen on the basis of what was available as opposed to designing an ideal target. It is possible that a mixture of something like 90% aluminum and 10% copper would provide more information on the opacity question.

Figures 28a - 28e show a set of spectra for titanium, iron, nickel, copper and tin obtained using the short pulse system where the pulse is in its "stretched" mode with pulse length 2 ps. These spectra are obtained at a typical pulse energy of 35 - 40 mJ with the number of shots required ranging from 5 to 20. It may be observed that the spectra are generally similar to those from the 90 ps pulse but that there is an additional increase in the complexity of the structure of the spectra as well as an additional slight shift in the centroid of emission by 50 eV. This indicates that a hotter plasma has been formed. Figure 28f shows the copper spectrum obtained with the 850 fs pulse at a typical pulse energy of 35 mJ. This spectrum is closer in structure to the 90 ps spectrum as evidenced by the stronger neon-like lines indicating that a slightly lower average ionization stage has been reached than was the case for the 2 ps pulse. This indicates that in spite of the lower estimated intensity the 2 ps pulse is able to achieve a higher plasma temperature.

In addition to the spectra recorded in the 800 - 1600 eV range with the RAP spectrometer, spectra have also been recorded for aluminum using an ADP crystal in the 1600 - 2300 eV range. This diagnostic is specifically designed to be able to record the emission spectrum of aluminum. Aluminum is a valuable material in laser plasma interaction diagnostics. Many of the laser plasma interaction simulations which are in existence are for aluminum because it is an atomically simple (relative to other materials)

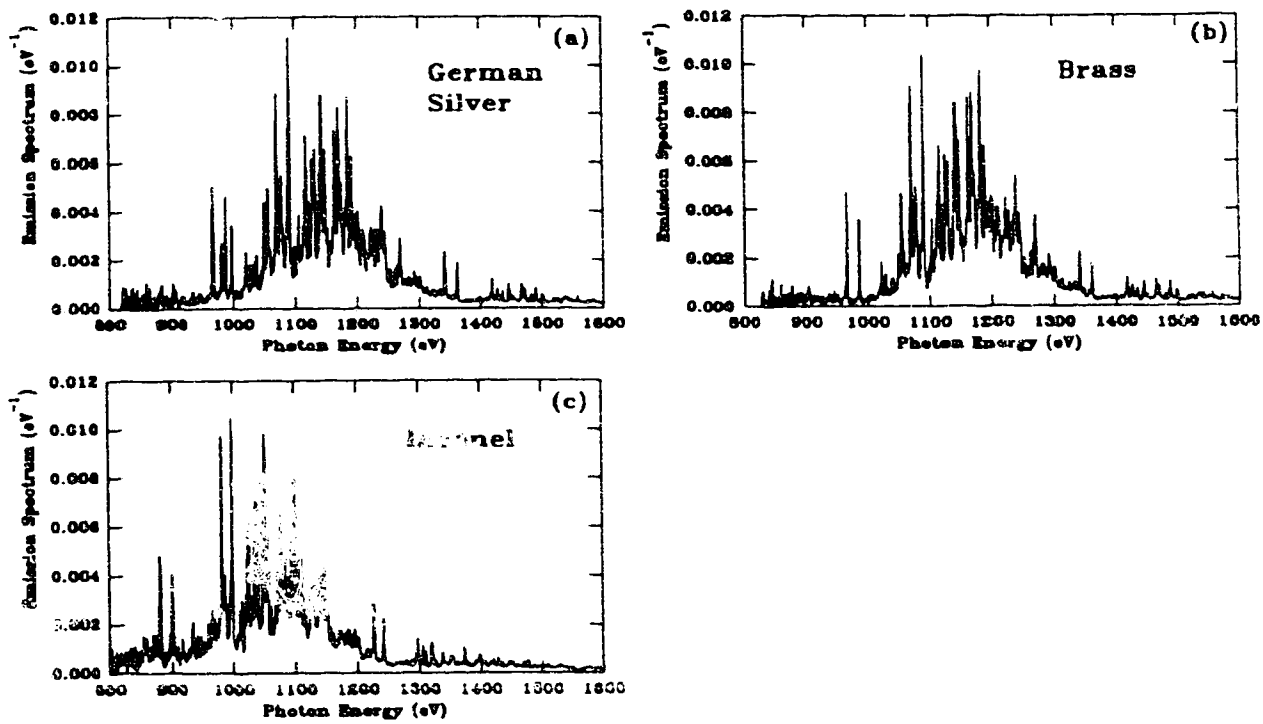


Fig. 27 Final keV spectra for mixed target materials obtained with 90 ps pulse at intensity $8 \times 10^{14} \text{ Wcm}^{-2}$. Materials are (a) German Silver, (b) Brass, (c) Inconel 750.

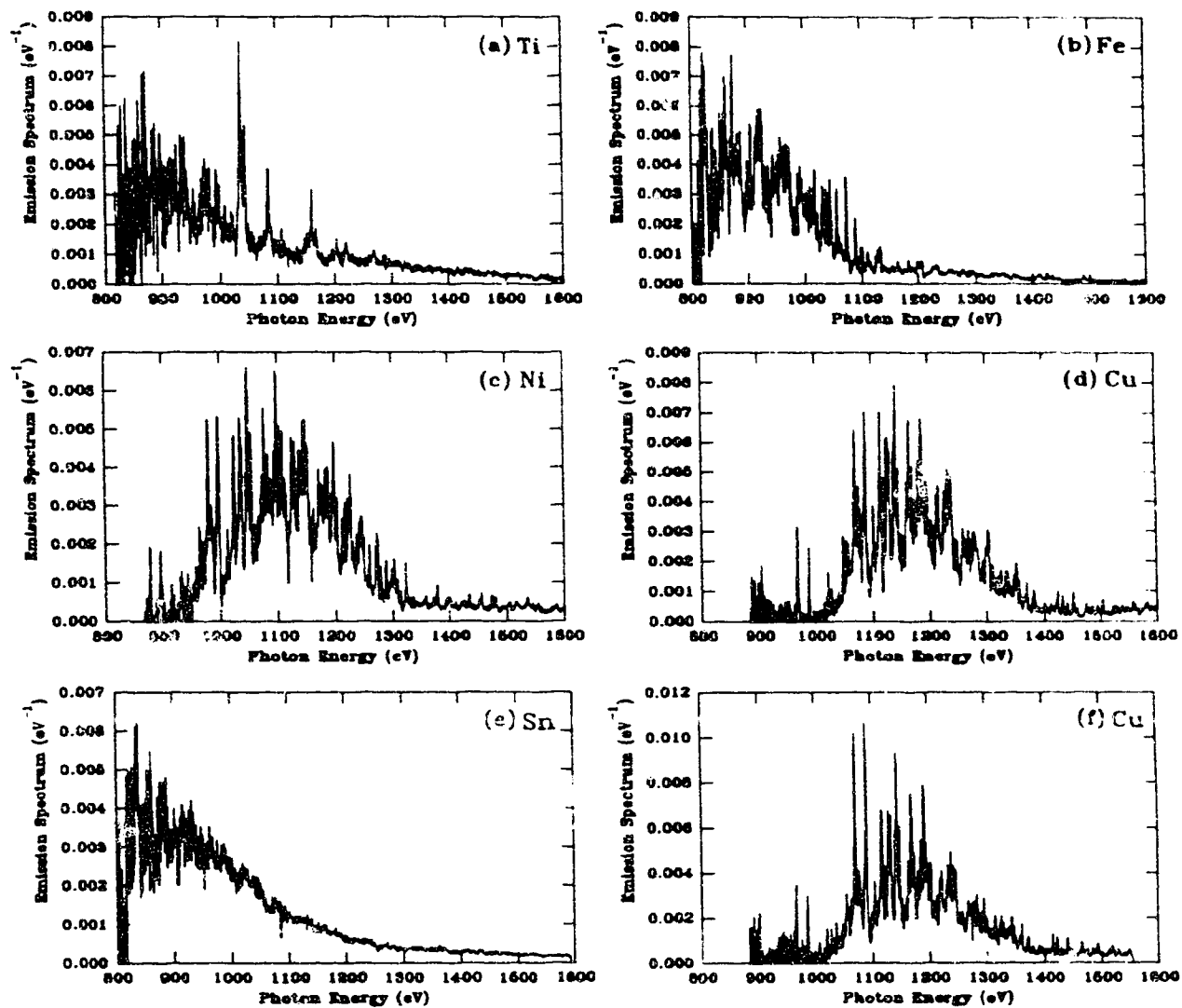


Fig. 28 Final keV spectra obtained with the "stretched" 2 ps pulse at an intensity of $3 \times 10^{16} \text{ Wcm}^{-2}$. Materials are (a) Titanium, (b) Iron, (c) Nickel, (d) Copper and (e) Tin. Also shown in (f) is copper spectrum obtained with 850 fs pulse at intensity of approximately $6 \times 10^{16} \text{ Wcm}^{-2}$.

material for calculations and is an easily fabricated target material for experiments. Considerable study has been devoted to the examination of the spectrum emitted by helium-like and hydrogen-like atoms and estimates of plasma conditions can sometimes be made from the relative sizes of the hydrogen and helium lines as well as from the sizes of the satellite lines. Figures 29a - 29c show aluminum spectra taken using the ADP crystal for the three different pulse length regimes. The increase in the hydrogenic component of the 2 ps spectrum supports the indications from the copper spectra that the temperature has increased at this pulse length.

TGS and Pinhole Camera Measurements

In addition to the detailed keV spectral measurements made with the crystal spectrographs a transmission grating spectrometer (TGS) was used with the 100 ps system to study the emission spectrum over a wider range. The TGS uses a 25 μm pinhole with a free-standing gold grating⁶⁸ of 2000 lines/mm to disperse the x-rays over a region of 100 - 1600 eV. The x-rays are dispersed onto Kodak 101-07 film which is sensitive over this entire range. The film densities are processed in a manner similar to those of the crystal spectrograph. They are deconvolved from the film response function⁶⁹ and the grating dispersion and efficiency functions⁷⁰ on a microcomputer. The resolution of the TGS is estimated from the geometry of the camera to be $\sim 2 \text{ \AA}$ which is poor for the keV ($< 10 \text{ \AA}$) region but is useful for the lower energies down to 100 eV (124 \AA). Figures 30a and 30b show the raw film response with nickel as a target material from the low ($1.5 \times 10^{14} \text{ W / cm}^2$) and high intensity ($3 \times 10^{14} \text{ W / cm}^2$) stages of the 100 ps system. Figures 31a - 31e show the deconvolved TGS spectra for titanium, iron, nickel, copper and tin in the low intensity experiment where the 20 cm lens was used. Figures 32a - 32g show the same spectra taken plus cobalt and zinc during the high intensity experiment where the 12.5 cm aberration corrected lens was used. These spectra show a somewhat flatter structure than that observed in the low intensity

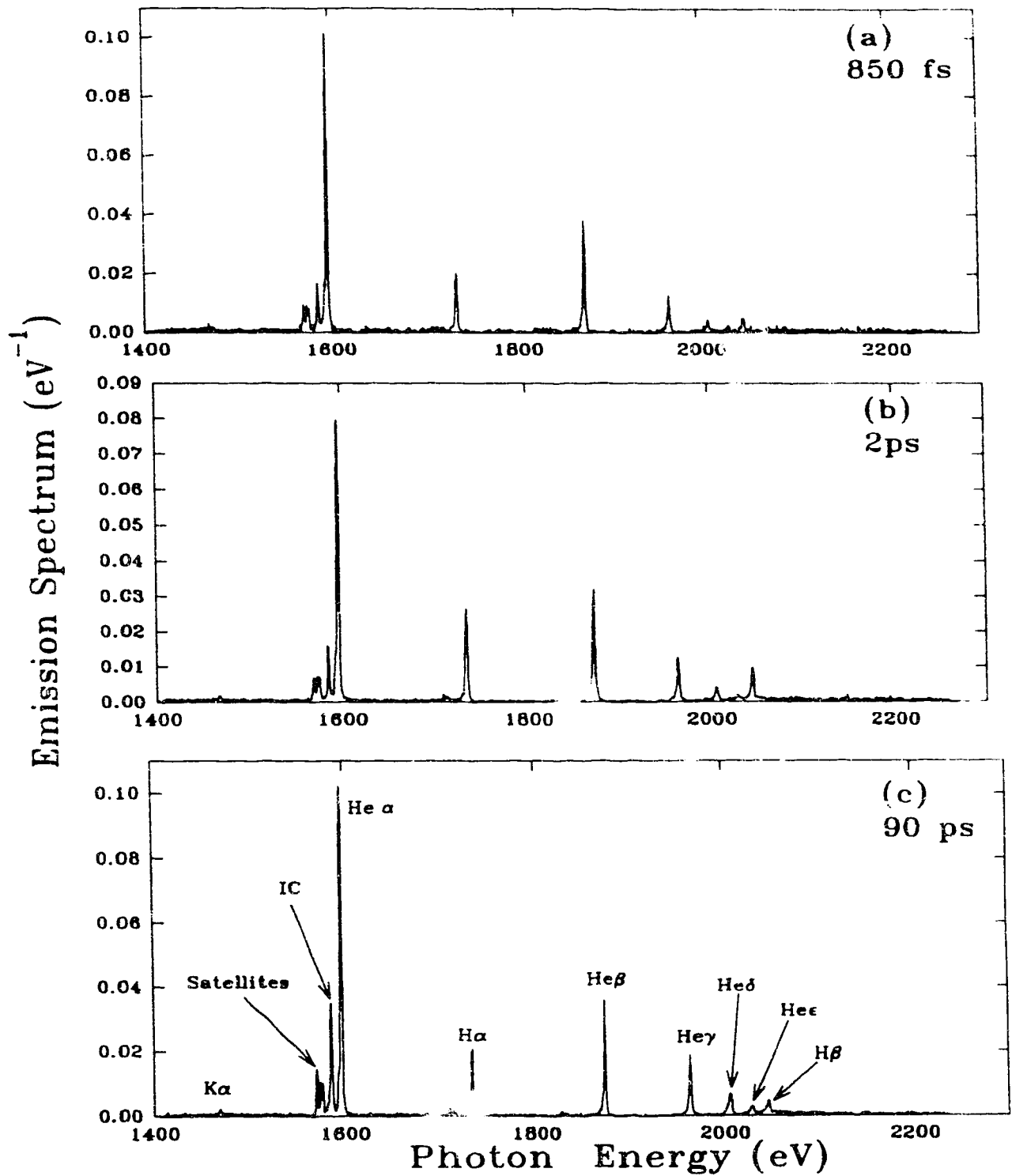


Fig. 29 Aluminum spectra in 1400 - 2300 eV range showing helium and hydrogen-like spectral structures. Produced with (a) 850 fs, (b) 2 ps and (c) 90 ps pulses. Note that the He α has been permitted to saturate in order to enhance the other structures.

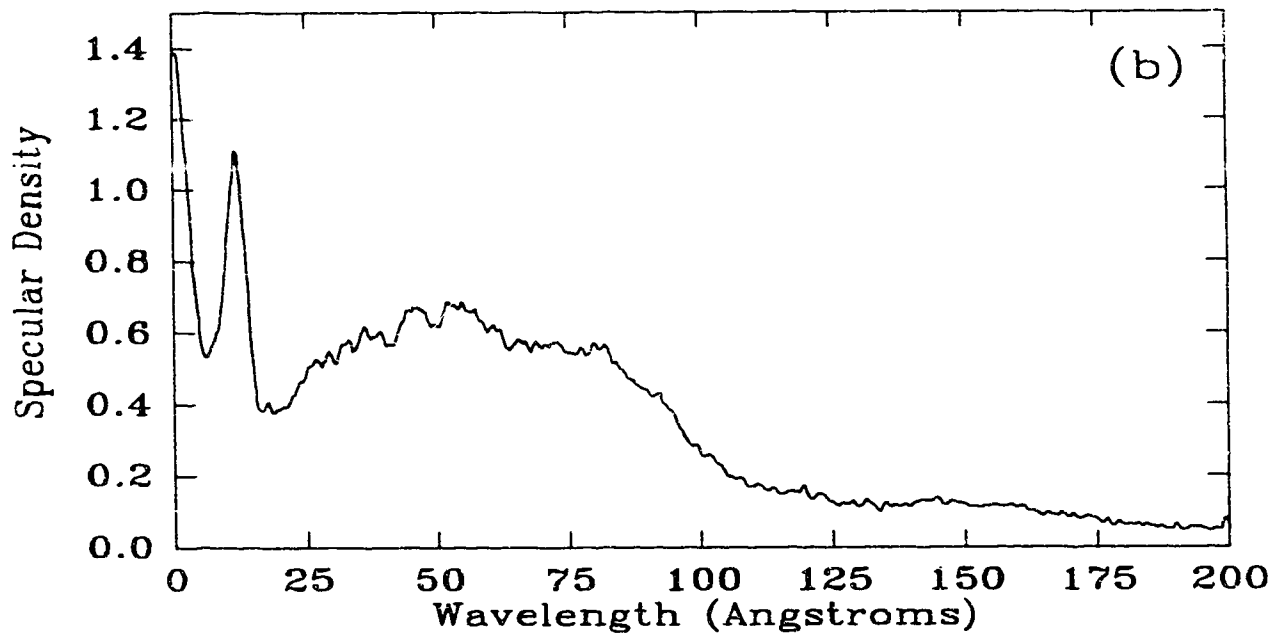
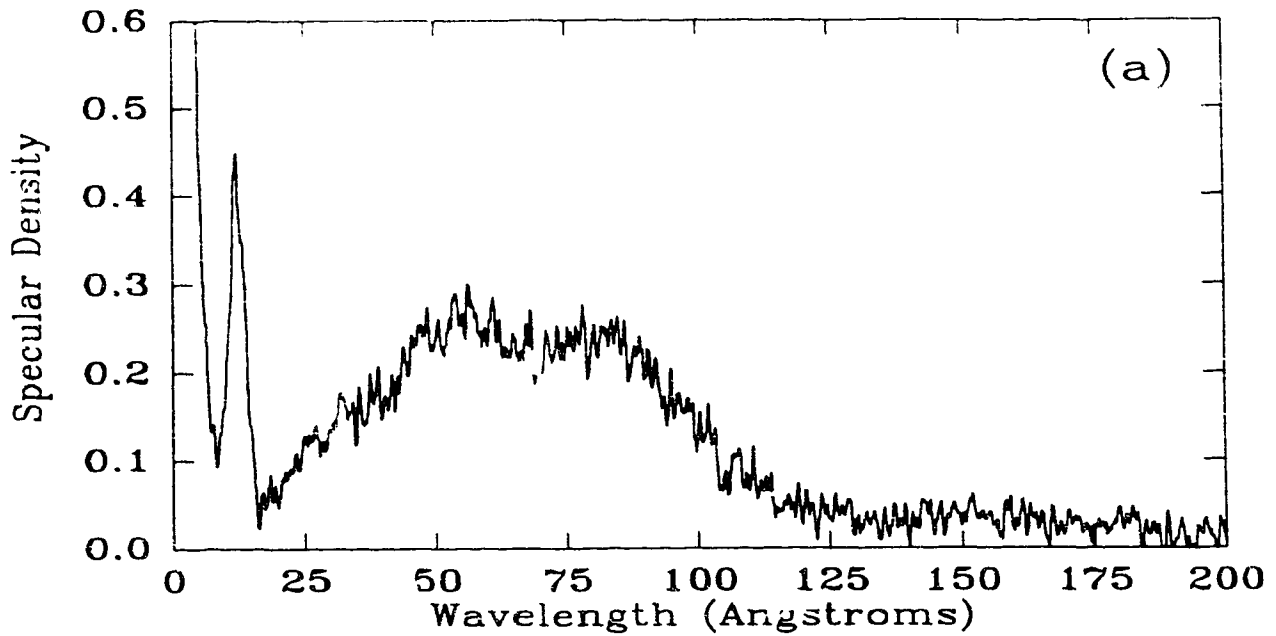


Fig. 30 Raw data from TGS for nickel. Recorded on Kodak 101-07 film and measured with Joyce Loebel microdensitometer (NA=0.25). (a) 120 ps pulse at $1.5 \times 10^{14} \text{ Wcm}^{-2}$ and (b) 90 ps pulse at $8 \times 10^{14} \text{ Wcm}^{-2}$

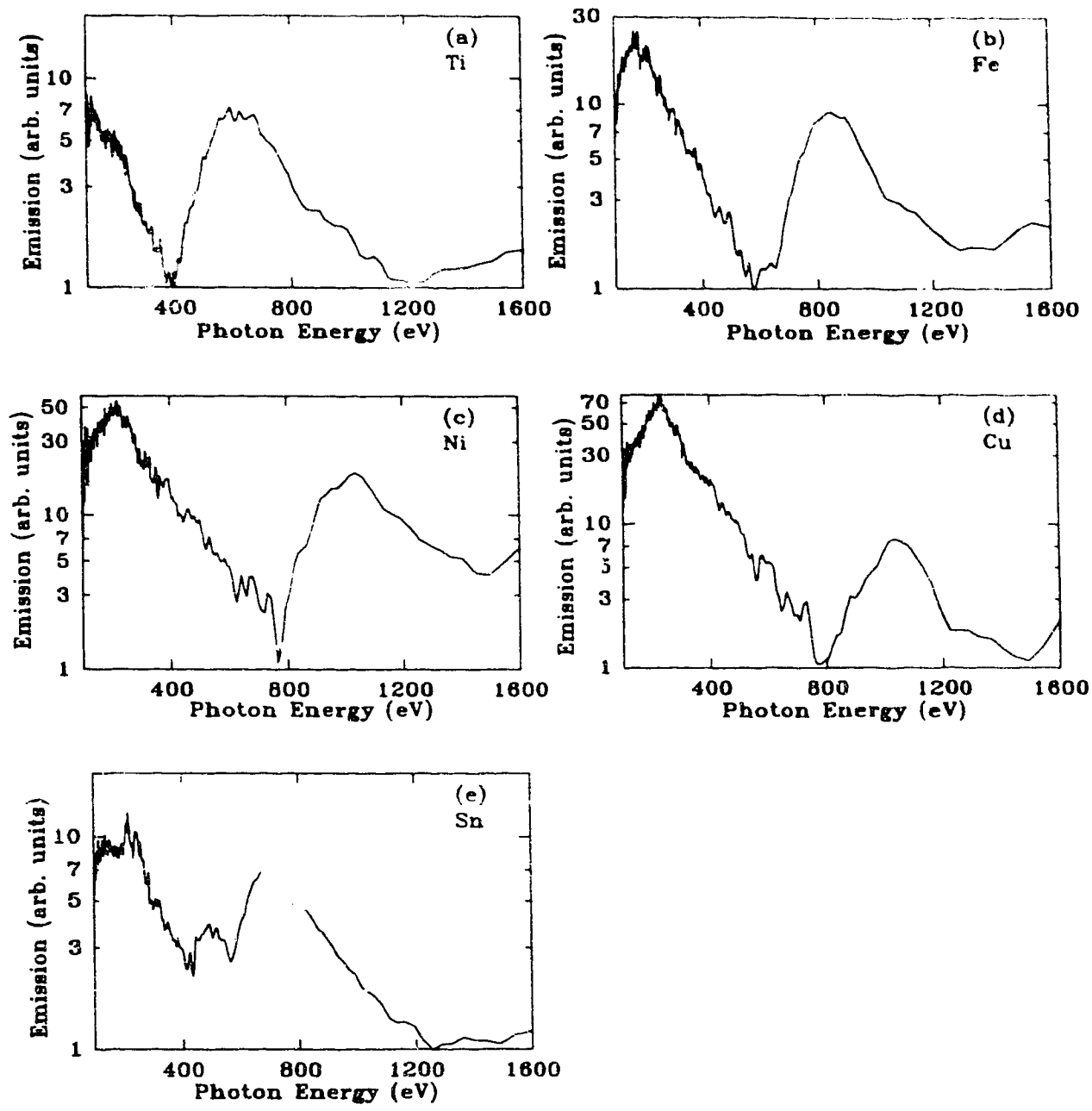


Fig. 31 Final TGS spectra in 100 - 1600 eV range obtained with 120 ps pulse at intensity $1.5 \times 10^{14} \text{ Wcm}^{-2}$. Materials are (a) Titanium, (b) Iron, (c) Nickel, (d) Copper and (e) Tin.

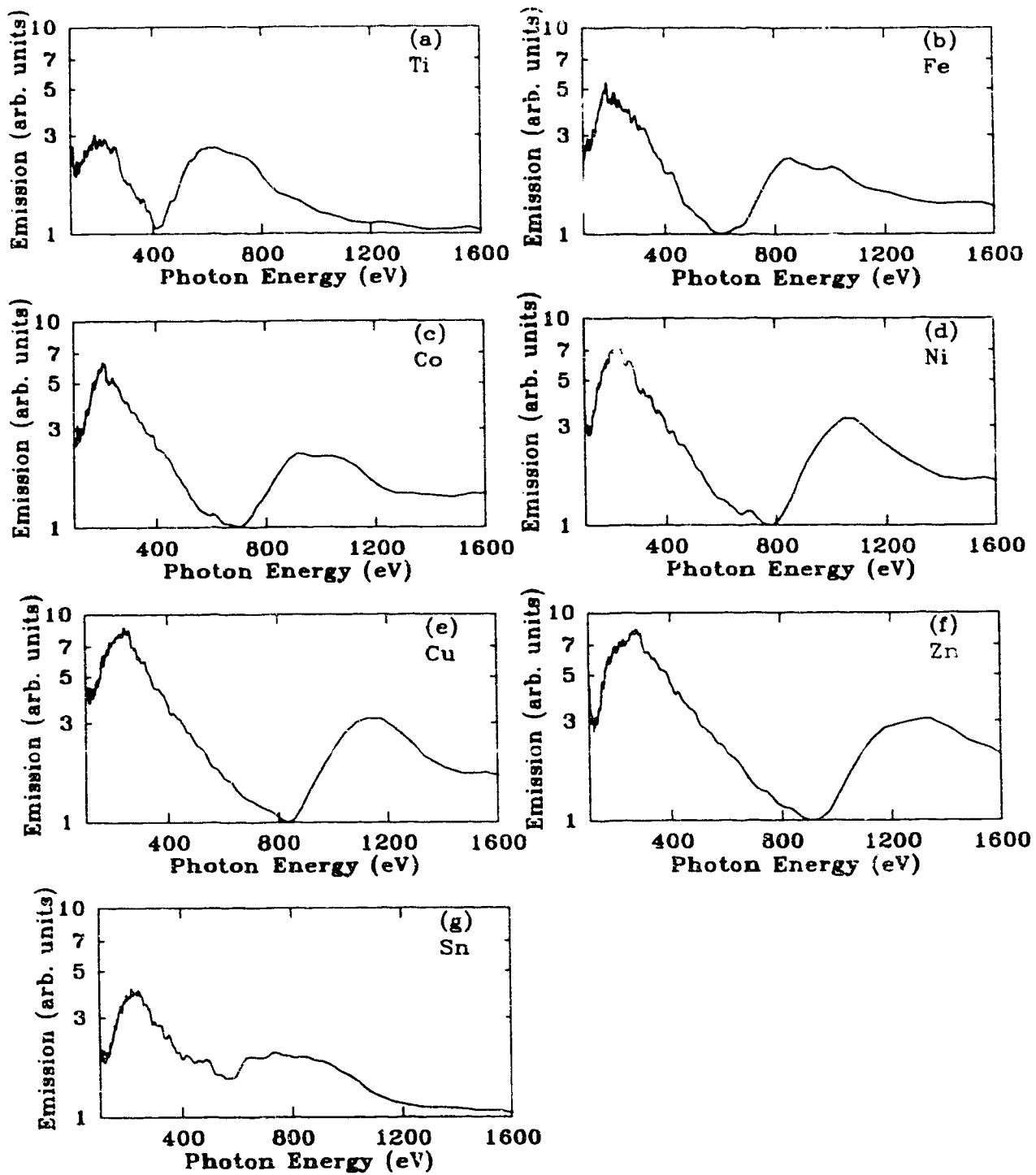


Fig. 32 Final TGS spectra in 100 - 1600 eV range obtained with 90 ps pulse at intensity $8 \times 10^{14} \text{ Wcm}^{-2}$. Materials are (a) Titanium, (b) Iron, (c) Cobalt, (d) Nickel, (e) Copper, (f) Zinc and (g) Tin.

experiments which is attributable to a hotter plasma and enhanced keV emission where the resolving power of the spectrometer drops. A hotter plasma would produce increased thermal emission in the middle energy portion of the spectrum resulting in a loss of contrast between the lower photon energy thermal and the higher photon energy line emission spectra. These spectra provide some context in terms of total x-ray emission into which the keV measurements may be placed.

When the pinhole/grating combination is replaced with a pair of pinholes and a 2B10 filter it is possible to make an estimate of the size of the keV emission zone. This experiment was performed using the 100 ps system in the low and high intensity stages and the result in both cases supports the information derived from the ray tracing code estimates of the size of the focal spot. In the low intensity experiment the plasma size was estimated to be approximately $16 \pm 3 \mu\text{m}$ and in the high intensity case the plasma size was reduced to an estimated $10 \pm 3 \mu\text{m}$. The error bounds are estimated from a measurement of the pinhole image from the edge where the exposure drops to the noise level and the inner portion where full film saturation occurs.

X-ray Yield Measurements

The absolute measurement of x-ray yield begins with the measurement of the charge from the detectors. During the low intensity experiment the signal from the *p-i-n* diodes was detected with a high speed oscilloscope and recorded using photographic film. Following the experiment the charge was integrated by videodigitizing the photographs and processing the digitized images. The technique for measuring the charge was changed for the second experiment by incorporating an integrating circuit. The charge was deposited in a capacitive integrator circuit which is monitored by a digital oscilloscope connected to a microcomputer. The integrator waveform for each detector is transferred to the computer and integrated numerically. The charge from each detector is recorded in a data file along with the laser energy for later processing. The solid

angles of the detectors are 333 μSr for the *p-i-n* diodes and 248 μSr for the GaAsP diodes. Figure 33 shows a plot of integrated charge from a *p-i-n* diode with a 9 μm Al filter as a function of total laser pulse energy on a copper target. Using the keV emission spectra recorded with the RAP crystal spectrograph the conversion efficiency for each element may be calculated according to the theory presented in the chapter on x-ray experimental techniques. Figure 34 shows the peak conversion efficiency for Ti, Fe, Co, Ni, Cu, Zn and Sn that has been measured using the 90 ps pulse and the 120 ps pulse at an energy of approximately 50 mJ. Substantial increases in the efficiency have resulted from the creation of the hotter plasmas due to the use of the triplet lens and the reduction in pulse length. It is significant that the same conversion efficiency has been achieved with tin as has been achieved with the mid Z_N targets. In principle the ideal target for M shell keV emission might be solid xenon but this presents an obvious logistical problem and tin could prove to be a valuable alternative in terms of price, availability and ease of fabrication as a target material.

It is important to note that the conversion efficiency curve in Fig. 34 is strongly influenced by the choice of the wide x-ray window (800 - 1400 eV). Figure 35 demonstrates the result of using a narrower window of 1000 - 1400 eV for the 90 ps pulses. In this case the bulk of the emission from iron is below the window edge and as a result conversion efficiency is defined as being lower. As a result of the redefinition of the x-ray window the optimum target material is now copper. The effect of shell structure which was discussed earlier is evident in Fig. 34 as the conversion efficiency is low for titanium because the bulk of its L shell emission falls below the 800 eV cutoff. The conversion efficiency is high for the mid Z_N elements with a steady drop with increasing Z_N as the neon-like populations are reduced by the increase in ionization energies. The conversion efficiency of tin is high again because it has been ionized sufficiently to bring its M shell emissions into the x-ray window.

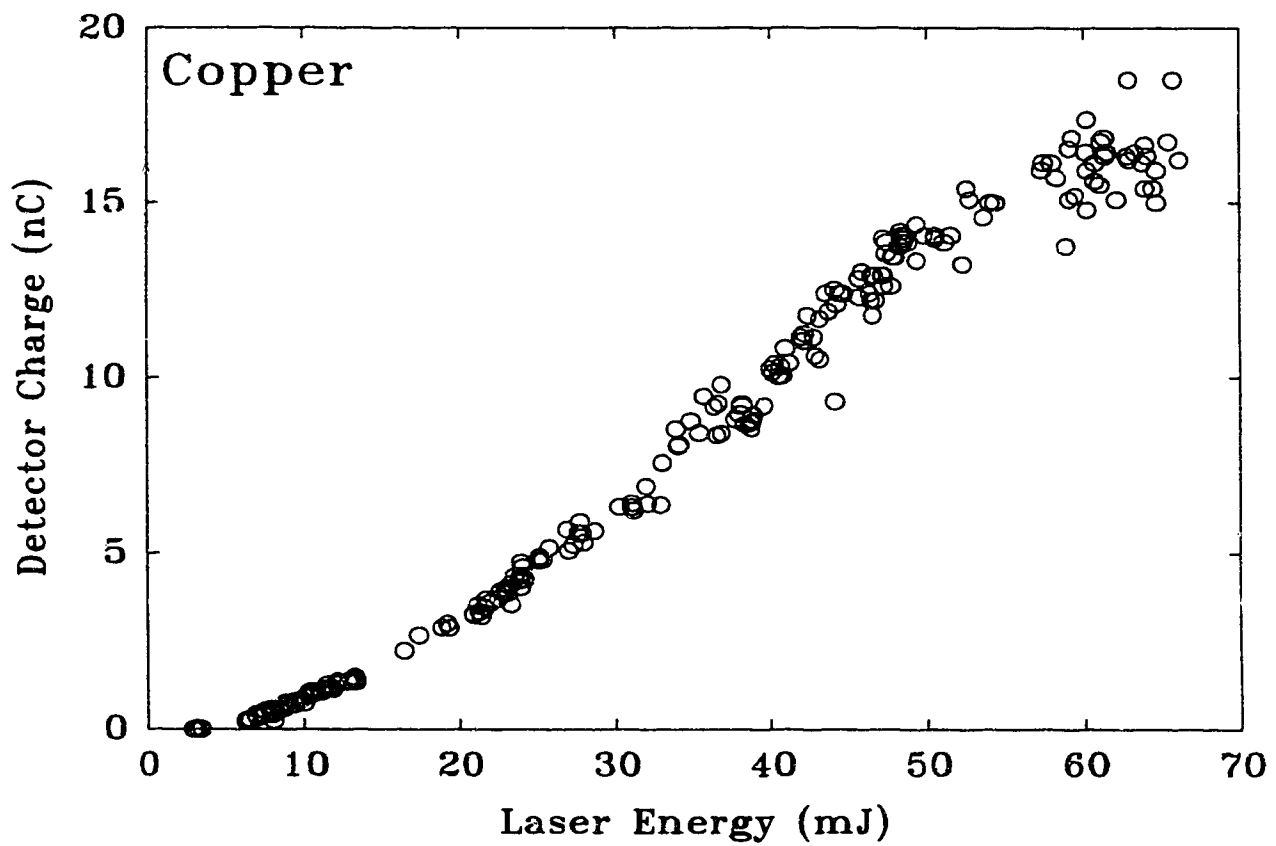


Fig. 33 Scaling of charge detected by *p-i-n* diode with 9 μm Al filter as a function of laser energy on copper target using the 90 ps pulse with the triplet focusing lens. Diode solid angle is 333 μSr .

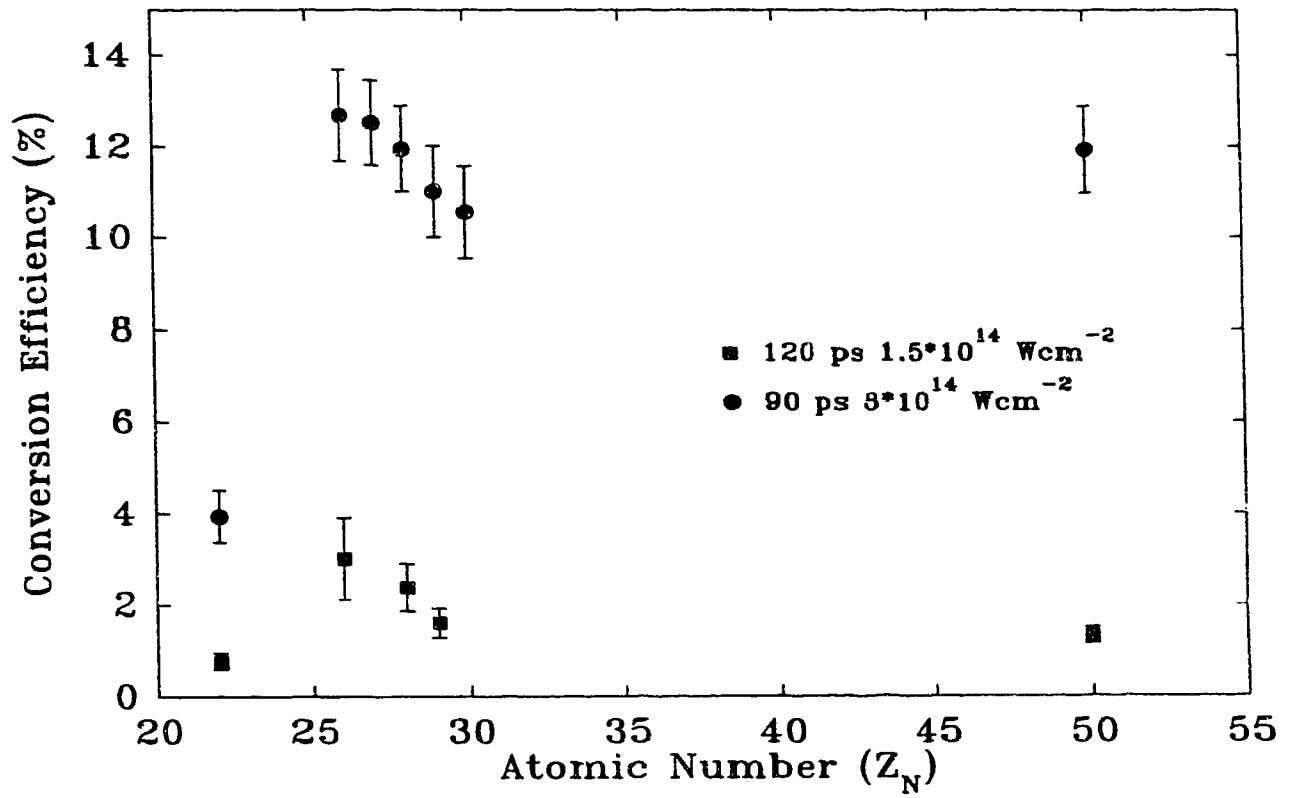


Fig. 34 Peak conversion efficiency into 800 -1400 eV x-rays in 2π Sr as a function of atomic number measured with the 90 ps pulse and the 120 ps pulse.

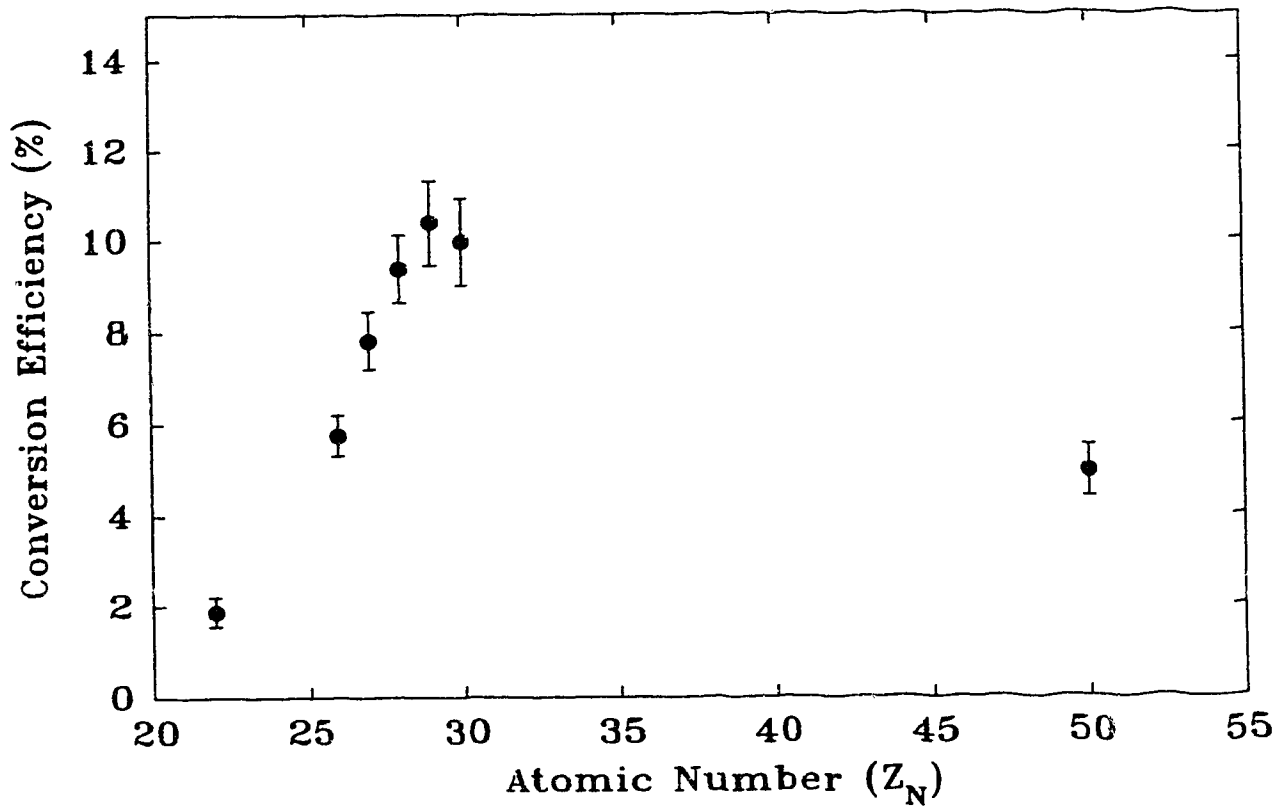


Fig. 35 Peak conversion efficiency when x-ray window is redefined to 1000 - 1400 eV.

The results from the 90 ps pulse can be compared with the maximum conversion efficiency measured with the 2 ps pulse for Ti, Fe, Ni, Cu, and Sn shown in Fig. 36. Although the structure is similar there has been a slight loss of overall conversion efficiency. This loss appears to be mostly due to a loss of energy coupling because a substantial fraction of the laser light is being reflected by the plasma as the scale length decreases with pulse length and the density gradients become steeper. The measured values of plasma reflectivity will be presented in a later section. Finally, Fig. 37 shows the contrast between typical peak conversion efficiencies for copper using the 90 ps, 2 ps and 850 fs pulses with energies in the range of 50 mJ, 40 mJ and 35 mJ respectively. In the case of the 850 fs pulse there has been a much larger loss of conversion efficiency than was observed for the transition from 90 ps to 2 ps. Unlike the 2 ps case the measured reflection does not appear to account completely for the loss in conversion efficiency leading to the need for other explanations such as ionization rate limitations and possible focusing degradation due to self-focusing in the triplet lens.

The scaling of conversion efficiency with pulse energy on target for the 90 ps pulse is shown in Figs. 38a and 38b for copper. The main effect, of course, is the increase in conversion efficiency with the increase in intensity. However, there are two additional effects which can be observed in this figure. The first is a threshold near 3 - 5 mJ corresponding approximately to $6 \times 10^{13} \text{ Wcm}^{-2}$ in intensity. This threshold represents the intensity where significant neon-like populations are being formed. In the low intensity region a power law fit to the data yields a scaling of $E^{2.38}$ dependence on laser pulse energy. Note that comparison of intensities between these experiments and the results of other groups is complicated by the small size of the focal spot leading to two dimensional effects. These effects will be discussed further in the next chapter. A second interesting feature of the energy scaling curve is the rollover in the high pulse energy regime. This is due to two effects which arise in the high energy range of

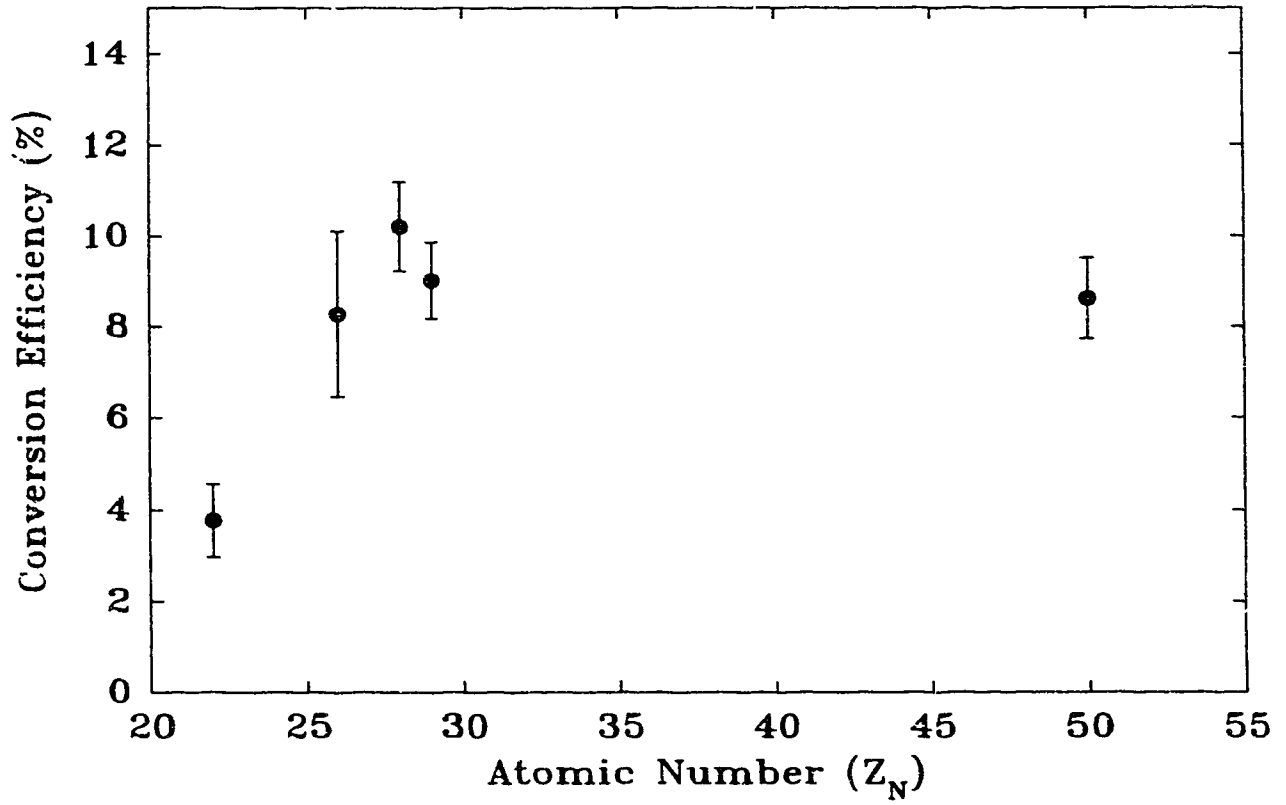


Fig. 36 Conversion efficiency into 800-1400 eV x-rays from 2 ps pulse as a function of atomic number.

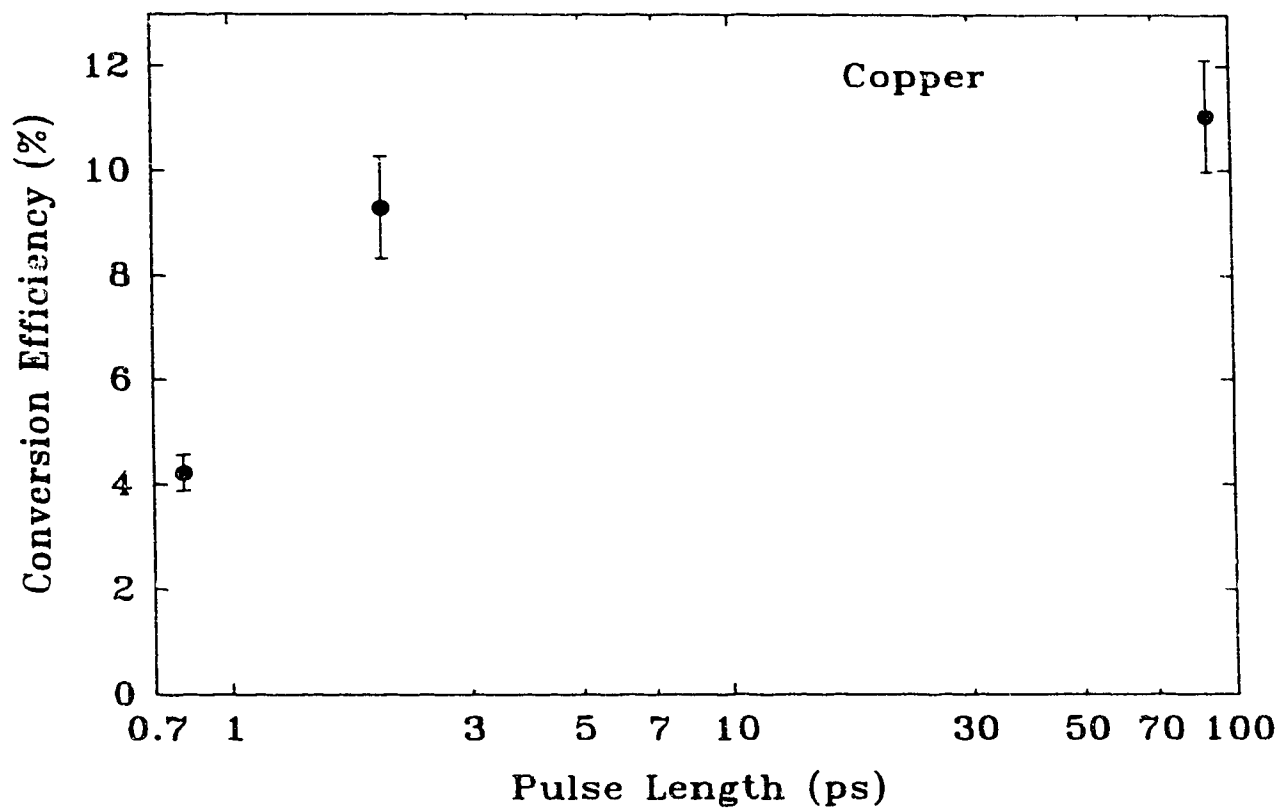


Fig. 37 Conversion efficiency for copper measured at 850 fs, 2 ps and 90 ps.

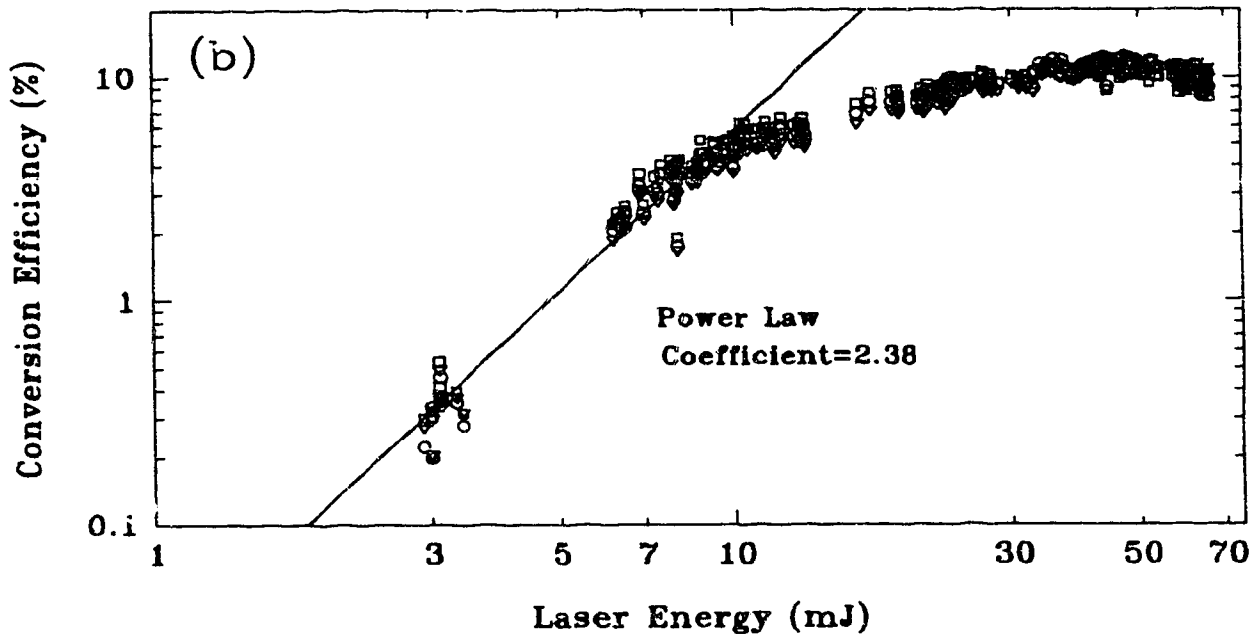
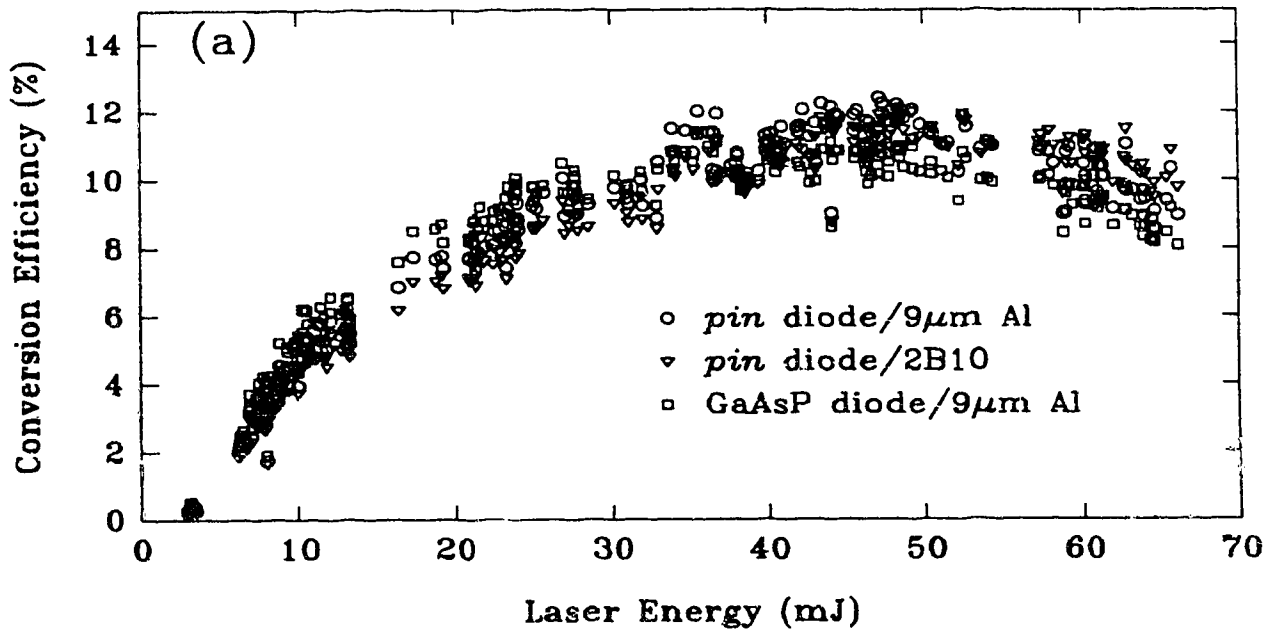


Fig. 38 Conversion efficiency for copper as a function of laser pulse energy measured using 90 ps pulses. (a) Conversion efficiency data on linear scale showing rollover in high energy end. (b) Same data on log-log scale showing drop off and scaling in low energy end.

operation of the KrF amplifier. In the regime where the highest pulse energies are obtained (fresh laser gas/high gain regime) the fraction of ASE often exceeds 10% during the earliest shots. This energy contributes to the measured total pulse energy but does not contribute to x-ray generation and therefore reduces the conversion efficiency by its fractional contribution. The second effect of the ASE is the production of a preformed plasma with which the main pulse interacts. If this plasma is sufficiently large a noticeable fraction of the energy of the main pulse will be absorbed farther from the target surface than in the lower ASE regimes and the energy of the main pulse will couple less effectively to the high density plasma where the heat is needed to generate the high conversion efficiencies. This rollover behaviour is seen with all materials and in all pulse length regimes including the low intensity experiments with the 120 ps pulse.

ASE Dependence

The amplified spontaneous emission (ASE) which accompanies the main pulse comes (effectively) from two sources. Single pass ASE refers to ASE which passes through the amplifier only once before emerging in the direction of the target chamber. Single pass ASE is highly divergent and contributes negligibly to the measured laser energy on target. ASE which follows the same path as the main pulse during both of its passes through the amplifier is two-pass ASE. The ASE which passes through the spatial filter is the portion that can contribute significantly to the total pulse energy. As a result of traveling through the spatial filter this ASE has the same order of magnitude divergence as the main pulse and can be focused to significant intensities. The 2 pass ASE energy has been measured as a fraction of the total pulse energy for the 90 ps system and generally starts near 12% and falls steadily until it stabilizes at approximately 5-6%. The fraction of this which actually precedes the main pulse is roughly 15% corresponding to the timing of the main pulse which normally occurs 5 - 6 nsec into the ASE pulse. The peak prepulse intensity can be estimated from the measured ASE

divergence of 200 μRad to be approximately $1 - 5 \times 10^{10} \text{ Wcm}^{-2}$. This is well above the generally accepted threshold intensity for plasma generation of 10^8 Wcm^{-2} so it can be assumed that there will be a preformed plasma at all times.

Quantitative measurements of the dependence of the x-ray emission on the prepulse ASE proved to be difficult. This is due to the fact that the high gain regime is short lived and the ASE levels cannot be "controlled". However, experiments were undertaken in order to try and understand the effects of the ASE and those results are presented here. Measuring ASE levels is problematic with this particular laser system because they must be measured on a shot to shot basis since the combination of gas lifetime, trigger jitter and low repetition rate results in ASE conditions which vary from shot to shot. The technique used to measure the ASE was to allow the main pulse to saturate a high speed semiconductor photodiode with a saturated voltage of 45 V. This allowed oscilloscope recording of the ASE pulseshape with 1 nsec resolution while avoiding damage to the high speed oscilloscope. The energy as measured by the photodiode was calibrated against a calorimeter. Figure 39 shows the results of an ASE experimental run. The energy of the laser pulse decreases with each shot as the gas becomes slightly more contaminated and the gain is reduced. The trend of the increase in conversion efficiency with decreasing total laser energy is fairly clear. The ASE fraction starts at 10% and decreases to 5% over the course of the run and this accounts for some of the trend in the conversion efficiency because it contributes to the total energy measurement but not to x-ray generation. However, once the energy measurement is corrected to subtract the ASE (as shown in Fig. 39b) the trend is still visible in the data although it is weaker. Kodama et al.⁷¹ and Tanaka et al.⁷² have examined the effect of preformed plasmas on x-ray production using large laser systems and have found that short scale length preformed plasmas enhance x-ray production for UV pulses but if the preformed plasma becomes too large then x-ray generation becomes slightly suppressed. This is supported by the data shown in Fig. 39b. Even after the ASE has been factored

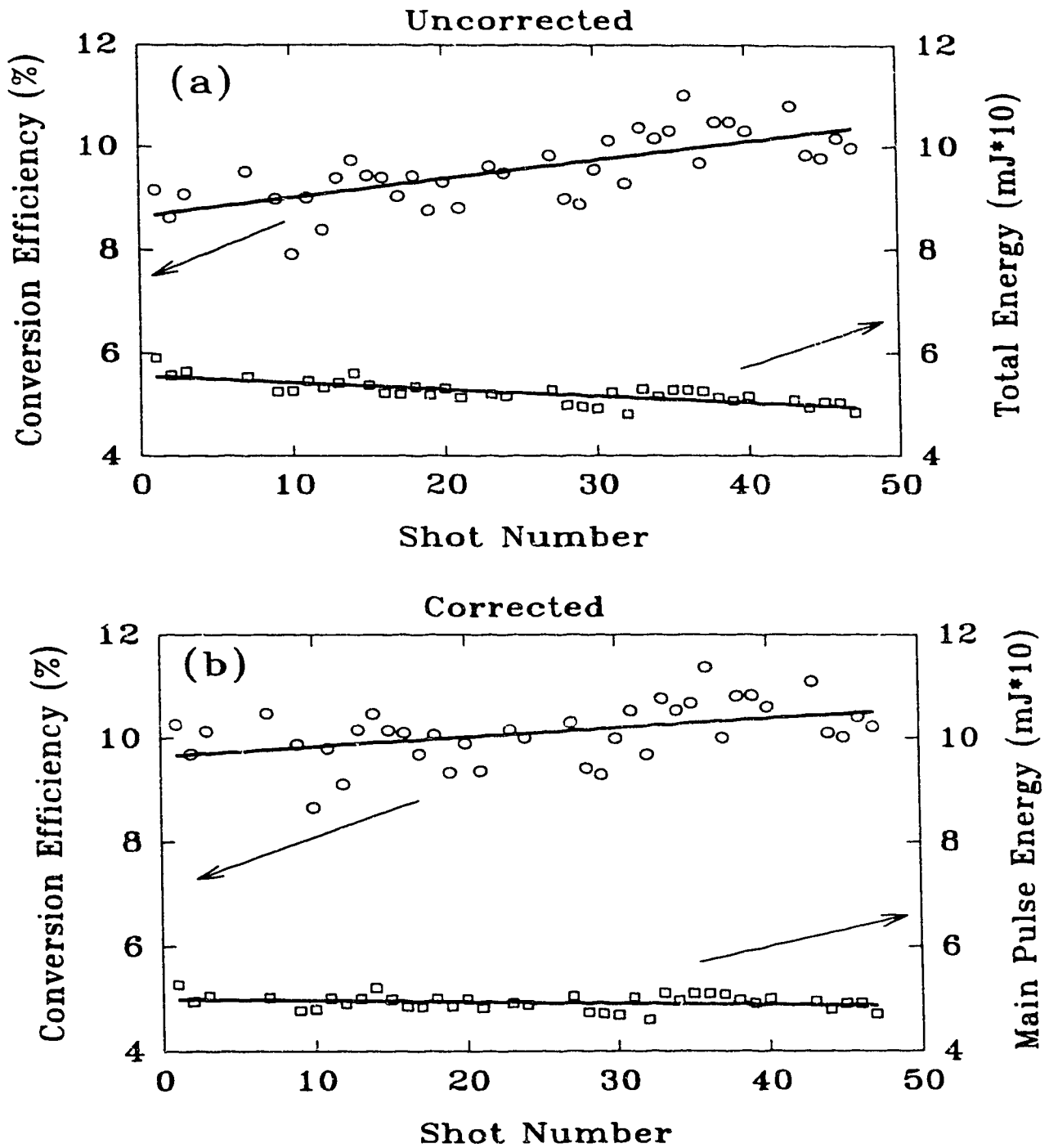


Fig. 39 Effect of ASE on conversion efficiency. (a) Data not corrected to subtract ASE effect. (b) Data corrected to subtract ASE still shows trend of increasing conversion efficiency with slowly decreasing main pulse energy.

out of the data the conversion efficiency increases while the pulse energy decreases slightly. It is expected that the ASE on target is above the threshold for plasma formation at all times and therefore x-ray generation is enhanced above the level that would be seen if the prepulse were eliminated completely. However, because the ASE starts at least 5 nsec before the main pulse an extended cold underdense coronal plasma is created through which the main pulse must burn to get to the higher density plasma at the target surface.

In addition to the ASE intensity experiment the dependence on timing was studied by delaying the injection of the KrF amplifier by up to 7.5 nsec on top of the basic 5 - 6 nsec delay. In this experiment no evidence was found to indicate any dependence on the time at which the main pulse arrived. This is not surprising since the plasma should evolve into a steady state three dimensional expansion due to the relatively long duration of the prepulse. This would seem to indicate that the dependence is not on the volume of plasma generated by the prepulse but on the density scale length of the prepulse plasma which would vary with the intensity of the prepulse.

Angular Dependence

The angular dependence of the keV x-ray emission has been measured in order to test the assumptions made in calculating the yields. The x-ray yields have been calculated under the assumption of an isotropic angular distribution. The yield measurements were made at an angle of 60° in order to minimize the error resulting from nonisotropic distributions. The measurement of angular dependence of keV x-ray emission was made by using two *p-i-n* diodes with $9\mu\text{m}$ aluminum filters. One diode was held in the normal fixed position at 60° off target normal. The other diode was moved through a series of viewing angles from 85° to 30° . The measured emissions were normalized against the fixed diode at 60° . Figure 40 shows the measured angular dependence for the three pulse length regimes. The measurements have been fit to the

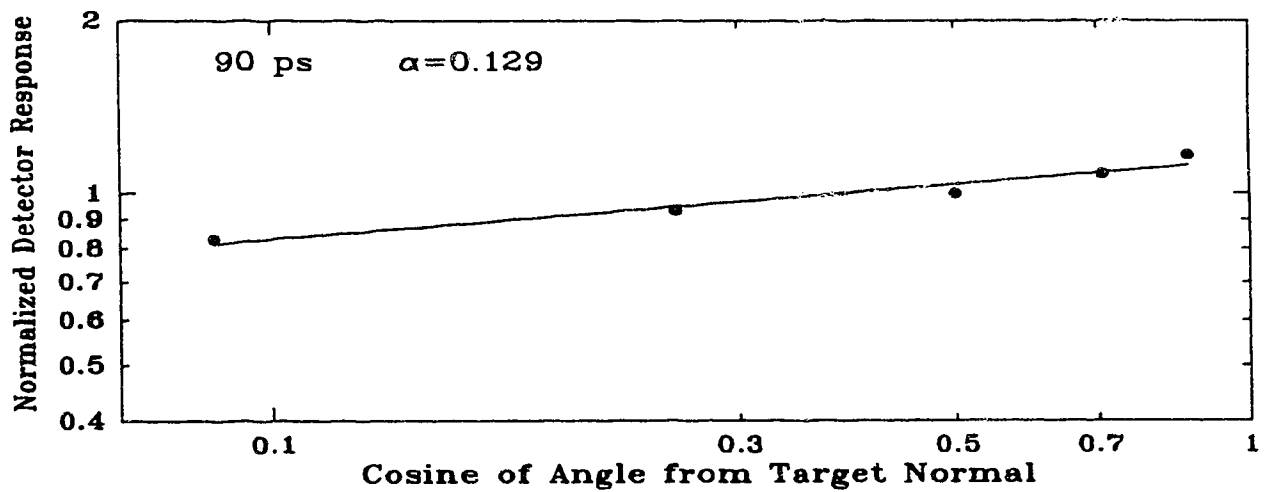
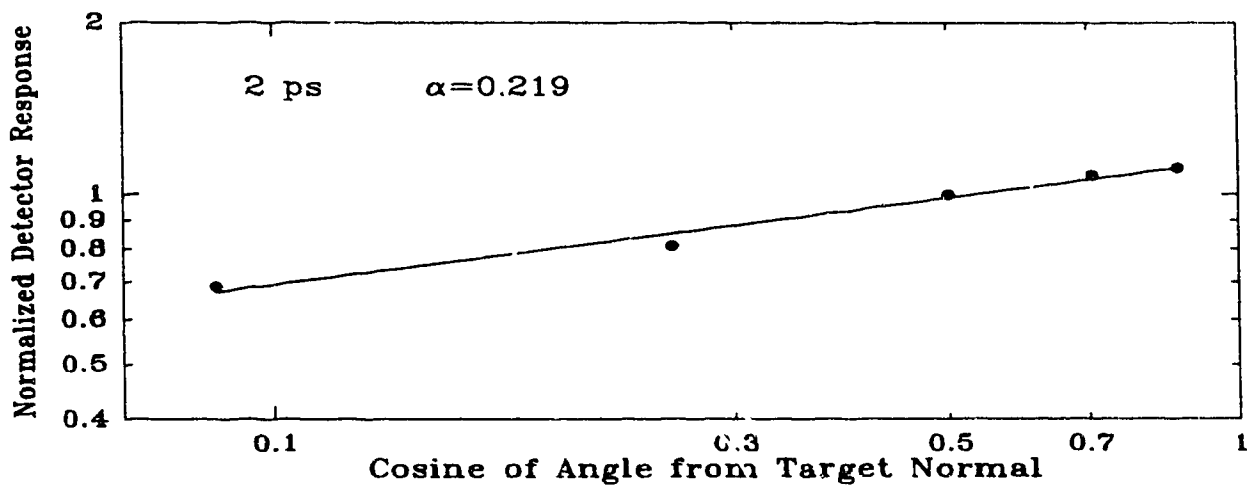
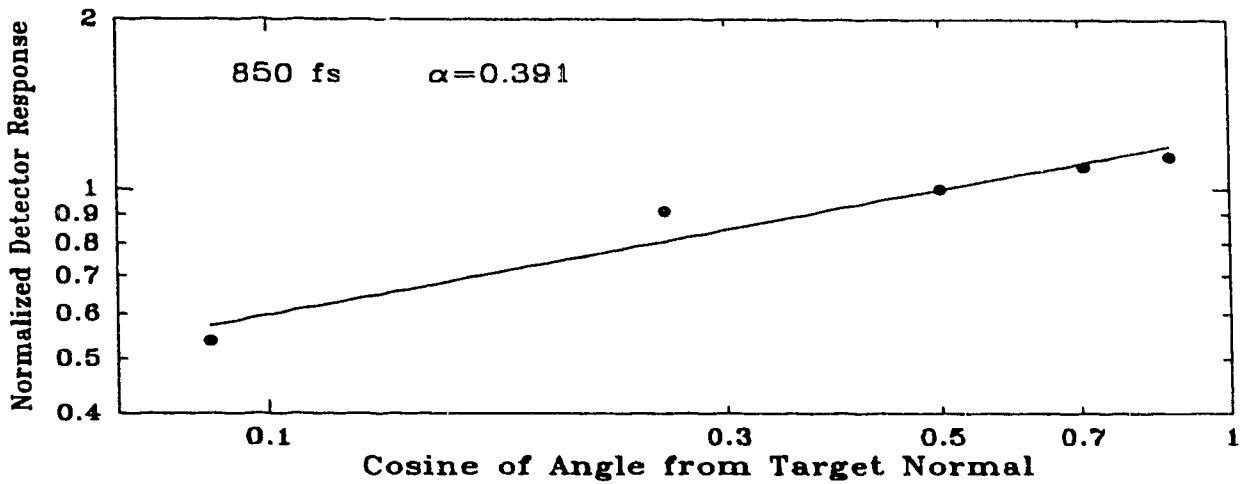


Fig. 40 Angular dependence of emission for (a) 850 fs pulse, (b) 2 ps pulse and (c) 90 ps pulse. The estimated $\cos^\alpha(\theta)$ coefficient is listed in each figure.

assumed $\cos^\alpha(\theta)$ dependence by the least squares method and the fit in all cases is satisfactory with no major discrepancy. These results support the assumption of the $\cos^\alpha(\theta)$ angular dependence and more importantly indicate that the combination of the assumption of isotropic emission and the 60° observation angle results in minimal error in the calculation of the yields. Note that the α parameter increases with decreasing pulse length which may be associated with the decreasing thickness and increasing density of the emitting plasma leading to opacity effects.

Plasma Reflectivity

In order to obtain a basic estimate of the coupling efficiency between the laser and the plasma the reflectivity of the plasma in the 3 different pulse length regimes has been measured in the specular direction. To make this measurement the target was moved to provide an angle of incidence of approximately 17° with respect to target normal. The polarization was tested and verified to be S polarized (perpendicular to the plane of incidence) in order to most closely simulate normal incidence conditions. A pyroelectric calorimeter was positioned with a collection angle of F/1.7 to intercept the specularly reflected beam and a thin quartz plate was mounted on the front of the calorimeter to block all other emission from the plasma. Figure 41 shows the dependence of the measured specular reflectivity on pulse length. This figure clearly shows a decrease in the reflected portion as the pulse length increases with almost complete absorption occurring for the 90 ps pulse. Specular reflectivity represents a base estimate for losses due to reflection since it is likely that there will also be scattering into nonspecular directions. Plasma reflectivity is undesirable in terms of maximizing keV x-ray conversion efficiency since it represents a substantial fraction of the laser energy being wasted. The ~20-25% specular reflectivity in the case of the 2 ps plasma accounts for most of the loss of conversion efficiency that was observed in the x-ray

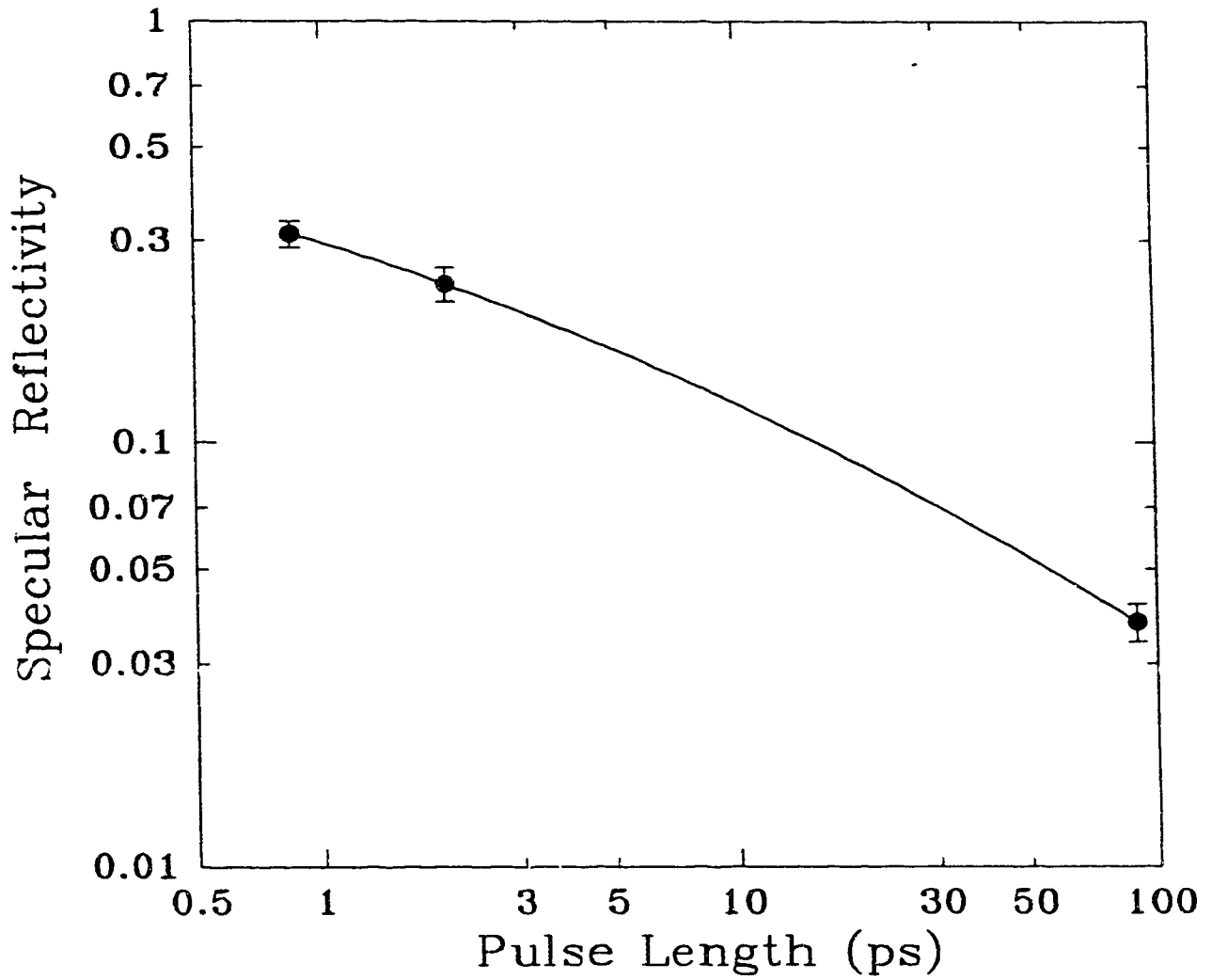


Fig. 41 Measured specular reflectivity of plasma as a function of pulse length.

The curve is drawn only to guide the eye through the data.

measurements. However, the ~30% reflectivity of the 850 fs pulse is not enough to account for the drop in conversion efficiency by a factor of 2. Fedosejevs et al.⁷³ have measured specular and nonspecular reflectivity from plasmas generated using 250 fs KrF laser pulses at intensities between 10^{14} Wcm^{-2} and 10^{15} Wcm^{-2} . They have observed specular reflectivities of 55% at 10^{14} Wcm^{-2} decreasing to 40% at 10^{15} Wcm^{-2} . They have also observed that nonspecular reflection increases from less than 10% to near 20% of the total reflected light for the same intensities respectively. On this basis it is reasonable to expect that the combination of specular and nonspecular reflection will not be able to account for all of the reduction in keV emission in the 850 fs case. This clearly indicates that there are other processes which are beginning to affect the x-ray generation. In addition to possible increases in nonspecular reflection the ionization dynamics are likely playing a role in the reduction of the keV emission.

X-Ray Yields in Helium Background

In addition to the bulk of the measurements of keV emission which were conducted under vacuum conditions some measurements were made using atmospheric helium as a background gas. This is an interesting case because x-ray lithography processes may be simplified considerably if the need for evacuated chambers can be eliminated or at least minimized. Figure 42a shows the effect of the presence of helium on the charge yield as measured by the *p-i-n* diode with a $9\mu\text{m}$ Al filter. Figure 42b shows the conversion efficiency with and without helium background where the spectrally integrated transmission of the helium has been accounted for. The integrated transmission for the keV spectrum of copper through the 26.5 cm path length of helium is calculated to be approximately 86% assuming $158.5 \mu\text{g cm}^{-3}$ of helium (appropriate for atmospheric pressure of 700 Torr in Edmonton). The data shows that the presence of the helium results in approximately 15% suppression of overall conversion efficiency (at the plasma). However, in terms of system development this may be a small price to pay

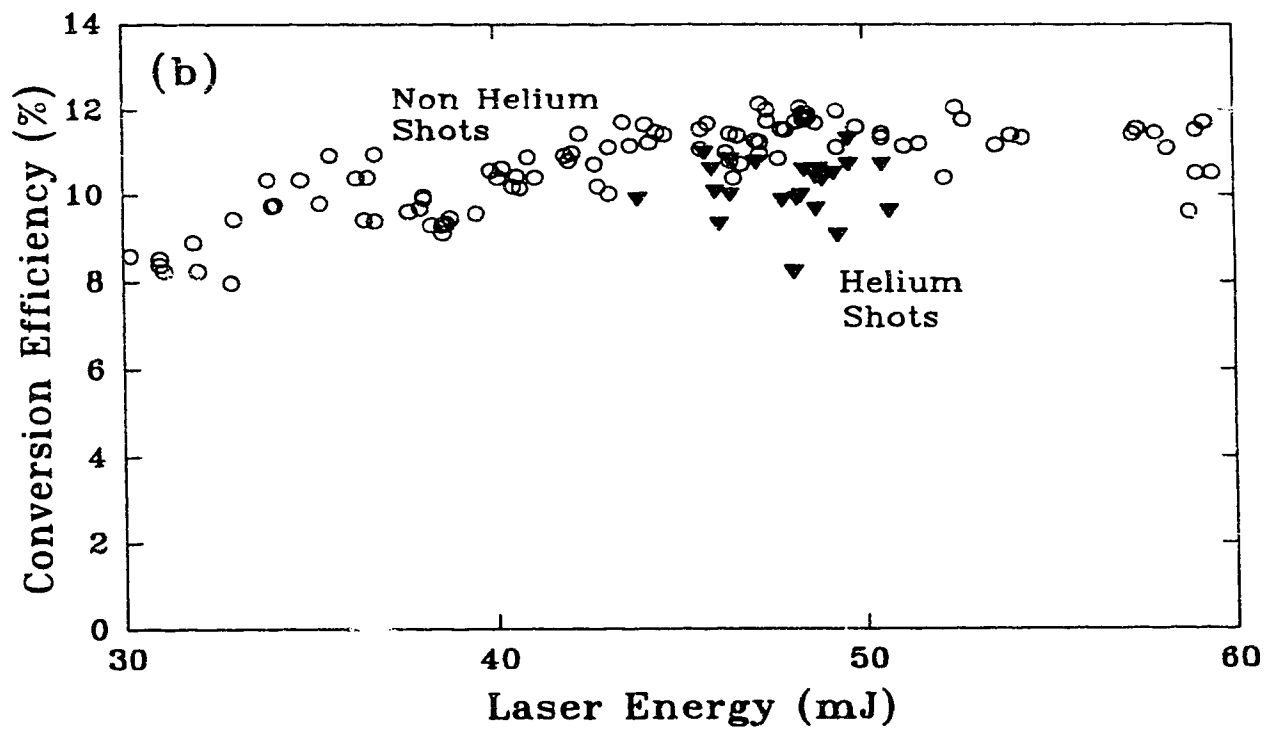
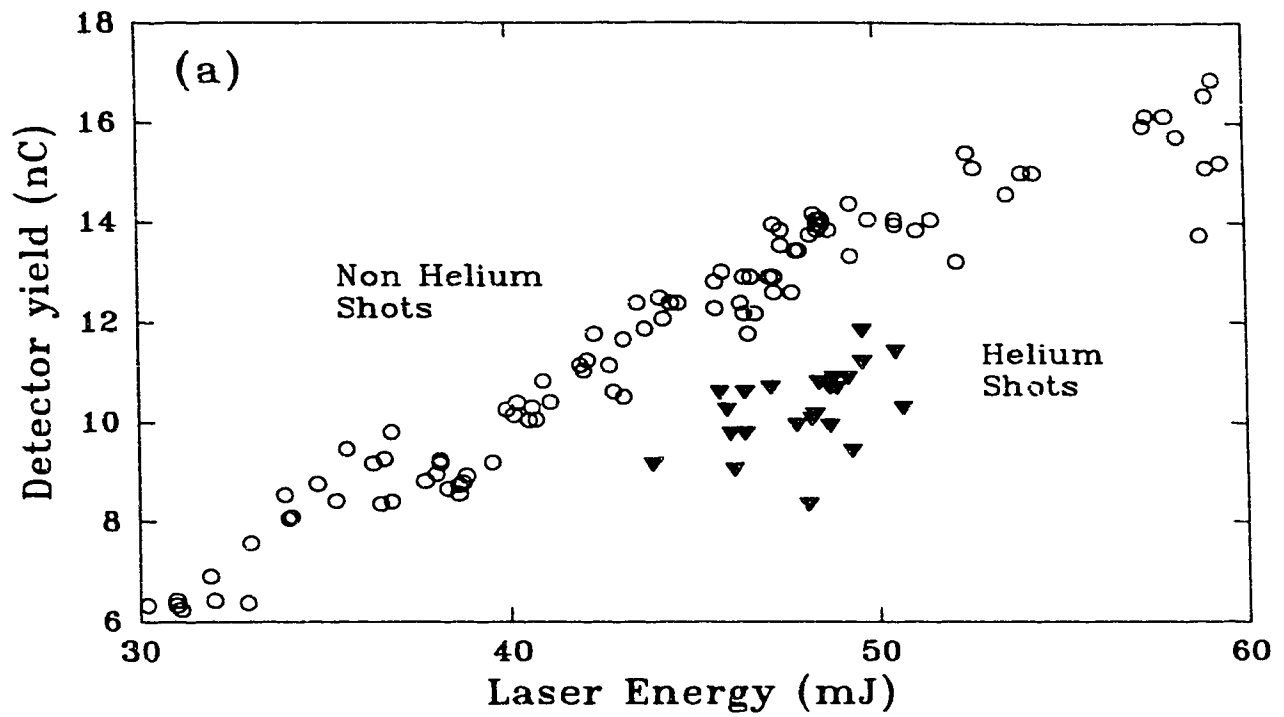


Fig. 42 Effect of helium on conversion efficiency for copper as measured with the *p-i-n* diode with $9\mu\text{m}$ Al filter. (a) shows charge detected as a function of energy. (b) shows x-ray conversion efficiency when corrected for helium absorption.

in order to afford the benefits of the presence of a background gas. One additional major potential benefit of working with a background gas is the suppression of target debris as the presence of the gas slows material blasted from the target.

DISCUSSION

Simulations of some of the experimental conditions have been run using the one dimensional Lagrangian hydrocode MEDUSA⁷⁴ in an effort to better understand some of the underlying processes which have lead to the x-ray conversion efficiencies observed. The MEDUSA simulations are run using a flux limiter value of 0.6. The material is aluminum but it is expected that the results will be reasonably general and provide valuable information on plasma conditions and behaviour during the interaction with the laser. Of primary interest is the estimation of temperature and density in the regions where the x-ray emission occurs. In addition to the MEDUSA simulations, some comparison has been made to an analytic self-regulating model⁷⁵. In addition, an effort has been made to identify the main characteristics of the preformed plasma using an extension of the analytic model for spherically divergent plasmas.

Figures 43a and 43b show MEDUSA simulation results depicting the detailed structure of the plasma at the peak of the laser pulse for a 100 ps gaussian pulse at intensities of 10^{14} Wcm^{-2} and 10^{15} Wcm^{-2} respectively. In this simulation the target starts as a solid slab at $x=30 \mu\text{m}$ at time equal zero with the peak of the laser pulse occurring 150 ps later. The figures show the spatial profiles of the electron temperature (in eV) and the electron density (in units of critical density) as well as the plasma radiation (in $10^5 \text{ W}\mu\text{m}^{-3}$) as calculated⁷⁶ by MEDUSA. The shock wave structure in front of the ablation zone may be seen quite clearly in the diagrams where the electron density is strongly peaked in a layer approximately $1 \mu\text{m}$ thick and reaches values between 10 and 60 times critical density (note that Z is artificially set to 2 in the cold material). The temperature profiles begin at room temperature in the cold target material and rise rapidly at the leading edge of the shock wave to a value of 10 eV. The temperature again rises rapidly at the leading edge of the ablation front and this is where the initial ionization occurs. The temperature continues to rise out to the critical density

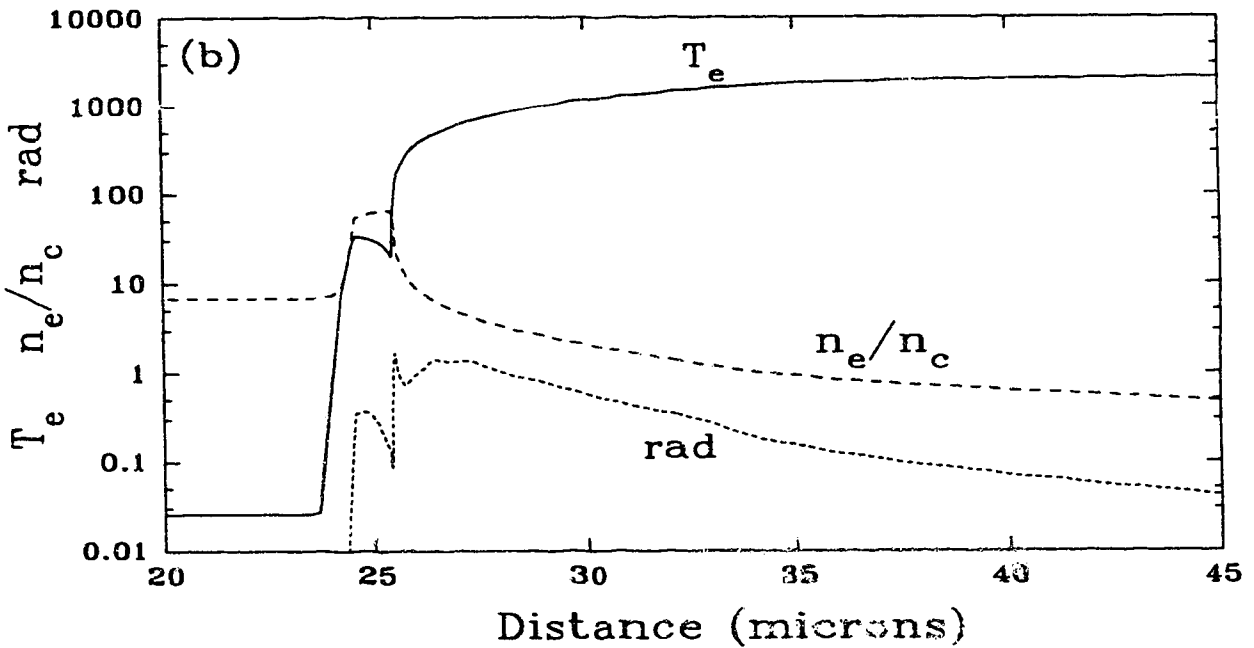
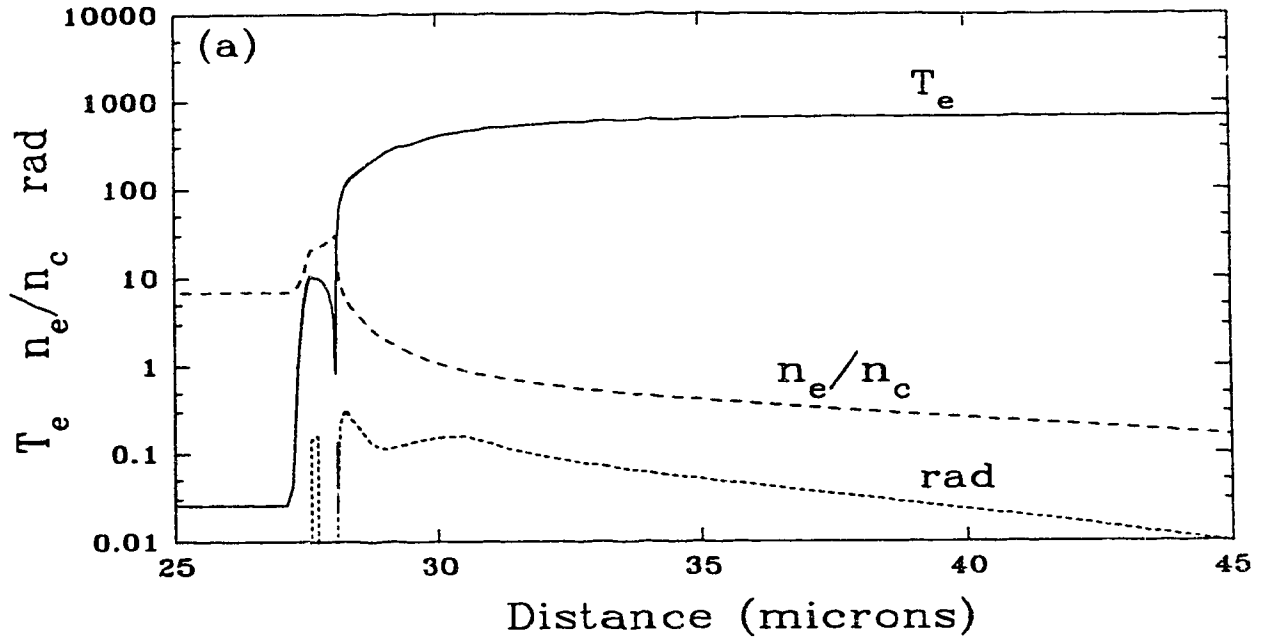


Fig. 43 MEDUSA simulation results for a 100 ps $K\alpha$ laser pulse showing spatial profiles of electron temperature (T_e in eV), electron density in terms of critical density (n_e/n_c) and the radiation from the plasma (rad) in units of $10^5 \text{ W}\mu\text{m}^{-3}$. The profiles are those occurring at the peak of the laser where peak intensity is (a) 10^{14} Wcm^2 and (b) 10^{15} Wcm^2 .

region where it begins to approach an asymptotic value which is maintained well out into the corona. The radiation profile is the radiated power per unit volume as calculated by MEDUSA. Note that the dip in temperature at the trailing edge of the shock wave is not believed to be real but is likely an artifact of the equation of state.

The radiation profiles in Fig. 43 may be observed to have a multiply peaked structure. This corresponds to different regions (plasma conditions) producing the different types of radiation as discussed in the chapter on x-ray emission (bremsstrahlung, recombination and bound-bound). The dominant region of emission for each type of radiation can be determined from the dependence on density, temperature and ionization predicted by MEDUSA. The bremsstrahlung scaling profile (recall Eqn. 7) is calculated as:

$$P_B \propto n_e n_i Z^2 T^{1/2} \quad (23)$$

where n_e and n_i are calculated from the mass density (ρ) and the average ion charge Z .

The profile for the free-bound (recombination) emission from He and H-like ions (which will provide the bulk of the continuum radiation observed in the experimental keV spectra) is calculated as (also from Eqn. 7):

$$P_{fb} \propto n_e n_i f(Z-10) Z^2 T_e^{-1/2} \quad (24)$$

where the function $f(Z-10)$ provides an estimate of the fraction of ions which are ionized to H and He-like states together and is defined by $f(Z-10)=0$ for $Z<10$, $f(Z-10)=Z-10$ for $10 \leq Z \leq 11$ and $f(Z-10)=1$ for $Z>11$. The collisional excitation rate for bound electrons in helium-like and hydrogen-like ions provides the scaling profile for line emission and is estimated as (refer to Eqn. 8):

$$P_L \propto n_e n_i f(Z-10) T_e^{-1/2} \exp(-1600 / T_e) \quad (25)$$

where 1600 eV is the dominant line emission energy in the aluminum spectrum. Note these are not rigorous calculations of emission from aluminum plasmas but are simple estimates to characterize the origin of the structure of the emission profile generated by MEDUSA. Figure 44 shows the radiation emission profile from Fig. 43b in more detail

along with the individual scaling profiles (arbitrary vertical units are used to clarify the structure) of the different types of radiation based on the densities, temperatures and ionization states as calculated by MEDUSA. The results show that there is a fairly clear separation of zones in which particular types of radiation occur. From the comparison of the MEDUSA profile and the individual scaling profiles it may be seen that bremsstrahlung is generated deep inside the plasma in the shock front region largely as a result of the high densities generated in this zone. However, it must be noted that while this is the region where the bulk of the bremsstrahlung is generated, bremsstrahlung actually makes only a small contribution to the total radiation because of the cold plasma temperature in this region. The recombination radiation profile for He and H-like ions peaks at the ablation front where the temperature rises and the ionization has reached a level where there are significant numbers of these ions. At this point the temperature has not risen to a level where recombination would be suppressed by a lack of low energy electrons (those most likely to recombine). Comparing to Fig. 43b the line emission profile can be seen to peak in a region of overdense plasma ($4-7n_c$) where the temperature ranges from 500 eV to 700 eV. According to the MEDUSA simulations this is the region of the plasma where the keV emission originates. Similar structure may be observed in the radiation profile in Fig. 43a with the exception that the keV emission zone has shifted to a lower density region and is reduced in height relative to the recombination radiation peak. This difference between the two profiles corresponds to the increased conversion efficiency observed experimentally in the 100 ps regime when the intensity was increased from $1.5 \times 10^{14} \text{ Wcm}^{-2}$ to $8 \times 10^{14} \text{ Wcm}^{-2}$.

The conclusion reached from the behaviour of the scaling profiles in Fig. 44 and the profiles in Figs. 43a and 43b is that there are two separate regions contributing two different types of radiation to the emission from the plasma. True bremsstrahlung is not expected to be a significantly contributing source leaving recombination and line

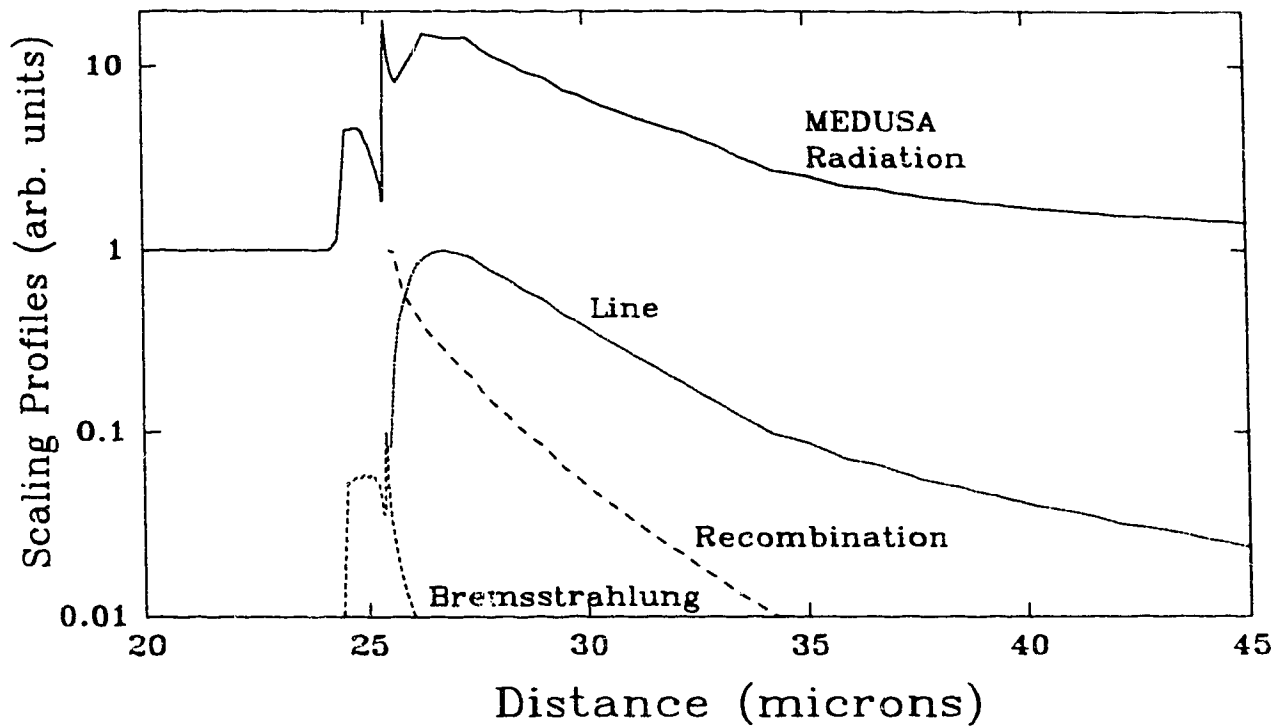


Fig. 44 Sources of radiation from the MEDUSA simulated plasma. Shows the scaling of the factors for bremsstrahlung, recombination and line radiation for the plasma conditions in Fig 43b. The vertical scaling is arbitrary in order to highlight the structural comparison to the MEDUSA prediction for radiation.

radiation dominating the spectrum. The continuum radiation is primarily generated deep inside the plasma near the ablation front from recombining He-like atoms at high densities and cooler temperatures (compared to the coronal temperatures). The line radiation originates in a less dense region closer to the critical density but higher in temperature. This observation is supported by the results of calculations and experiments done by Alaterre et al.²⁹ where plasma emission characteristics were best reproduced by using a two-temperature model where the cooler temperatures corresponded to the continuum radiation from higher densities (4-5 times critical) and the higher temperatures correspond to radiation from lower densities near critical density. The experiments to which they were comparing were 450 ps, 260 nm pulses in the 10^{14} Wcm^{-2} regime. Simulations using MEDUSA with a 1 ns pulse length at 10^{14} Wcm^{-2} further support this description of the origins of the radiation. Experimental verification of this description would require specialized experiments using layered targets with different atomic materials as markers.

Experimental estimates of the temperature of the plasma from the continuum emission from titanium and tin at the high ends of the keV spectra recorded on film have yielded results of 170 ± 30 eV for the 120 ps pulse experiments (1.5×10^{14} Wcm^{-2}). Similar estimates for the 90 ps pulse experiments (8×10^{14} Wcm^{-2}) indicate higher temperatures in the range of 230 ± 20 eV. The results from the 2 ps experiments are more scattered and range from 230 eV to 330 eV but some increase in temperature is indicated by the spectra. No estimate can be made for the 850 fs pulse because titanium and tin were not used with this pulse length and these two elements are the principal species used in making continuum emission estimates as their shell emission is concentrated at the low end of the measured range. As indicated above, the temperatures which are estimated from the continuum at the high ends of the keV spectra are expected to originate with the recombination radiation emanating from the high density leading edge of the ablation zone. The estimates of temperature appear to agree with the values

predicted by MEDUSA in this region. However, it is difficult to say with any certainty because of the extremely steep temperature gradients in the region which result in a wide variety of temperatures occurring in a small area. Also, the experimental measurements integrate radiation in time which includes late time radiation from the cooling plasma.

Figures 45a and 45b show MEDUSA simulations in the 1 ps and 10 ps pulse length regimes at intensities of 10^{16} Wcm^{-2} when the laser is at its peak. The diagrams show a progressive merging of the ablation front (nonlinear heat wave) into the shock front as the pulse length is reduced. Also visible is a trend of the peak keV emission zone moving into higher density regions ($>10n_c$) as the entire length of the interaction region is reduced. In the 10 ps simulation the x-ray emission levels appear to be somewhat higher than in either the 100 ps or the 1 ps case corresponding to the transition of the keV emission zone to higher densities. The MEDUSA simulations at 10^{16} Wcm^{-2} have been chosen for comparison because at higher intensities the simulation starts to produce some anomalous behaviour in the deposition of energy at the critical density.

One of the important issues which must be addressed in attempting to relate a simulation of laser plasma interaction with aluminum to that which occurs with higher atomic number species is the time required to reach the desired ionization states. Figure 46 shows a calculation of copper ionization state based on a simple Thomas Fermi model⁷⁷. This model indicates that the neon ($Z=19$) to oxygen ($Z=21$)-like ionization states of copper can be reached at temperatures ranging from 200 - 400 eV for an electron density range from 1 to 10 times critical. However, this model is steady state and only yields the information that the ionization states which are of interest may be reached by temperatures which are easily accessible in laser produced plasmas.

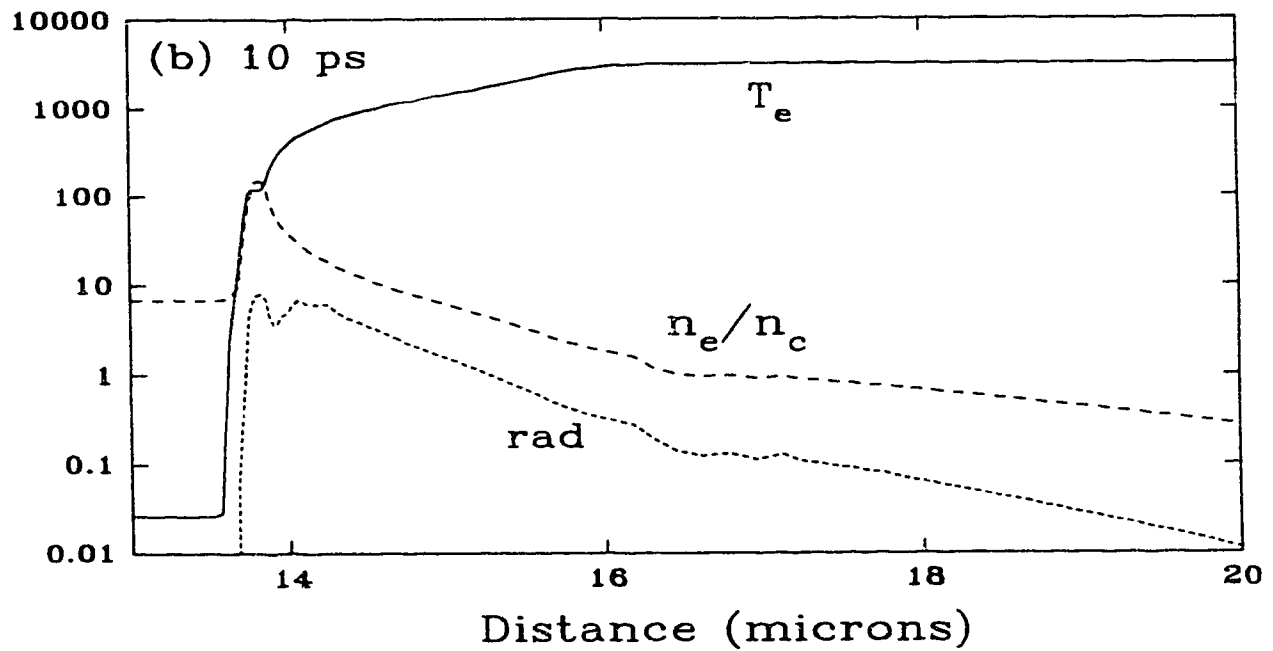
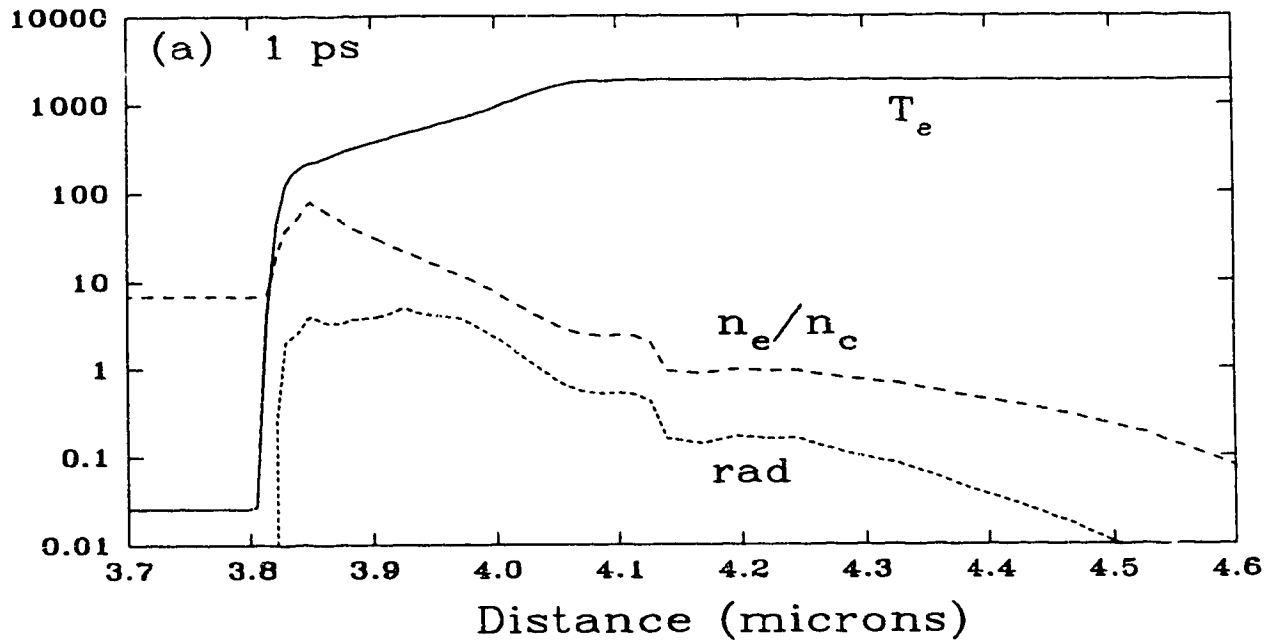


Fig. 45 MEDUSA simulation results at the peak of the laser pulse for (a) 1 ps KrF pulse at 10^{16} Wcm^2 and (b) 10 ps KrF pulse at 10^{16} Wcm^2 . Shows the spatial profiles of electron temperature (T_e in eV), electron density in terms of critical density (n_e / n_c) and the radiation in the plasma (rad) in units of $10^5 \text{ W}\mu\text{m}^{-3}$.

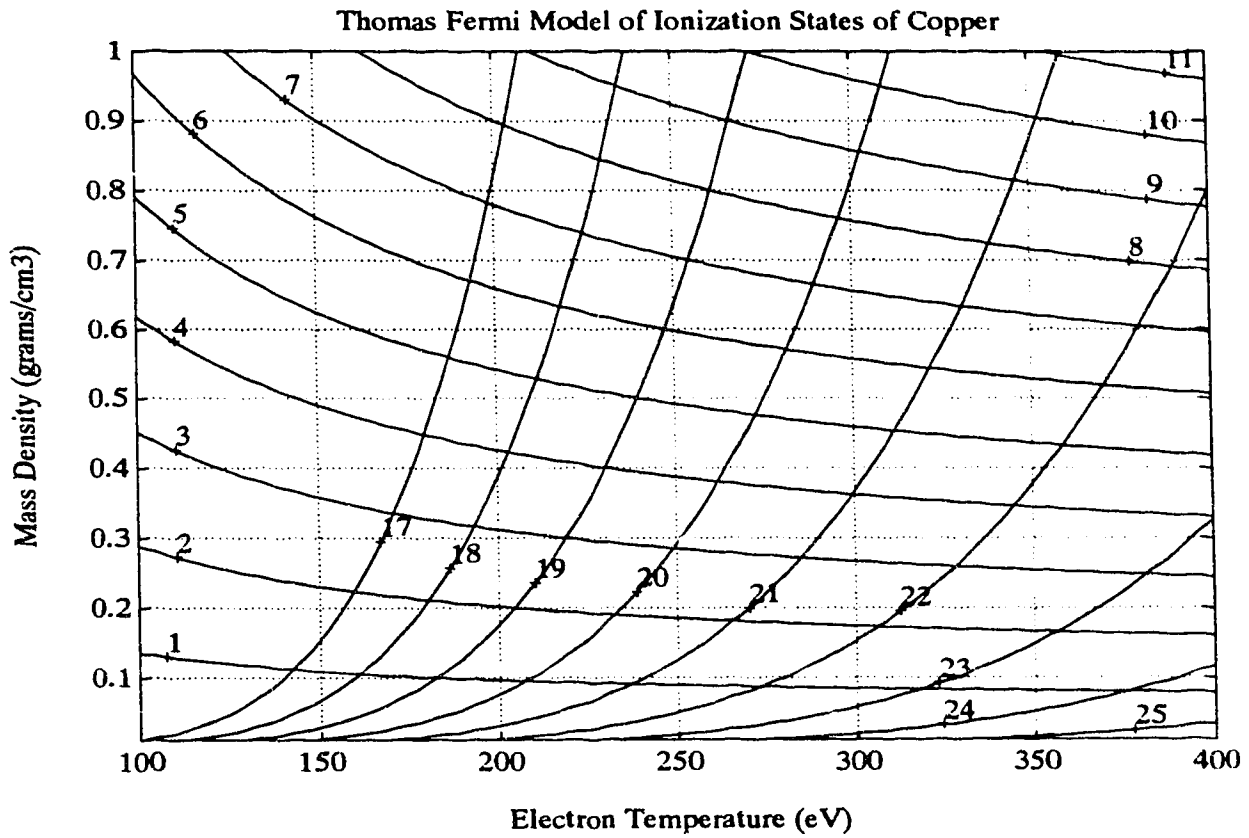


Fig. 46 Ionization of copper according to Thomas Fermi model as a function of mass density (gcm^{-3}) and temperature (eV) showing ionization state contours for Mg-like ($Z=17$) to Be-like ($Z=25$) and electron density contours from 1 to 11 times critical density.

The time required to ionize an atom out of a specified ionization state and into the next can be calculated²⁵ as the inverse of the collisional ionization rate $\langle\sigma_i v\rangle$

$$\langle\sigma_i v\rangle = \bar{g}(1.7 \times 10^{-8}) \left[\frac{R_y}{X_z} \right]^2 \left[\frac{T_e}{R_y} \right]^{1/2} \left[1 - \exp\left(\frac{-5X_z}{T_e} \right) \right] \exp\left(\frac{-X_z}{T_e} \right) \text{ cm}^3 \text{ s}^{-1} \quad (26)$$

Using this estimate Figs. 47a-47c show the timescales for collisional ionization of copper ions from aluminum-like up to the oxygen-like state under the conditions of Figs. 43b and 45b and 45a respectively. The diagram for the 100 ps pulse regime indicates that copper can be ionized to the neon-like state in times of a few picoseconds and that further ionization to fluorine and oxygen-like states will proceed on timescales ranging from 5 - 20 ps. The 10 ps pulse conditions appear to support even more rapid ionization with the bulk of the ionization occurring in subpicosecond timescales and continuing on to oxygen-like in a few picoseconds. The results using the conditions of the 1 ps simulation may provide some of the explanation for the loss of conversion efficiency with the 850 fs pulse. The timescale for achieving the neon-like ionization has increased to several picoseconds which is longer than the actual pulse length. In part this is a result of the intensity of 10^{16} Wcm^{-2} which is used in this case. However, this raises an important point in that the question of whether or not an atom will achieve a specific ionization state depends not only on the ionization rate in a specific region but also on the time spent in that region. This corresponds to the time scale defined by the flow velocity of the plasma. If the atom is swept out into a lower density region before ionization can occur then there will be a significant discrepancy between the steady state ionization predicted from the local temperatures and densities and that which is observed experimentally. It is believed that this is the case for the 850 fs pulses. Note that a proper assessment of the ionization states would require a calculation of time-dependent atomic physics (which is beyond the scope of this thesis) but the present results give a

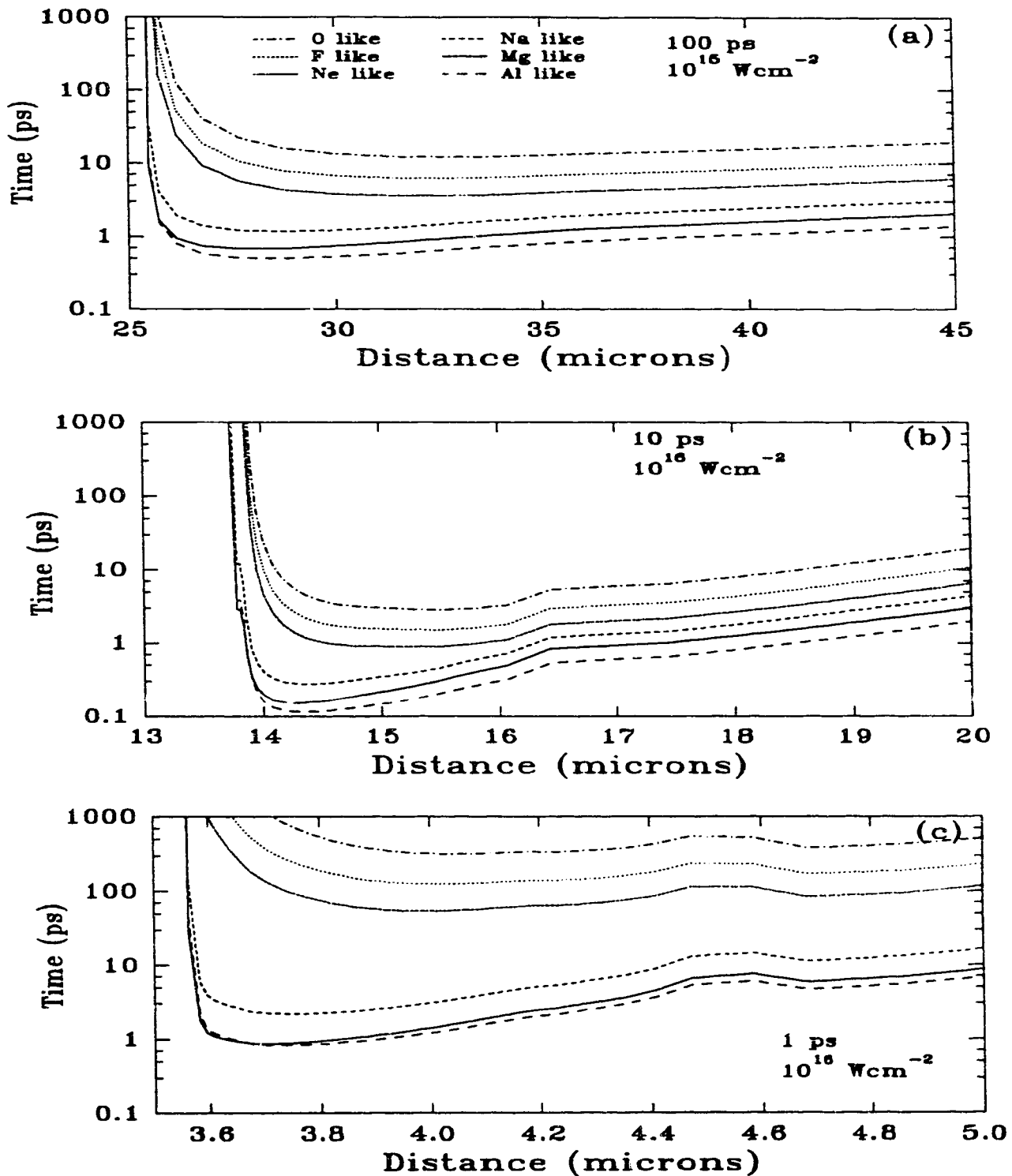


Fig. 47 Ionization timescales for copper ions under conditions shown in Figs. 43b, 45b and 45a. The figure shows the inverse of the collisional ionization rate for ions in the Al through O-like states. Note that the transition to Ne-like ions is generally marked by a significant jump in ionization time.

general indication of the underlying processes which influence the keV conversion efficiency in the various regimes investigated.

The results of the MEDUSA simulations in the 100 ps regime are in basic agreement with those derived using a self-similar analytic model⁷⁵ where the laser radiation is predicted to penetrate to near critical density (2 e-foldings of absorption in an exponential profile) with coronal temperatures ranging from 800 eV for 10^{14} Wcm⁻² to 2500 eV for 10^{15} Wcm⁻². This compares well with the MEDUSA estimates of the peak coronal temperatures of 740 eV and 2200 eV in the two cases respectively. Application of the analytic model to a neon-like copper plasma (Z=19) instead of a helium-like aluminum plasma (Z=11) results in only a marginal reduction in the estimated density and an increase in the coronal temperatures to 900 eV and 3000 eV in the two cases. It must be noted however that the analytic model does not account for radiation cooling which may be small in the case of the aluminum plasma but which will have a significant impact on the copper plasma as a substantial portion of the energy is lost to keV radiation as well as to the other forms of x-ray radiation (recombination). On this basis it may be expected that the copper plasma would likely be somewhat cooler rather than warmer if all processes were accounted for.

The analytic model⁷⁵ can be applied to the shorter pulse regimes under different assumptions where inverse bremsstrahlung is not the dominant absorption mechanism and energy is absorbed at the critical density. In this regime for an aluminum plasma the model predicts coronal temperatures of 1500 eV for the 1 ps pulse at 10^{16} Wcm⁻² and 3500 eV for the 10 ps pulse at the same intensity. These values compare reasonably well with the MEDUSA predicted values of 1800 and 3100 eV respectively. It should be noted that neither of the models accounts for resonance absorption accurately although approximately 30% of the energy reaching the critical density surface in the MEDUSA model is dumped at that point as a rough approximation. In the short pulse regime this energy dump accounts for a significant portion of the heating as generally over 80% of

the laser energy reaches the critical density. The portion of the laser energy which MEDUSA predicts as reaching the critical density surface in the 100 ps case is much lower at 20 - 30 % and as a result a much smaller fraction of the laser energy is dumped at the critical surface. Evidence supporting the existence of resonance absorption was observed in the experiments in the form of the presence of the $K\alpha$ line in the aluminum spectra in Fig. 29. However, it is interesting to note that the height of the $K\alpha$ line is roughly the same in the 2 ps and 90 ps spectra but appears to be reduced in the 850 fs spectra. This is an unexpected result. According to MEDUSA the fraction of the pulse which reaches the critical density increases with decreasing pulse length. This would imply that the shortest pulses should show the strongest evidence of resonance absorption. There are two possible explanations for this apparent discrepancy. One is that there is no discrepancy because the observation of the $K\alpha$ line is not evidence of resonance absorption and that the $K\alpha$ radiation is being generated by some other hot electron mechanism or perhaps it being is photopumped by higher energy x-rays. Another explanation is that the preformed plasma from the ASE is somehow interfering with the "normal" interaction between the short pulse and the critical density plasma and suppressing the resonance absorption process. Because of two-photon absorption losses in the optics, the laser system was operated at maximum gain for the 850 fs shots resulting in a high level of ASE which would lead to a larger preformed plasma than that of the other two pulse length regimes.

Computer simulation of the aluminum spectra that might be expected on the basis of the MEDUSA predictions of plasma conditions were generated using the RATION simulation code⁷⁸. Figures 48a and 48b show RATION generated spectra under the assumptions of no opacity restrictions and steady state ionization. Figure 48a shows the aluminum spectrum predicted by RATION for conditions of approximately 5 times critical density and 500 eV which corresponds to the peak line emission zone from Fig. 43b. In comparison to any of the experimental aluminum spectra in Fig. 29 it may be

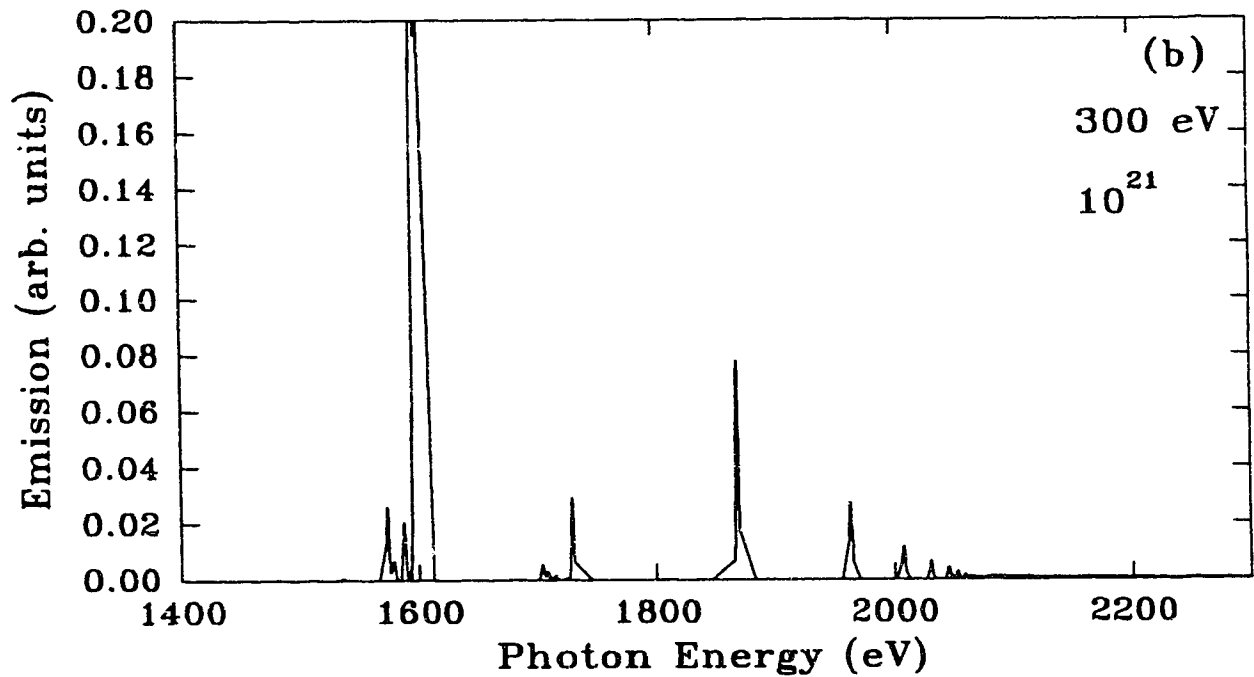
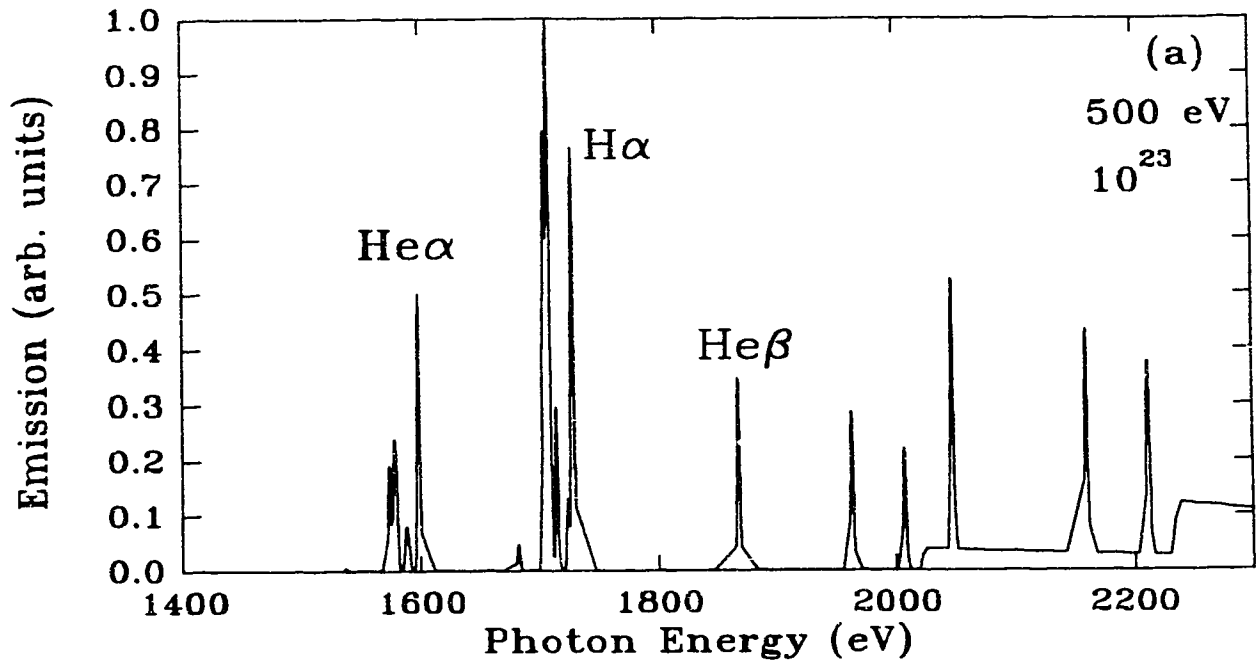


Fig. 48 RATION simulated aluminum spectra at (a) temperature 500 eV and electron density of 10^{23} cm^{-3} (b) temperature 300 eV and 10^{21} cm^{-3} . Spectra include 2.5 eV instrumental broadening to simulate experimental results.

seen that there is a significant discrepancy between the measured results and the theoretical predictions. In spite of the fact that the He α line was permitted to saturate on the film in order to enhance the rest of the spectral structures it is clear that RATION predicts a much higher hydrogenic component (indicated by He β /H α ratio) corresponding to more effective ionization. This discrepancy is most likely the result of 2 factors. Firstly, there is ionization lag in the real plasma where the ionization states do not reach those expected for a given plasma temperature because the heating pulse is too short to allow processes to reach steady state values. Also, the experimental measurement integrates over the late time recombining plasma which leads to a spectrum which can be quite different from that predicted on the basis of the peak temperature conditions. Figure 48b shows the results of reducing the temperature and density parameters until the spectra more closely resemble the experimental results. The assertion that the theoretical spectra from RATION do not resemble the experimental results because of the temporal ionization lag is supported by the findings of Chaker et al.⁷⁹ where the bulk of the emission from an aluminum plasma irradiated by a 1 ps pulse was calculated to occur much later between 4 and 20 ps. Essentially this means that the aluminum spectra from the interaction with the laser are heavily mixed or perhaps even lost in the emission which occurs later when the ions in the cooling plasma recombine. It is difficult to determine how this affects the predictions of MEDUSA and their relation to the experiments which measure x-ray emission in the 800 - 1400 eV range. In order to properly determine the relation between MEDUSA predictions and the experimental results it would be necessary to develop an x-ray postprocessor code to integrate the emission from MEDUSA over the entire duration of the plasma evolution.

Spherical expansion of the plasma may be an additional source of cooling in the 100 ps regime. The transition of plasma flow from a 1D planar regime to a 2D spherical expansion occurs when the scale length of the plasma approaches the diameter of the focal spot. The scale length parameter for planar expanding plasma is given by $L=C_s\tau$

where C_s is the ion sound velocity in the expanding plasma and τ is the pulse length.

The ion sound speed is calculated as:

$$C_s = \sqrt{\frac{ZT_e}{M_i}} \quad (27)$$

where M_i is the mass of the ions in the plasma. Given that the focal spot size is $\sim 10 \mu\text{m}$ with the triplet lens then the estimated scale lengths of the 1 ps and 10 ps cases are $0.23 \mu\text{m}$ and $3.1 \mu\text{m}$ respectively indicating that these pulse lengths produce interactions which may be properly described using planar simulations. In the 100 ps pulse length regime the expansion dimensions of $L=12 \mu\text{m}$ and $23 \mu\text{m}$ at intensities of 10^{14} Wcm^{-2} and 10^{15} Wcm^{-2} respectively indicate that spherical expansion is becoming a contributing factor in the dynamics. The principal effect of the transition to spherical expansion is the cooling of the plasma leading to lower temperatures in the coronal region than predicted by MEDUSA. A second effect may be the introduction of some beam refraction by the expanding plasma reducing the focused intensity.

The plasma generated by the prepulse ASE is more difficult to model because the flow is strongly spherical since the focal spot is approximately $30 \mu\text{m}$ and the plasma evolution occurs over a 5 ns period. Additional difficulty arises from the low intensity, $10^{10} - 10^{11} \text{ Wcm}^{-2}$ which produces an extended cold, low ionization state plasma. The analytic model⁷⁵ discussed above may be extended to spherically expanding plasmas but because of the low intensity some assumption must be made regarding the ionization state of the plasma. Using a Thomas Fermi model⁷⁷ to estimate the ionization state of aluminum at 20 eV yields an ionization state of $Z=6$. Using this value the analytic model produces temperatures ranging from 10 eV to 30 eV and densities of the order of $1/20 - 1/10$ critical in this intensity range with a scale length of $30\mu\text{m}$. These results are qualitatively supported by the MEDUSA model (planar) which predicts temperatures of $\sim 10 \text{ eV}$ for intensities of $10^{10} - 10^{11} \text{ Wcm}^{-2}$. MEDUSA simulations under these

conditions produce plasmas where the density drops very rapidly near the surface (within a few hundred nanometers) of the target to somewhere near 1/10 critical density and then over a much more extended region of tens to hundreds of microns continues to drop to 1/100 critical density and below. In the spherical expansion regime this drop-off would be expected to be even more rapid with a scale length given approximately by the diameter of the focal spot. The temperature and VUV emission characteristics of plasmas generated by low intensity $10^9 - 10^{11} \text{ Wcm}^{-2}$ laser pulses at wavelengths ranging from 308 nm to 1054 nm have been studied by Welleghausen et al.⁸⁰ They have found that the emission spectra in the 30 nm range correspond to plasma temperatures of 5 - 10 eV which further supports the results obtained from the modelling.

The presence of the preformed plasma has a number of effects on the generation of x-rays from the main pulse. Firstly, it presents an extended cloud of cold, low ionization state material which the main pulse must burn through in order to reach the target surface. In this sense the preformed plasma constitutes a loss mechanism because heating this plasma does not produce keV x-rays. This loss is expected to be relatively small on the basis of estimates of the ablated mass from the target for the main pulses versus the prepulse. The ablated mass can be estimated using the analytic model and for the main laser pulse gives values ranging from 1.5 pg for the 1 ps pulse at 10^{16} Wcm^{-2} to near 200 pg for the 100 ps pulse at 10^{15} Wcm^{-2} . Estimates of the ablated mass from the 5 ns prepulse range from 50 -150 pg in a range of $10^{10} -10^{11} \text{ Wcm}^{-2}$. However, this mass is expanding into 2π steradians and only ~0.5% of what is ablated remains within the solid angle of the laser beam. As a result the mass of the preformed plasma would only be considered significant in comparison to the mass ablated by the main pulse in the 1 ps case and will become less significant as intensity increases. In all cases the preformed plasma would absorb only a small fraction of the energy of the main pulse because of the extremely low density of the bulk of the plasma. However, in the region close to the target surface the density of the preformed plasma rises rapidly from 1/10

critical through critical to the solid density of the target. In this area the existence of the plasma is highly advantageous because inverse bremsstrahlung will be very strong and the short density scale length allows the laser pulse to begin coupling almost immediately to high density plasma.

There may be some disadvantage associated with the fact that the focal spot for the ASE is roughly three times larger than the main pulse focal spot. The situation that arises is one where the main pulse is heating a small spot in the middle of a much larger cold plasma spot on the target surface. The effect that this surrounding cold plasma will have is not clearly understood. It is possible that it may represent a heat sink for the energy from the main pulse. The opposing case is that it is possible that the heat transport into the surrounding plasma becomes severely flux limited as soon as the central spot reaches a sufficiently high temperature. A second factor which is likely to suppress the transfer of heat to the surrounding plasma is the generation of toroidal magnetic fields around the focal spot. Such fields would suppress the motion of electrons out of the focal zone and thus restrict heat transport out of the focal spot. The surrounding plasma can probably be expected to absorb a certain amount of heat early in the interaction process even if flux limiting factors cut off the flow later. It should be noted that the pinhole camera measurements of the x-ray emission zone were reasonably close to the values predicted by the ray tracing code. This would seem to indicate that lateral energy transport does not spread the energy of the laser over the entire ASE spot zone and that it is not an overriding factor in removing energy from the main laser-plasma spot.

The intensity dependence scaling has been observed to change strongly between pulse length regimes. In the 100 ps pulse length range the experiments with the 120 ps pulse and the 20 cm lens produced intensities of $1.5 \times 10^{14} \text{ Wcm}^{-2}$ and mid Z_N conversion efficiencies of 1-3%. The reduction of the focal spot size using the 12.5 cm triplet lens in combination with the 90 ps pulse produced intensities of $8 \times 10^{14} \text{ Wcm}^{-2}$

and increased yields to 10-13% corresponding to more effective heating of the plasma. The measured threshold intensity in this regime is $6 \times 10^{13} \text{ Wcm}^{-2}$ to get 1% conversion from copper with peak conversion efficiency at $\sim 10^{15} \text{ Wcm}^{-2}$. In the shorter pulse regimes the necessary intensities shift to much higher values in that the peak intensity to measure 1% conversion efficiency with the 2 ps pulse is estimated to be $4 \times 10^{15} \text{ Wcm}^{-2}$ with the maximum measured value occurring at $3 \times 10^{16} \text{ Wcm}^{-2}$. Using the 850 fs pulse the requisite intensities again shift to higher values with the measurement of 4% conversion efficiency at $6 \times 10^{16} \text{ Wcm}^{-2}$. Experiments done using a planoconvex 20 cm CaF_2 lens and the 850 fs pulse saw detector yields reduced to less than 10% of those seen using the quartz triplet in spite of the fact that pulse energies on target were as high as 45 mJ (corresponding to peak intensities of $1.5 \times 10^{16} \text{ Wcm}^{-2}$). The scaling of the threshold intensity with pulse length is not surprising since higher intensities are required with the shorter pulses in order to achieve the required plasma temperatures of 500-1000 eV.

A fairly clear scaling of the x-ray conversion efficiency with pulse length has been observed for a constant pulse energy. In the 100 ps regime absorption by the plasma is almost complete indicating a regime which is close to optimum in terms of generating x-rays without wasting energy to reflection losses. The combination of the 90 ps pulse and the triplet lens yielded mid Z_N conversion efficiencies of 10-13% demonstrating the ability to generate substantial x-rays using these pulse lengths. The simulations at 100 ps pulse lengths using MEDUSA indicate a shift in the keV emission zone to higher densities with increasing intensity improving the radiation efficiency. Experiments with the "stretched" 2 ps pulse and the 12.5 cm triplet lens gave intensities of $3 \times 10^{16} \text{ Wcm}^{-2}$ but with reduced conversion efficiencies of 8 - 10%. The measured plasma specular reflectivity of 20-25% appears to account for most of the loss in conversion efficiency. Using the 850 fs pulse the conversion efficiency from copper was seen to drop to 4% in spite of the increase in intensity to $\sim 6 \times 10^{16} \text{ Wcm}^{-2}$ using the triplet lens. The observed specular reflectivity of 30% does not account for all of the

reduction in conversion efficiency. In this case it appears likely that ionization lag has become a significant factor in suppressing the generation of keV x-rays.

In the pulse length regimes which surround those that have been investigated it is expected that reduced x-ray conversion efficiency will be observed given the same pulse energies. In the range above 100 ps the intensity will be reduced and the keV emission zone will shift to lower densities. The resulting lower temperature, lower density plasma will result in smaller x-ray conversion efficiencies. In the pulse length regimes below 850 fs the reflectivity of the plasma would be expected to increase slightly to around 50%. The resultant short scale length plasma would allow coupling of the laser energy to close to solid density producing a very dense but cold plasma leading to reduced keV emission. In addition the ionization lag would become more significant and result in the generation of even less keV radiation. Another undesirable consequence of the use of pulses in the 1 ps and shorter regime is the reduction in the amount of target material which is heated. Due to the very short interaction times the heating takes place in a very thin region and may fail to generate significant quantities of heated plasma. Finally, the problems of two-photon absorption and self-focusing in the laser system when working with subpicosecond pulses makes operation with ultrashort pulses undesirable. On the basis of the experimental results the optimal pulse length regime for keV x-ray generation using KrF pulses from commercial sized modules where pulse energies are on the order of 50 mJ appears to be in the region of 10 - 100 ps where the lower limit is determined by plasma reflectivity losses and the upper limit is determined by the need to generate adequate intensity for heating.

The development of x-ray generation systems using KrF lasers must be considered in the context of development of systems based on glass lasers. Glass lasers have been under development for a longer period of time than excimer lasers and the technology of producing glass lasers is more mature. Glass lasers have an important advantage in their ability to access higher pulse energy regimes due to longer energy

storage times. However, the repetition rate is severely limited by the need to remove heat deposited from the flashlamps that pump the glass medium. This limitation may be overcome with the development of diode laser pumped glass systems but at present such systems are expensive. Glass lasers also have an additional disadvantage because of their long wavelength (1.06 μm) which limits the conversion efficiency³³ unless the pulse is frequency multiplied to green or UV light (usually an inefficient process itself). In spite of these limitations an x-ray generation system based on a glass system with a repetition rate of 1 Hz, a pulse length of 10 ns and pulse energy of 20 J has been developed by Hampshire Instruments and AT&T Laboratories⁸¹. An instructive comparison may be made between what might be expected with this system and what might be expected from a KrF based system. Assuming 5% conversion efficiency from the glass laser gives a sustained flux of 1.59 mWcm^{-2} at a distance of 10 cm. In the case of a 20 W KrF (400 mJ pulse trains at 50 Hz) module assuming 10% conversion one gets 3.18 mWcm^{-2} at 10 cm. With the low energy pulses at a high repetition rate KrF has an additional advantage in that the energy deposition in the x-ray mask per pulse is lower and this reduces stress due to rapid heating from the x-ray pulse. One further advantage of KrF is the ability to work in atmospheric helium background gas. Fully ionized helium at atmospheric pressure has an electron density of approximately $5 \times 10^{19} \text{ cm}^{-3}$ which is $\sim 5\%$ of critical density for $1 \mu\text{m}$ light whereas it is only $\sim 0.3\%$ of critical density for KrF. This could be expected to have a very strong deleterious effect on the ability of glass laser radiation to heat a solid target in atmospheric helium.

The choice of target material for use in a laser based keV x-ray generation system is influenced by a number of factors. Mask contrast is important because with softer x-rays (i.e. from iron) it is possible to use thinner layers of masking material to achieve a given contrast level. At present the technology of producing masks is considered one of the biggest challenges to the development of x-ray lithography. The drawback to softer x-rays is the penetration depth in resist material. If the x-rays are unable to penetrate the

resist material effectively the dose must be increased (leading to longer exposure times and reducing chip yields) or multilayer resists must be used (increasing complexity and cost). Using harder x-rays from materials like copper or zinc can increase the penetration depth of the x-rays into the resist and produce better definition in the resulting profiles because of the uniformity of exposure through the depth of the resist. However, harder x-rays require thicker masks to get proper contrast and can also produce scattered electrons in the resist which can reduce profile definition. In this sense x-ray generation from laser plasmas has an important advantage in the ability to allow tuning of the emission by choice of target material. An additional possibility for tuning of x-ray energy comes from the use of M shell emitters where the line structure seen with the L shell is broadened into band structure. Using an x-ray monochromator and targets such as tin, iodine or xenon it would be possible to obtain tunable narrow line x-ray sources similar to tunable sources presently available from synchrotron machines.

CONCLUSIONS

In the later part of this decade or most certainly by the beginning of the 21'st century the technology behind manufacturing the most advanced computer chips will change from lithography based on the use of visible photons to the use of x-ray photons as the exposure source. For many companies and research groups the benefits of developing x-ray lithography will only be available if a source of x-rays is developed which is a cost effective alternative to the enormous capital investments associated with building a synchrotron facility. Laser plasma generated x-rays may very well represent such an alternative. This project represents the first phase of research into the question of whether or not a sustained flux keV x-ray source can be based on plasmas generated by KrF lasers. It is known that KrF lasers are capable of producing continuous power outputs of several hundred watts and if some substantial fraction of that energy can be converted to useful x-rays on a continuous basis then a viable alternative to synchrotrons will exist. The research which has been carried out for this thesis has been aimed at determining if a KrF laser pulse such as might be generated by a system based on commercial excimer modules (as opposed to much larger research oriented units) can access the high efficiency (>10%) regime which has been demonstrated with much larger laser systems. In order to carry out this investigation a KrF laser system has been developed with the specific aim of measuring x-ray conversion efficiencies with picosecond UV laser pulses. X-ray conversion efficiencies into 2π steradians in the 800 -1400 eV photon energy range have been measured for a variety of target materials.

The KrF laser system constructed by the author specifically for these experiments incorporates two dye laser systems pumped by a XeCl laser to produce visible ($\lambda=497$ nm) pulses in the 100 ps and 1 ps pulse length regimes. These pulses are frequency doubled and amplified in a KrF laser module to produce on target energies of 50 - 55 mJ in the 100 ps regime and 35 - 40 mJ in the 1 ps regime. Early experiments using a pulse

length of 120 ps and a 20 cm planoconvex quartz lens produced peak intensities estimated at $1.5 \times 10^{14} \text{ Wcm}^{-2}$. X-ray conversion efficiencies under these conditions were measured to be in the range of 1-3% for mid Z_N materials such as iron, nickel and copper. These results were substantially improved by the use of a 12.5 cm aberration corrected triplet lens and a reduction of pulse length to 90 ps resulting in peak intensities of $8 \times 10^{14} \text{ Wcm}^{-2}$. With the higher intensities x-ray conversion efficiencies rose into the 10 - 13% range due to increased plasma temperature. Conversion efficiencies were also measured using 2 ps KrF pulses where the peak intensities were estimated to be $3 \times 10^{16} \text{ Wcm}^{-2}$ and were found to be in the 8-10% range for the mid Z_N materials with plasma reflectivity (~20-25%) accounting for much of the loss in efficiency. Evidence from aluminum spectra indicated that the 2 ps pulses were generating higher temperature plasmas in spite of the reduced coupling efficiency between the laser and the plasma. Conversion efficiency measurements using an 850 fs pulse with peak intensity of approximately $6 \times 10^{16} \text{ Wcm}^{-2}$ on a copper target yielded a reduced value of 4%. In this case plasma reflectivity(~30%) is not able to account for the reduction in x-ray yield. The most likely explanation is that short time scale ionization dynamics are responsible for the reduced yield. In the 850 fs regime the copper atoms may be unable to ionize quickly enough to produce keV radiation in the quantities observed with the longer pulses. In addition some consideration must be given to degradation of the beam due to self-focusing in the lens.

The broad tunability of the laser-plasma based x-ray source has been demonstrated by varying the target material. Mid Z_N materials such as iron and cobalt up to zinc have been shown to be good L shell keV emitters and it has been seen that the centroid of emission can be tuned from 950 eV up to 1250 eV using these materials. These materials produce spectra containing a strong component from neon-like ions due to the jump in ionization energies at the neon-like stage. It has also been observed that the nature of the emission spectrum can be changed from the line spectra of the L shell

emitters to the smoother band structure of M shell emitters by using materials such as tin. It is expected that the tunability seen in the L shell materials will also be seen with the M shell materials. However, the spectra will be much less dominated by any one ionization species because of the relatively smooth transition in ionization energies associated with the larger shell structure.

The optimal pulse length to be used in a specific system is essentially determined by two considerations. Firstly, given that KrF amplifiers provide a limited amount of energy to any one pulse the pulse length must be reduced in order to increase the intensity to that required for efficient keV emission. The intensity requirement observed is on the order of $8 \times 10^{14} \text{ Wcm}^{-2}$ for 100 ps pulses with higher intensities increasing the risk of nonlinear processes which may modify the energy coupling between the laser and the plasma. Reducing the pulse length increases the loss of energy due to reflection and eventually introduces technical difficulties from two-photon absorption and beam degradation due to self-focusing in the optics. Thus there is a lower limit on the usable pulse length. The actual value of the lower limit would probably be on the order of 10 ps. The conclusion is that the optimal pulse length for a 50 mJ KrF laser pulse is in the 10 to 100 ps range.

There are a number of questions which remain for future research which could effectively be investigated using the system developed for this project. In terms of the laser system itself the addition of an electro-optic switch to the quenched resonator pump beam in order to control the rise time could, in principle, allow access to an almost continuous range of pulse lengths from 10 ps to 200 ps which would provide a wealth of information on the detailed behaviour of the pulse length scaling. It would also allow for the possibility of shaped pulse and multiple pulse experiments where the issues of multiple pulse x-ray generation could be addressed. It would also be valuable to expand the selection of target materials by investigating more of the M shell materials such as iodine and xenon. Another important issue for future research is the development of

more detailed modelling for the radiation processes including a preformed plasma and tests to determine how closely the simulation codes correspond to the reality of the experimental results. Important technical questions also remain to be studied before commercial x-ray systems can be developed. The crucial question is whether or not the energy available in a KrF amplifier can be efficiently extracted in a pulse train and the high conversion efficiency maintained throughout the process.

Conversion efficiencies in the 10-13% range demonstrated here are competitive with the best results achieved by other groups³³ with much larger laser systems. This study has clearly demonstrated that small KrF laser systems are capable of accessing this high conversion efficiency regime using single short laser pulses.

REFERENCES

- ¹ T. Mochizuki, T. Yabe, K. Okada, M. Hamada, N. Ikeda, S. Kiyokawa and C. Yamanaka
Atomic number dependence of soft x-ray emission from various targets irradiated by a 0.53 μm wavelength laser
Phys. Rev. A 33(1), 525 (1986)
- ² A.A. Hauer, N.D. Delamater and Z.M. Koenig
High resolution x-ray spectroscopic diagnostics of laser heated and ICF plasmas
Laser and Particle Beams 9(1), 3 (1991)
- ³ H. Pepin, R. Fabbro, B. Faral, F. Amiranoff, J. Virmont, F. Cottet and J.P. Romain
The x-ray emission, ablation pressure and preheating for foils irradiated at 0.26 μm wavelength
Phys. Fluids 28(11), 3393 (1985)
- ⁴ P.D. Gupta, R. Popil, R. Fedosejevs, A.A. Offenberger, D. Salzmann and C.E. Capjack
Temperature and x-ray intensity scaling in KrF laser plasma interaction
Appl. Phys. Lett. 48(2), 103 (1986)
- ⁵ N. Nakano and H. Kuroda
Energies and time resolved spectroscopy of 10 - 2000 \AA emissions from laser plasmas produced by a picosecond laser
Phys. Rev. A 35(11), 4719 (1987)
- ⁶ R.C. Elton
X-ray lasers
Academic press (1990)
- ⁷ D.L. Matthews, P.L. Hagelstein, M.D. Rosen, M.J. Eckart, N.M. Ceglio et al.
Demonstration of a soft x-ray amplifier
Phys. Rev. A 54(2), 110 (1985)
- ⁸ T.N. Lee, E.A. McLean and R.C. Elton
Soft x-ray lasing in neonlike germanium and copper plasmas
Phys. Rev. Lett. 59(11), 1185 (1987)
- ⁹ G.D. Enright and H. Baldis
XUV gain measurements in a collisionally excited germanium plasma
20'th Anomalous Absorption Conference 1990
- ¹⁰ N.H. Burnett and G.D. Enright
Population inversion in the recombination of optically ionized plasmas

- IEEE J. Quant. Elect. 26(10), 1797 (1990)
- ¹¹ M.Howells, J. Kirz, D. Sayre and G. Schmahl
Soft x-ray microscopes
Physics Today, August 1985 22
- ¹² C. Jacobsen, S. Williams, E. Anderson, M.T. Browne, C.J. Buckley et al.
Diffraction limited imaging in a scanning transmission x-ray microscope
Opt. Comm. 86, 351 (1991)
- ¹³ J.E. Trebes, S. Mrowka, T.W. Barbee, J. Brase, J.A. Koch, R.A. London et al.
Demonstration of x-ray microscopy with an x-ray laser operating near the carbon K edge
Opt. Lett. 17(10), 754 (1992)
- ¹⁴ F. Bijkerk, G.E. van Dorssen, M.J. van der Wiel, R. Dammel and J. Lingnau
Laser plasma as x-ray source for lithographic imaging of submicron structures onto experimental x-ray resist
Microelect. Eng. 9, 121 (1989)
- ¹⁵ W. Arden
Optical versus x-ray lithography for future device fabrication
Microelect. Eng. 13, 231 (1991)
- ¹⁶ S. Okazaki
Resolution limits of optical lithography
J. Vac. Sci. Technol. B 9(6), 2829 (1991)
- ¹⁷ D.M. Tennant, J.E. Bjorkholm, R.M D'Souza et al.
Reflective mask technologies and imaging results in soft x-ray projection lithography
J. Vac. Sci. Technol. B 9(6), 3176 (1991)
- ¹⁸ D.L. White, J.E. Bjorkholm, J. Bokor et al.
Soft x-ray projection lithography
Solid State Tech. July 1991 37
- ¹⁹ J.N. Broughton and R. Fedosejevs
X-ray generation from 50 mJ, 120 ps KrF laser produced plasmas
J. Appl. Phys. 71(3), 1153 (1992)
- ²⁰ J.N. Broughton and R. Fedosejevs
Efficient keV x-ray generation from 50 mJ KrF laser plasmas
Appl. Phys. Lett. 60(15), 1818 (1992)
- ²¹ T.W. Johnston and J.M. Dawson

- Phys. Fluids 16,722 (1973)
- ²² W.L. Kruer
The Physics of Laser Plasma Interactions
Addison Wesley 1988
- ²³ R.M. More
Atomic physics in inertial confinement fusion
UCRL Preprint 84991 Lawrence Livermore Laboratory (1981)
- ²⁴ R.P. McWhirter
Plasma Diagnostic Techniques
Academic Press (1965)
- ²⁵ I.H. Hutchinson
Principles of Plasma Diagnostics
Cambridge University Press (1987)
- ²⁶ H. Pepin, B. Grek, F. Rheault and D.J. Nagel
X-ray emission measurements from CO₂ laser created plasmas
J. Appl. Phys. 48(8), 3312 (1977)
- ²⁷ R.D. Bleach and D.J. Nagel
Plasma x-ray emission produced by ruby lasers at 10^{12} W/cm²
J. Appl. Phys. 49(7), 2832 (1978)
- ²⁸ K.M. Glibert, J.P. Anthes, M.A. Gusinow, M.A. Palmer, R.R. Whitlock, D.J. Nagel
X-ray yields of plasmas heated by 8 nsec neodymium laser pulses
J. Appl. Phys. 51(3), 1449 (1980)
- ²⁹ P. Alaterre, H. Pepin, R. Fabbro and B. Faral
X-ray conversion efficiency as a function of atomic number for 0.26 μm laser irradiated targets
Phys. Rev. A 34(5), 4184 (1986)
- ³⁰ R. Popil, P.D. Gupta, R. Fedosejevs and A.A. Offenberger
Measurement of KrF laser plasma x-ray radiation from targets with various atomic numbers
Phys. Rev. A 35(9), 3874 (1987)
- ³¹ R. Kodama, K. Okada, N. Ikeda, M. Mineo, K.A. Tanaka, T. Mochizuki and C. Yamanaka
Soft x-ray emission from ω_0 , $2\omega_0$, $4\omega_0$ laser produced plasmas
J. Appl. Phys. 59(9), 3050 (1986)

- ³² R. Fedosejevs, R. Popil, P.D. Gupta, D. Vick, Y.Y. Tsui and A.A. Offenberger
Characterization of x-ray production from krypton fluoride laser produced plasma
Proc. SPIE volume 831 p66 (1987)
- ³³ M. Chaker, H. Pepin, V. Bateau, B. Lafontaine, I. Toubhans, R. Fabbro and B. Faral
Laser plasma x-ray sources for microlithography
J. Appl. Phys. 63(3), 892 (1988)
- ³⁴ F. O'Neill, G.M. Davis, M.C. Gower, I.C.E. Turcu, M. Lawless and M. Williams
Plasma x-ray sources for lithography generated by a 0.5 J KrF laser
SPIE vol 831 p230 (1987)
- ³⁵ D. Xenakis, M.H.R. Hutchinson, F.O'Neill and I.C.E. Turcu
Laser plasma x-ray generation using an injection mode locked XeCl excimer laser
J. Appl. Phys. 71(1), 85 (1992)
- ³⁶ S. Szatmari and F.P. Schafer
Simple generation of high power, picosecond, tunable excimer laser pulses
Opt. Comm. 48, 279 (1983)
- ³⁷ S. Szatmari and F.P. Schafer
Excimer laser pumped ps dye laser
Appl. Phys. B 33, 95 (1984)
- ³⁸ S. Szatmari and F.P. Schafer
Subpicosecond, widely tunable distributed feedback dye laser
Appl. Phys. B 46, 305 (1988)
- ³⁹ S. Szatmari and F.P. Schafer
Simplified laser system for the generation of 60 fs pulses at 248 nm
Opt. Comm. 68(3), 196 (1988)
- ⁴⁰ S. Szatmari
Pulse shortening of 5×10^3 by the combined pulse forming of dye oscillators, saturated amplifiers and gated saturable absorbers
Opt. and Quant. Elect. 21, 55 (1989)
- ⁴¹ D.C Thompson, R. Fedosejevs, A.A. Offenberger, J.P. Santiago and H.R. Manjunath
Measurements of gain and absorption saturation in an electron beam pumped KrF amplifier
IEEE J. Quant. Elect. 25(10), 2161 (1989)
- ⁴² R.R. Freeman and P.H. Bucksbaum
Investigations of above-threshold ionization using subpicosecond laser pulses

- J. Phys. B. At. Mol. Opt. Phys. 24, 325 (1991)
- ⁴³ M.L. Sentis, P. Delaporte, B.M. Forestier and B.L. Fontaine
Design and characteristics of high pulse repetition rate and high average power
excimer laser systems
IEEE J. Quant. Elect. 27(10), 2332 (1991)
- ⁴⁴ M. J. Kushner
Microarcs as a termination mechanism of optical pulses in electric discharge excited
KrF excimer lasers
IEEE Trans. on Plasma Sci. 19(2), 387 (1991)
- ⁴⁵ T.Y. Chang
Improved uniform field electrode profiles for TEA laser and high voltage applications
Rev. Sci. Instr. 44(4), 405 (1973)
- ⁴⁶ C. Li Thomas
POTENT: a package for computation of electric and magnetic fields
- ⁴⁷ R.C. Sze
Rare gas halide avalanche discharge lasers
IEEE J. Quant. Elect. 15(12), 1338 (1979)
- ⁴⁸ A. Garscadden, M.J. Kushner and J.G. Eden
Plasma physics issues in gas discharge laser development
IEEE Trans. on Plasma Sci. 19(6), 1013 (1991)
- ⁴⁹ F. Kannari
Multilevel model analysis of energy extraction from a KrF laser medium by short
pulses
J. Appl. Phys. 67(9), 3954 (1990)
- ⁵⁰ M. Mizoguchi, K. Kondo and S. Watanabe
100-fs, 10 Hz terawatt KrF laser
J. Opt. Soc. Am. B 9(4), 560 (1992)
- ⁵¹ S. Szatmari and F.P. Schafer
Comparative study of the gain dynamics of XeCl and KrF with subpicosecond
resolution
J. Opt. Soc. Am. B 4(12), 1943 (1987)
- ⁵² A.J. Taylor, R.B. Gibson and J.P. Roberts
Picosecond gain dynamics in KrF amplifiers
Appl. Phys. Lett. 52(10), 773 (1988)

- ⁵³ P. Simon, P. Klebniczki and G. Szabo
A study of picosecond pulse generation by a double resonator dye laser
Optics. Comm. 56(5), 359 (1986)
- ⁵⁴ Z. Bor and A. Muller
Picosecond distributed feedback dye lasers
IEEE J. Quant. Elect. 22(8), 1524 (1986)
- ⁵⁵ A. Brun, P. Georges, G. Le Saux and F. Salin
Single shot characterization of ultrashort pulses
J. Phys. D: Appl. Phys. 24, 1225 (1991)
- ⁵⁶ M. Kaschke and B. Wilhelmi
Pump pulse induced chirp production in semiconductors
Appl. Phys. B 45,71 (1988)
- ⁵⁷ W.T. White, W.L. Smith and D. Milam
Opt. Lett. 9,10 (1984)
- ⁵⁸ S.P. Le Blanc, G. Szabo and R. Sauerbrey
Femtosecond single shot phase sensitive autocorrelator for the ultraviolet
Optics. Lett. 16(19), 1508 (1991)
- ⁵⁹ R. Fedosejevs Private Communication
- ⁶⁰ M. Krumrey, E. Tegeler, J. Barth, M. Krisch, F. Schafers, and R. Wolf
Schottky type photodiodes as detectors in the VUV and soft x-ray range
Appl. Opt. 27, 4336 (1988)
- ⁶¹ B10 filter material courtesy Alexander Vacuum Research, Greenfield, MA 01301
- ⁶² B.L. Henke, J.Y. Uejio, G.F. Stone, C.H. Dittmore and F.G. Fujiwara
High energy x-ray response of photographic films: models and measurement
J. Opt. Soc. Am. B 3(11), 1540 (1986)
- ⁶³ B.L. Henke, P. Lee, T.J. Tanaka, R.L. Shimabukuro and B.K. Fujikawa
Low energy x-ray interaction coefficients: photoabsorption, scattering and reflection
Atomic Data and Nuclear Data Tables 27,1 (1982)
- ⁶⁴ R. Hall
A quantitative description of Bragg analysers
PhD. Thesis University of Leicester 1980
- ⁶⁵ M. Chaker, V. Bateau, J.C. Kieffer, H. Pepin and T.W. Johnston
Calibrated soft x-ray spectroscopy using transmission grating, pinhole and film

Rev. Sci. Instrum. 60(11), 3386 (1989)

- ⁶⁶ H. Gordon, M.G. Hobby and N.J. Peacock
Classification of the x-ray spectra of transitions in Ne, F and O isoelectronic sequences of the elements from iron to bromine and in the Na isoelectronic sequence of gallium to bromine
J. Phys. B: Atom. Molec. Phys. 13,1985 (1980)
- ⁶⁷ M. Chaker, S. Boily, B. Lafontaine, J.C. Kieffer, H. Pepin, I. Toubhans and R. Fabbro
X-ray wavelength optimization of the laser plasma x-ray lithography source
Microelect. Eng. 10, 91 (1990)
- ⁶⁸ Heidenhain GMBH. Traunreut, Germany
- ⁶⁹ B.L. Henke, S.L. Kwok, J.Y. Uejio, H.T. Yamada and G.C. Young
Low energy x-ray response of photographic films. I . Mathematical models
J. Opt. Soc. Am. B 1, 818 (1984)
- ⁷⁰ N.M. Ceglio, R.L. Kaufmann, A.M. Hawryluk and H. Medeki
Time resolved x-ray transmission grating spectrometer for studying laser produced plasmas
Appl. Opt. 22,318 (1983)
- ⁷¹ R. Kodama, T. Mochizuki, K.A. Tanaka and C. Yamanaka
Enhancement of keV x-ray emission in laser produced plasmas by a weak prepulse laser
Appl. Phys. Lett. 50(12), 720 (1987)
- ⁷² K.A. Tanaka, A. Yamauchi, R. Kodama, T. Mochizuki, T. Yamanaka, S. Nakai and C. Yamanaka
Enhancement of soft x-ray emission using prepulses with 2ω and 4ω laser plasmas
J. Appl. Phys. 63(5), 1787 (1988)
- ⁷³ R.Fedosejevs, R. Ottman, R. Sigel, G. Kuhnle, S. Szatmari and F.P. Schafer
Absorption of subpicosecond ultraviolet laser pulses in high density plasma
Appl. Phys. B 50, 79 (1990)
- ⁷⁴ J.P. Christiansen, D.E.T.F. Ashby and K.V. Roberts
MEDUSA
Comp. Phys. Comm. 7,271 (1974)
- ⁷⁵ P. Mora
Theoretical model of absorption of laser light by a plasma
Phys. Fluids 25(6), 1051 (1982)

- ⁷⁶ R. Marchand, A. Birnboim, C.E. Capjack and D. Salzmann
A fast radiation transport algorithm for planar laser produced plasmas
- ⁷⁷ R. More
Atomic physics in inertial confinement fusion
Preprint UCRL-84991 Lawrence Livermore Laboratory (1981)
- ⁷⁸ R.W. Lee
Lawrence Livermore Laboratory
Private Communication
- ⁷⁹ M. Chaker, J.C. Kieffer, J.P. Matte and H. Pepin
Interaction of a 1 psec laser pulse with solid matter
Phys. Fluids B 3(1), 167 (1991)
- ⁸⁰ B. Welleghausen, M. Hube and F. Jin
Investigations on laser plasma soft x-ray sources generated with low energy laser systems
Appl. Phys. B 49, 173 (1989)
- ⁸¹ J. Frackoviak, G.K. Celler, R.R. Freeman, C.W. Jurgensen et al.
Evaluation of a laser based proximity x-ray stepper
paper 1671-10 SPIE Proceeding 1671 March 1992

APPENDIX 1

Laser System Alignment Techniques

This section presents some of the technical details of alignment and setup of the different stages for the benefit of those who may want to develop similar systems and for those who must maintain the systems developed during the course of this project.

The alignment of the QR is generally straightforward but is best optimized by experience and diagnosis using a streak camera. Begin with the outer resonator strongly misaligned to ensure no spurious signals confuse the first stage of the setup. Start with a relatively soft focus of the pump beam on the dye cell. It should be just enough to get lasing from the cell walls. Locate the laser spot on a target several meters away and mark the position of the inner resonator output. Align the outer resonator such that it lases in exactly the same direction. In a stepwise manner, march the outer resonator output beam down (or up) by first tilting the back mirror and then realigning the front mirror, continue until there is about 5 degrees of separation. It is highly likely that the output from the inner resonator will disappear during this process. This is remedied by increasing the focusing of the pump beam. The angular separation between the resonators and the intensity of the pump beam can be varied until the output pulse is deemed to have suitable spatial and temporal qualities. If necessary the concentration of the laser dye may also be varied in order to allow modified pumping geometry. It may also be necessary to change the length of the outer resonator since this determines when the inner resonator is quenched. If the outer resonator is too short there may be some pulse shortening but only at substantial expense in output energy. If the outer resonator is too long it will fail to quench the second pulse from the inner resonator. In the beginning stages it may be helpful to observe the unquenched output from the inner resonator on a streak camera and its dependence on pump intensity. In principle it is

possible to optimize the output pulse without the use of the outer resonator because the only available parameter is pump pulse focusing. However, it is usually necessary to make tradeoffs in focusing to get full quenching from the outer resonator.

The alignment of the SCDL is very simple. The most important point is to check the parallelism of the mirrors when the SCDL is assembled (using a Helium Neon laser). Start with the lens which focuses the pump beam from the QR several cm closer to the SCDL than it's focal length (such that there is no output) and tighten the focusing until lasing begins. Further improvements must be diagnosed with a streak camera. The pulshape of the output can vary from a single pulse with no tail to a series of pulses with a strong tail structure depending on the strength of the pump pulse and the alignment of the mirrors. Be careful not to focus too hard into the SCDL, it is unlikely that any damage will occur with such small energies but it is possible for the QR pulse to overpump the SCDL and burn it's way through instead of being absorbed. This can result in some confusion as to what constitutes the correct pulse for the next stage. The lens which follows the SCDL is used to collimate the strongly divergent pulse for amplification prior to use in the subsequent stage. The need for care in setting up the SCDL cannot be overemphasized because spatial structure in the SCDL pulse affects the formation of the grating image in the DFDL. In fact, the quality of this pulse is of such importance that Szatmari rotates and spatially filters the amplified SCDL pulse to reject all but the main lobe of the diffraction pattern generated by passage through the amplifier. In practice, I do not use this procedure as I was able to obtain a sufficiently uniform beam without any additional modifications. It is necessary to check the amplified SCDL pulse for visual uniformity by strongly expanding it over several meters using a short focal length lens. Possible sources of structure in the beam can go all the way back to the XeCl laser.

The basic alignment of the DFDL is straightforward in principle but ends up depending strongly on the quality of the amplified SCDL pulse. The cylindrical

telescope which precedes the objective serves two purposes. First is to enlarge the pump beam horizontally such that 3 - 5 mm of grating is illuminated (this determines the aspect ratio of the grating image). Second is to refocus the beams at the front focal point of the objective. The grating is placed into the pump beam at the image position of the objective and the zero order blocker installed at the entrance to the objective. At this point the dye cell can be installed using glycerin to make optical contact between the objective and the cell. If there is any doubt as to the initial positioning of the grating the emergence angle between the two interfering beams can be checked using a thick quartz window (20 mm) with a fluorescent target. Contact the window to the objective using glycerin (just as the cell will be contacted) and verify that the angle between the two beams is close to the theoretical value (estimated at 94°). When the dye cell is installed the distance between the inner surface of the dye cell and the objective should be adjusted to the working distance specified for the objective as a starting point. The first signs to look for when attempting to get laser operation from the DF DL are visually observable evidence of the transition from fluorescence to lasing (observed on white paper 1 - 2 cm from cell). This transition is characterized by two things. First is a change in spatial structure of the output. Fluorescence is characterized by relatively diffuse output whereas lasing is indicated the appearance of a smaller spot in which laser speckle may be seen to appear. The second change is in the color of the output, there should be a modification of the color of the output spot as the grating structure is formed or lost. This is dependent on the position of the grating but is always correlated with the transition from the large fluorescence spot to the tighter laser beam. Beyond these visual indications the true test of DF DL operation is the ability to tune the wavelength of the output by moving the grating. Beyond these procedures there is no systematic process other than controlled parameter variation to obtain optimized output. Setup of this system is not a trivial process, the initial development of this system required three months of continuous work.